Deconstruction of tropospheric chemical reactivity using aircraft measurements: the ATom data

Michael J. Prather[1], Hao Guo[1,2], and Xin Zhu[1]

[1]Department of Earth System Science, University of California at Irvine, Irvine, CA 92697-3100, USA
[2]State Key Laboratory of Organic Geochemistry, Guangzhou Institute of Geochemistry, Chinese Academy of Sciences, Tianhe, Guangzhou 510640, China

Correspondence to: Michael J. Prather (mprather@uci.edu)

Abstract. The NASA Atmospheric Tomography (ATom) Mission completed four seasonal deployments (August 2016, February 2017, October 2017, May 2018), each with regular 0.2-12 km profiling through transecting the remote Pacific and Atlantic Ocean basins. Additional data are acquired also for the Southern Ocean and Arctic basin, as well as two flights over Antarctica. ATom in situ measurements provide a near-complete chemical characterization of the ~140,000 10-second (80 m by 2 km) air parcels measured along the flight path. This paper presents the Modeling Data Stream (MDS), a continuous gap-filled record of the 10-s parcels containing the chemical species needed to initialize a gas-phase chemistry model for the budgets of tropospheric ozone and methane. Global 3D models have been used to calculate the Reactivity Data Stream (RDS), which is comprised of the chemical reactivities (production and loss) for methane, ozone, and carbon monoxide, through 24-hour integration of the 10-s parcels. These parcels accurately sample tropospheric heterogeneity and allow us to partially deconstruct the spatial scales and variability that defines tropospheric chemistry from composition to reactions. This paper provides a first look and analysis of the up-to-date MDS and RDS data including all four deployments (Prather et al., 2023, doi: 10.7280/D1B12H).

ATom's regular profiling of the ocean basins allows for weighted averages to build probability densities for key species and reactivities presented here. These statistics provide climatological metrics for global chemistry models, for example, the large-scale pattern of ozone and methane loss in the lower troposphere, and the more sporadic hot spots of ozone production in the upper troposphere. The profiling curtains of reactivity also identify meteorologically variable and hence deployment-specific hot spots of photochemical activity. Added calculations of the sensitivities of the production and loss terms relative to each species emphasize the few dominant species that control the ozone and methane budgets, and whose statistical patterns should be key model-measurement metrics. From the sensitivities, we also derive linearized lifetimes of ozone and methane on a parcel-by-parcel basis and average over the basins, providing an observational basis for these previously model-only diagnostics. We had found that most model differences in the ozone and methane budgets are caused by the models calculating different climatologies for the key species such as O_3, CO, H_2O, NOx, CH_4 plus T, and thus these ATom measurements provide a substantial contribution to the understanding of model differences and even identifying model errors in global tropospheric chemistry.

Table of Contents

1 Introduction

The environmental damage caused by chemically reactive greenhouse gases and most air pollutants is controlled by a balance between their sources and sinks, with atmospheric photochemistry as the major sink. The net chemical loss is comprised of a highly heterogeneous mixture of air parcels, each with its own mix of species, and each with its own chemical production and/or loss rates that are designated here as reactivities: P-O3, L-O3, L-CH4, and L-CO (see Prather et al., 2017; 2018, hence P2017 and P2018). A reactivity is calculated as the 24-hour integration of a reaction rate, or the sum of several reaction rates, that describe budgets of species in units of ppb (10^{-9} mole fraction) per day. In this paper we continue our efforts to deconstruct global tropospheric chemistry, examining its finest scales, reconstructing and parsing the O_3 and CH_4 budgets over the remote ocean basins as sampled by the NASA Atmospheric Tomography (ATom) Mission.

ATom provided intensive, chemically comprehensive measurement of air parcels (typically 10 s averages, equivalent to 2 km along flight by 80 m in the vertical) and extensive four-season semi-global 0-12 km profiling through the remote troposphere (Wofsy et al., 2021; Thompson et al., 2021). Recent publications have identified new scientific opportunities coming from the ATom observation, with topics including scales of variability (Schill et al., 2020; Allen et al., 2022), global CO forecasting (Strode et al., 2018), and OH oxidative capacity (Wolfe et al., 2019; Brune et al., 2020; Travis et al., 2020; Anderson et al., 2021), as well as aerosol distribution, formation, and precursors (Brock et al., 2021; Williamson et al., 2021; Veres et al., 2020). Guo et al. (2023: hence G2023) calculated the reactivities for all 10 s air parcels from the first deployment ATom-1 (29 July – 23 August 2016) and compared their statistics with six global chemistry model's sample day in mid-August. Note that the first published version (Guo et al., 2021) has been withdrawn due to some errors in the reactivities and is corrected with G2023.

Here we report reactivities for all four seasonal deployments (ATom-1234, see Fig. 1) and examine how their statistical patterns change with season. We extend the analysis of Pacific and Atlantic basins (Fig. 2) to the Southern Ocean and Polar regions, with a first look at Antarctic tropospheric chemistry. We present sensitivity analyses to identify which of the ATom-measured species drives the reactivities and are thus critical for the chemistry-climate models (CCMs) to simulate accurately. We show how the sensitivity analyses on each parcel can be used to estimate the true lifetime of tropospheric O_3 and the CH_4 chemical feedback. Overall, we hope to use the 10 s parcel statistics (>140,000 parcels in ATom) to build performance metrics for CCMs.

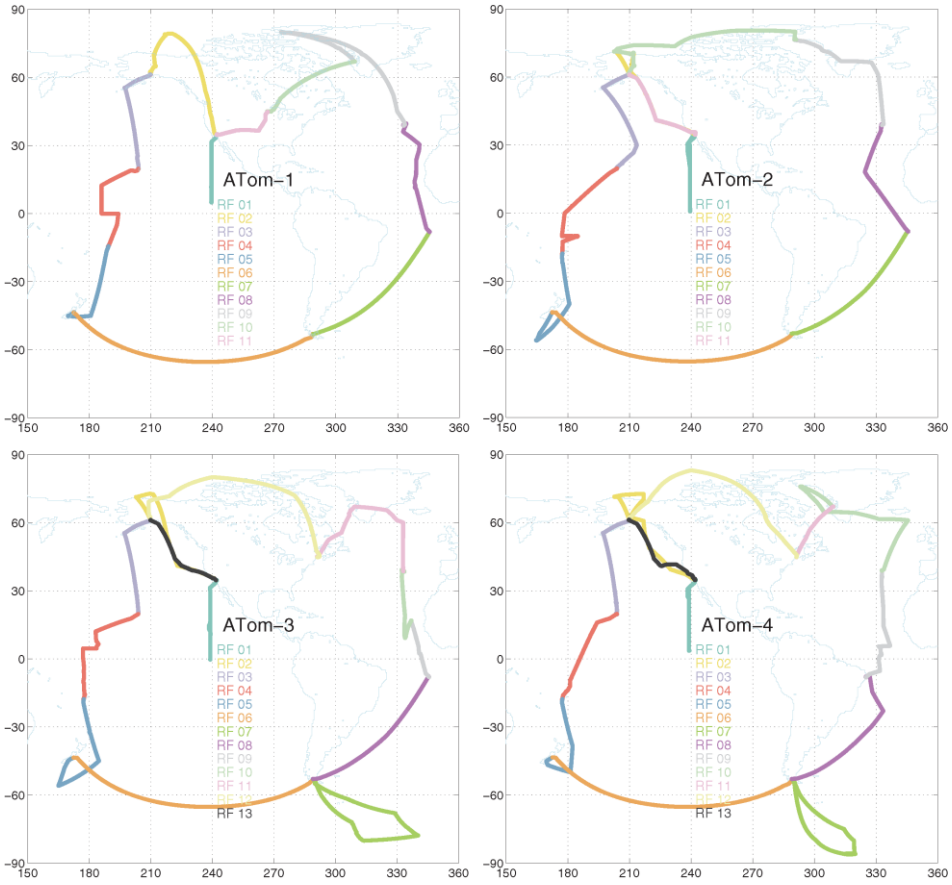

Figure 1. Map of ATom1234 flights, noting Research Flight number for each deployment. The flight sequence is counter clockwise starting at Palmdale CA. The first research flight of each deployment is the transect from CA nearly to the Equator along 121°W. The dates of each deployment are: ATom-1, 29 Jul – 23 Aug 2016; ATom-2, 26 Jan – 21 Feb 2017; ATom-3, 28 Sep – 27 Oct 2017; ATom-4, 24 Apr – 21 May 2018.

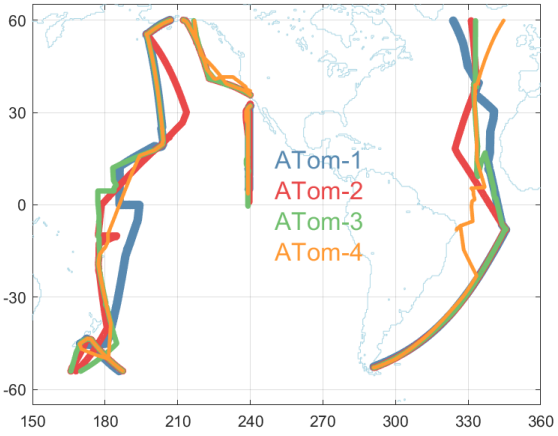

Figure 2. Map of the portion of ATom1234 flights included in the Pacific and Atlantic basin analysis. Flight tracks are plotted in successively thinner lines to see the overlap. These flights comprise 91,912 parcels out of the total of 146,494.

2 Methods, measurements, and outline

2.1 Reactivities

Our interests in the reactivity of air parcels or model grid cells began with P2017, continuing with P2018 and G2023. We focused on the budgets of O_3 and CH_4, and now add CO. Reactivities are defined by a few key reaction rates:

Loss of CH_4 (L-CH4),

$$CH_4 + OH \rightarrow CH_3 + H_2O \quad \text{(R1)}$$

Production of O_3 (P-O3),

$$HO_2 + NO \rightarrow NO_2 + RO \quad \text{(R2a)}$$

$$RO_2 + NO \rightarrow NO_2 + RO \quad \text{(R2b)}$$

$$O_2 + h\nu \rightarrow O + O \ \text{(x 2)} \quad \text{(R2c)}$$

Loss of O_3 (L-O3),

$$O_3 + OH \rightarrow O_2 + HO_2 \quad \text{(R3a)}$$

$$O_3 + HO_2 \rightarrow HO + O_2 + O_2 \quad \text{(R3b)}$$

$$O(^1D) + H_2O \rightarrow OH + OH \quad \text{(R3c)}$$

Loss of CO (L-CO).

$$CO + OH \rightarrow CO_2 + H \quad \text{(R4)}$$

In addition, we include statistics on two key photolysis rates that drive the chemistry:

Photolysis of O_3 yielding $O(^1D)$ (j-O1D).

$$O_3 + h\nu \rightarrow O(^1D) + O_2 \quad \text{(R5)}$$

Photolysis of NO_2 (j-NO2).

$$NO_2 + h\nu \rightarrow NO + O \quad \text{(R6)}$$

These rates are readily diagnosed in most CCMs. We found that the net P-O3 minus L-O3 describes the 24 h O_3 tendencies over the ocean basins, but not exactly as expected, and particularly not in highly polluted regions (G2023). Reaction 2c is important in tropospheric budget of O_3 only above ATom flight levels (12 km, Prather, 2009). In terms of the overall CO budget, we lack the chemical production of CO from CH_4 and other volatile organic compounds.

We focus on the Pacific and Atlantic oceanic flights of ATom, which we constrain to be 53°S to 60°N (see the map of included flights in Fig. 2), because these two ocean basins dominate the loss of CH_4 and O_3 and are a large part of the production of O_3 in most CCMs (P2017). The tropics clearly dominate the chemical budgets and we single out the three ATom-measured regions: Central Pacific (30ºS-30ºN, about the Dateline), Eastern Pacific (0º-30ºN, ~121ºW, the first flight of each deployment, to/from Palmdale), Tropical Atlantic (30ºS-30ºN). The Southern Ocean (66ºS-55ºS, the Christchurch to

Punta Arenas flight) and two polar regions (Arctic, >66ºN; Antarctic, <66ºS) are also examined separately. Only over-ocean data is analyzed here except for the two polar regions.

2.2 Protocols

The ATom observations used for the reactivity calculations here are taken from the Modeling Data Stream MDS-2b, described in G2023 and available at Prather et al. (2023). When completing this analysis, it was found that the method of gap-filling for NOx did not take advantage of all the observations (i.e., flight segments where NO was measured but NO_2 was not). Thus, the updated NOx gap-filling MDS-3 was developed.

The Reactivity Data Stream (RDS) reports the reactivities listed above plus the net 24-hour change in O_3 for each 145,388 parcels, land or ocean. (Research flight number 11 of ATom-4 was a ferry flight from Greenland to Maine without profiling for which many instruments were shut down, and thus the 1,106 parcels have NaN values for MDS and RDS.) Reactivity calculations here use the UCIZ model and the RDS* protocol described in G2023. UCIZ is the updated UCI chemistry-transport model (CTM version q7.4) by Xin Zhu that is adapted to calculating ATom air parcels. RDS* protocol allows the PAN and HNO_4 species to thermally decay for 24 hours before use. The overall ATom protocol for CTM/CCMs averages five days separated by five days centered on each deployments' central month (ATom-1, August; ATom-2, February; ATom-3, October; ATom-4, May) to average over the cloud fields (see P2017; P2018).

The ATom RDS protocol for CTM/CCMs is to locate the nearest model grid cell and then place the ATom air parcel in that cell (along with all the other parcels in their own cells) and then integrate for 24 hours (usually starting at 0000 UTC). The problem is that many 10 s parcels may lie in the same grid cell. We use the following nested search algorithm to locate an unoccupied cell nearby: (1^{st}) search E-W from -8 to +8 longitude-shifted cells; (2^{nd}) search up-down in pressure by -2 to +2 levels; (3^{rd}) search N-S by -2 to +2 latitude-shifted cells. With our 1.1-degree CTM, we are always able to find an empty cell, however, the latitude, longitude, and pressure of the grid cell may differ from the ATom-measured value. Figure 3 shows the ATom value (MDS, x-axis) versus the CTM grid-cell value (RDS, y-axis) for the 32,383 parcels of ATom-1. The mean errors in placement are very small, and even the root-mean square error is modest (±1.7° latitude, ±5.7° longitude, ±15.3 hPa).

The CTM/CCM is run 24 hours without advection, convection or other mixing, without wet scavenging or dry deposition or emissions. These requirements are critical because otherwise the air parcel's evolution would depend on the composition of neighboring cells, which are unknown from the ATom measurements. The key model-dependent quantities that control the reactivities are the photolysis rates, which depend on clouds and overhead column ozone. Figure 4 compares the j-values and reactivities for the ATom-1 parcels calculated for day numbers 213 (1 Aug) and 223 (11 Aug). The j-values have the largest scatter, and that drives a reduced level of scatter in reactivities. The j-NO2 value is not much affected by overhead ozone column and so we conclude the scatter in j-values and reactivities is driven primarily by the time varying cloud fields. (The UCI CTM uses 3-hour averaged cloud fields.) The O_3 tendency (dO3/dt) has less scatter than any of the four reactivities (P-O3, L-O3, L-CH4, L-CO) because the production and loss co-vary with clouds and their net difference has less scatter.

We expect the abundance of the reactive species to evolve over the 24-hour period of the reactivity calculation, and this is documented in Fig. 5. Species with no sources, because emissions are shut off, decrease over the 24 hour (CO, C_2H_6, alkane, alkene). NOx systematically decreases because there are no direct emissions and HNO_3 is a major sink. HOOH systematically increases because wet scavenging is turned off. O_3 and PAN show plus-minus scatter. HNO_3 increases at values less than 2 ppb, but decreases at the highest values (~ 3 ppb). In terms of the calculation of ATom reactivities, the

scatter is not worrisome, but the systematic shifts in HOOH and NOx are a concern. The P2017 experiments showed that averaged over an ocean basin, the reactivities with all processes running for 24 hours versus the ATom protocol were similar. A protocol that slowly removed HOOH and added NOx is tempting but would require some arbitrary parameterizations.

2.3 Outline

Latitude-by-altitude curtain plots of the reactivities along flight tracks are presented in Section 3, along with reactivity statistics of the means and extremes, altitude mean profiles, and probability densities. In Section 4, we analyze the sensitivities of the reactivities to each of the observed species for ATom-1. These sensitivities identify those critical species where a model bias will introduce large errors in the O_3 and CH_4 budgets. In Section 5, we examine the impacts of MDS-3 on these analyses, and we introduce probability densities for some critical species as a possible model metric. In Section 6 we show how the ATom parcel reactivities and sensitivities can be used to derive chemical feedbacks, such as the lifetime for O_3 perturbations and the CH_4 lifetime feedback factor. Section 7 concludes this analysis.

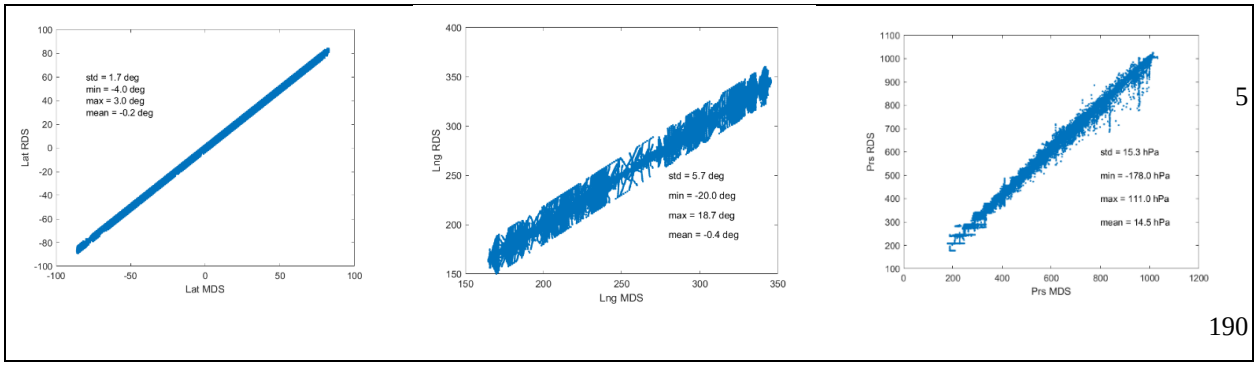

Figure 3. Comparison of the model grid cell value for pressure, latitude, and longitude used in the RDS calculation with those from the 32,383 10 s ATom-1 parcels (MDS). In each figure the standard deviation, minimum error, maximum error and mean error are shown. Values are specific to the UCI CTM with a T159L57 grid. These displacement errors occur because several 10 s parcels often occur within one CTM cell and must be shifted to nearby vacant cells.

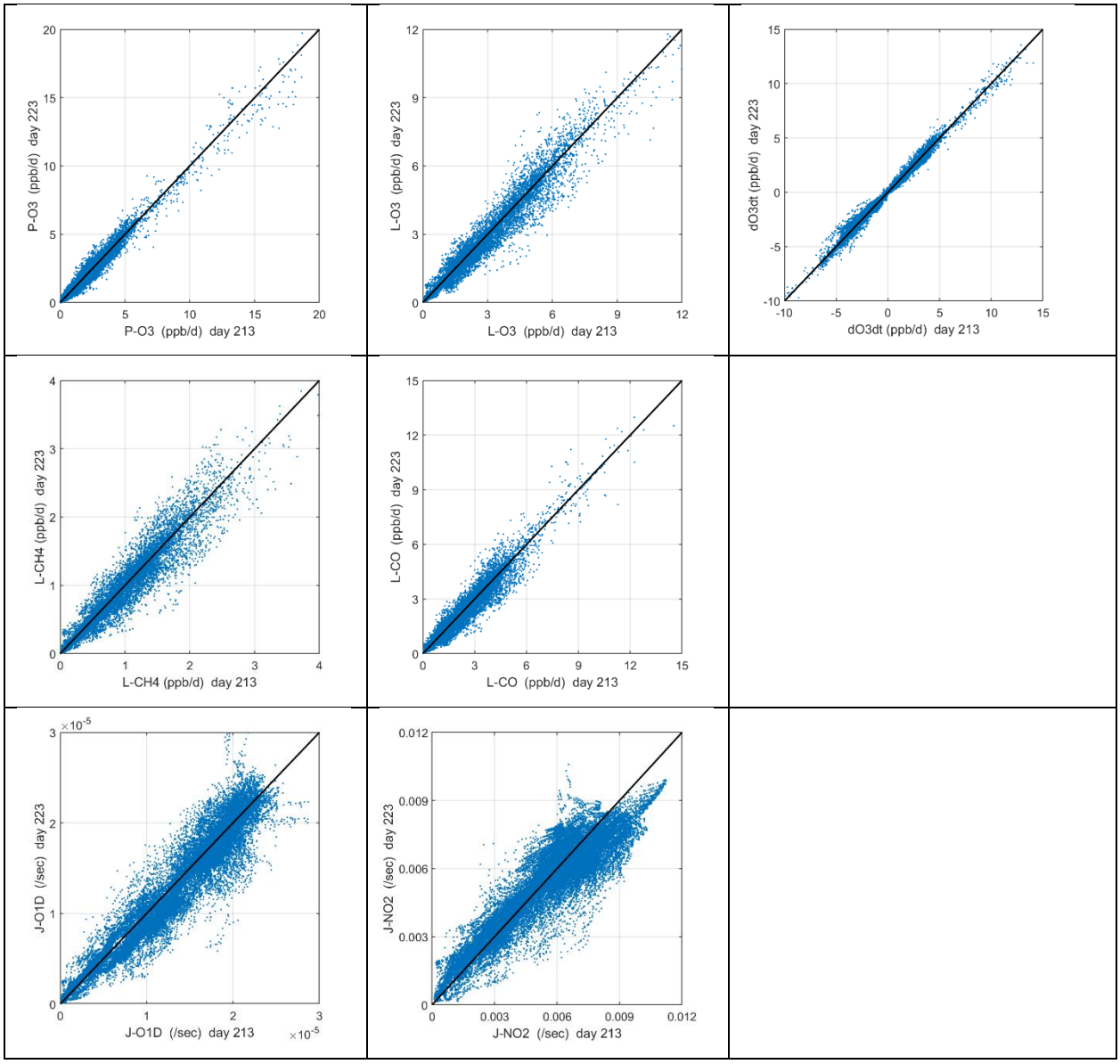

Figure 4. Reactivities (ppb/b) and J-values (/sec) calculated for all 32,383 ATom-1 10 s parcels using two different days with different cloud fields and ozone columns. The net integrated ozone change over the day, dO3/dt (ppb/d), is also shown. Day 213 = August 1 and day 223 = August 11. Mean reactivity statistics here are calculated as the mean of five days (August 1, 6, 11, 16, 21), while sensitivity analyses used only day 223.

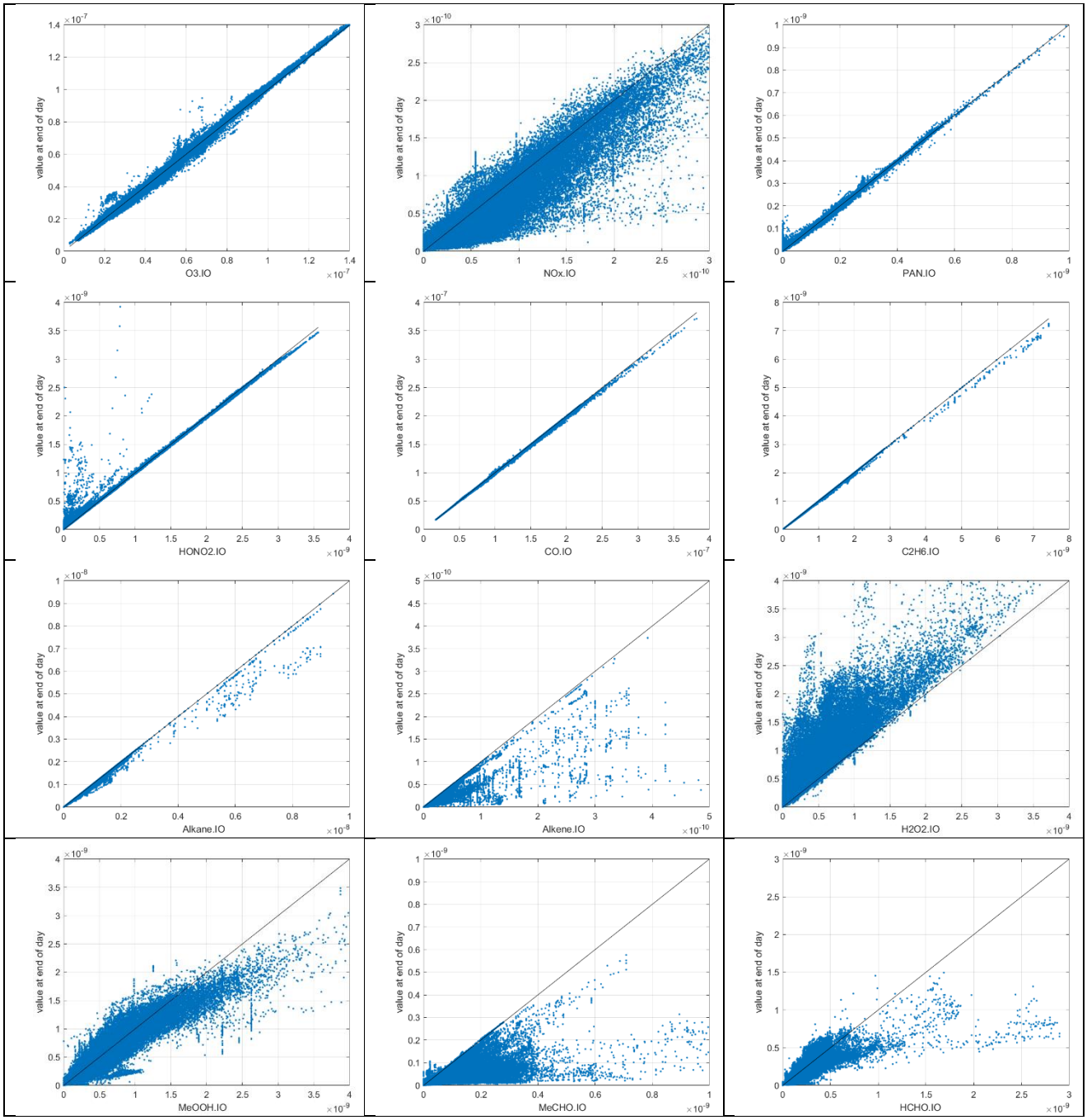

Figure 5. The input/output values of reactive species showing the 24-hour change from the ATom-1 MDS input value (x-axis) to the final value (y-axis) calculated following the ATom protocol in the UCI CTM. First row: O_3, NOx, PAN. Second row: $HONO_2$, CO, C_2H_6. Third row: Alkane (C_{3+}), Alkene (C_2H_4), H_2O_2. Fourth row: CH_3OOH (MeOOH), CH_3CHO (MeCHO), HCHO.

3 Variation of photochemical reactivities across the four ATom deployments

3.1 Reactivity statistics – means and extremes

We developed statistics that identify extremes (i.e., photochemical hot spots) and characterize the heterogeneous mix of air parcels. Table 1 presents the means and medians of each of the four reactivities (P-O3, L-O3, L-CH4, L-CO) and two j-values (j-O1D, j-NO2) for each of the eight regions (Pacific, Atlantic, Central Tropical Pacific, Eastern Tropical Pacific, Tropical Atlantic, Southern Ocean, Arctic, Antarctic) and four deployments (ATom-1234: in August, February, October, May respectively). Each 10 s parcel is weighted to give equal sampling by mass from 0-12 km for each 10º latitude bin or a single latitude bin for polar latitudes. The extreme statistics look at the top 50%, 10%, and 3% of the weighted parcels, giving the mean reactivity in those ranges as well as the fraction of total weighted reactivity in those upper ranges.

Starting with the Pacific and Atlantic basins, we see that the average photolysis rates (j-O1D, j-NO2, Table 1ef) have little seasonality (variation across deployments), and further, have a flat distribution with median greater than mean. For P-O3 (Table 1a) the Atlantic mean is slightly larger (10-20 %) than the Pacific except for ATom-2. The medians are always smaller than the mean. The reactivity of the top 10% is about 2.5 times that of the mean, indicating a distribution peaked to photochemical hot spots. For L-O3 (Table 1b) the Atlantic mean is much larger (30-50 %) than the Pacific, and the extreme statistics are similar. What is unusual is that ATom-1 has the lowest mean P-O3 in both Pacific and Atlantic, while it has a high or the highest L-O3. Thus, ATom-1 has a distinctly different mix of species than ATom-234. A clear seasonality is seen for L-O3 with ATom-2 (February) having the lowest reactivities, presumably due to the reduced activity of northern mid-latitude continental pollution in winter. L-CO (Table 1d) shows similar patterns as L-O3 (lowest in ATom-2 Pacific, highest in ATom-1 Atlantic), while that of L-CH4 (Table 1c) is more uniform across deployments. This feature can be seen in the curtain and mean profile plots where L-CH4 is restricted to the lower troposphere due to the high temperature sensitivity of rate coefficient for reaction (1).

The Arctic region is highly seasonal, and photochemistry mostly shuts down in ATom-2 and -3 (Feb and Oct) but it is quite reactive in ATom-1 and -4 (Aug and May). This is seen clearly in the j-values (Table 1ef), particularly j-O1D, which is the primary source of OH. The Arctic reactivities in ATom-1 and -4 are about 2/3 of the mean Pacific and Atlantic values year round, with the exception of L-CH4 which is extremely repressed due to the colder Arctic temperatures in all seasons. The extreme statistics in the Arctic are similar to the Pacific and Atlantic except for P-O3 in ATom-234 which is dominated by hot parcels. Note that we have excluded the stratospheric parcels in these statistics (see Supplement of G2023).

The Southern Ocean has high reactivities for ATom-2 and -3 as expected for austral summer. L-O3 and L-CO are about half the reactivity of the Arctic for the complementary seasons, but P-O3 and L-CH4 are more similar to the Arctic. Clearly, the chemical mixture of these two regions is different. The extreme statistics for the S. Ocean are similar to the Arctic.

The Antarctic flights of ATom were a target of opportunity for ATom-3 and -4. ATom-4 (May) was too dark to have significant reactivity (extremely low j-values, Table 1ef). ATom-3 Antarctica has distinctly lower reactivities than ATom-3 S. Ocean except for P-O3 which is surprisingly comparable.

Table 1. Statistics on Reactivities and J-values by basin and deployment

P-O3	react-ivity	deploy-ment	avg R (ppb/d)	mdn R (ppb/d)	avg R (ppb/d) in top50	avg R (ppb/d) in top10	avg R (ppb/d) in top03	fraction of total R in top50	fraction of total R in top10	fraction of total R in top03
Pacific	P-O3	ATom1	1.11	0.94	1.76	3.03	4.25	80%	27%	12%
Pacific	P-O3	ATom2	1.42	1.38	2.10	3.09	3.75	74%	22%	8%
Pacific	P-O3	ATom3	1.57	1.40	2.38	4.10	6.17	76%	26%	12%
Pacific	P-O3	ATom4	1.37	1.31	2.08	3.07	3.73	76%	22%	8%
Atlantic	P-O3	ATom1	1.25	1.10	2.07	3.38	4.21	83%	27%	10%
Atlantic	P-O3	ATom2	1.44	1.30	2.16	3.21	3.74	75%	22%	8%
Atlantic	P-O3	ATom3	1.84	1.70	2.65	3.94	4.73	72%	22%	8%
Atlantic	P-O3	ATom4	1.60	1.43	2.42	3.99	5.53	76%	25%	10%
C.Pacific	P-O3	ATom1	1.23	1.14	1.78	2.74	3.52	73%	22%	9%
C.Pacific	P-O3	ATom2	1.69	1.67	2.24	2.99	3.56	66%	18%	7%
C.Pacific	P-O3	ATom3	2.02	1.80	2.88	4.89	7.72	71%	24%	12%
C.Pacific	P-O3	ATom4	1.72	1.66	2.32	3.17	3.63	68%	19%	6%
E.Pacific	P-O3	ATom1	1.88	1.71	2.61	4.17	5.57	70%	22%	9%
E.Pacific	P-O3	ATom2	1.98	1.89	2.54	3.36	3.71	64%	17%	6%
E.Pacific	P-O3	ATom3	1.89	1.80	2.26	3.00	3.57	60%	16%	6%
E.Pacific	P-O3	ATom4	2.11	2.14	2.68	3.55	4.28	64%	17%	6%
T.Atlantic	P-O3	ATom1	1.47	1.35	2.24	3.57	4.33	76%	24%	9%
T.Atlantic	P-O3	ATom2	1.72	1.60	2.37	3.30	3.80	69%	19%	7%
T.Atlantic	P-O3	ATom3	2.28	2.18	3.00	4.13	4.80	66%	18%	6%
T.Atlantic	P-O3	ATom4	1.96	1.73	2.75	4.53	6.02	70%	23%	10%
Arctic	P-O3	ATom1	0.76	0.52	1.26	2.58	3.44	83%	34%	14%
Arctic	P-O3	ATom2	0.03	0.02	0.06	0.11	0.14	93%	37%	14%
Arctic	P-O3	ATom3	0.15	0.07	0.27	0.62	0.86	91%	41%	17%
Arctic	P-O3	ATom4	1.01	0.89	1.40	2.05	2.27	70%	21%	7%
S.Ocean	P-O3	ATom1	0.12	0.11	0.18	0.28	0.34	72%	22%	8%
S.Ocean	P-O3	ATom2	0.98	0.90	1.39	2.00	2.50	71%	21%	8%
S.Ocean	P-O3	ATom3	0.54	0.48	0.79	1.18	1.42	73%	22%	8%
S.Ocean	P-O3	ATom4	0.11	0.08	0.18	0.34	0.44	81%	32%	12%
Antarctic	P-O3	ATom3	0.53	0.49	0.71	0.98	1.12	68%	19%	7%
Antarctic	P-O3	ATom4	0.00	0.00	0.01	0.02	0.04	99%	72%	38%

L-O3	react-ivity	deploy-ment	avg R (ppb/d)	mdn R (ppb/d)	avg R (ppb/d) in top50	avg R (ppb/d) in top10	avg R (ppb/d) in top03	fraction of total R in top50	fraction of total R in top10	fraction of total R in top03
Pacific	L-O3	ATom1	1.42	1.02	2.42	4.53	6.44	85%	32%	14%
Pacific	L-O3	ATom2	1.05	0.94	1.65	2.44	2.84	78%	23%	8%
Pacific	L-O3	ATom3	1.42	1.23	2.20	3.65	5.20	77%	26%	11%
Pacific	L-O3	ATom4	1.43	1.01	2.41	4.57	5.59	84%	32%	12%

Atlantic	L-O3	ATom1	2.12	1.18	3.73	6.12	7.37	88%	29%	11%
Atlantic	L-O3	ATom2	1.61	0.99	2.77	5.51	7.84	86%	34%	15%
Atlantic	L-O3	ATom3	1.84	1.27	3.04	6.10	9.06	83%	33%	15%
Atlantic	L-O3	ATom4	1.68	1.19	2.84	4.94	6.74	85%	30%	12%
C.Pacific	L-O3	ATom1	1.31	1.13	2.09	2.97	3.44	80%	23%	9%
C.Pacific	L-O3	ATom2	1.31	1.38	1.94	2.53	2.86	74%	19%	7%
C.Pacific	L-O3	ATom3	1.74	1.58	2.57	4.18	6.28	74%	24%	11%
C.Pacific	L-O3	ATom4	1.54	1.25	2.43	4.83	5.73	79%	32%	11%
E.Pacific	L-O3	ATom1	3.03	2.71	4.61	6.97	7.87	76%	23%	8%
E.Pacific	L-O3	ATom2	1.19	1.02	1.81	3.00	3.47	76%	26%	9%
E.Pacific	L-O3	ATom3	1.53	1.39	2.34	3.24	3.89	77%	21%	8%
E.Pacific	L-O3	ATom4	2.23	1.88	3.49	5.33	5.99	79%	24%	9%
T.Atlantic	L-O3	ATom1	2.59	1.89	4.36	6.60	7.85	84%	26%	10%
T.Atlantic	L-O3	ATom2	2.17	1.79	3.53	6.58	8.80	81%	30%	13%
T.Atlantic	L-O3	ATom3	2.47	1.90	3.97	7.29	10.20	81%	30%	13%
T.Atlantic	L-O3	ATom4	1.93	1.38	3.17	5.57	7.71	82%	29%	12%
Arctic	L-O3	ATom1	0.80	0.70	1.10	1.71	2.13	69%	22%	8%
Arctic	L-O3	ATom2	0.04	0.04	0.06	0.09	0.10	76%	22%	8%
Arctic	L-O3	ATom3	0.11	0.10	0.16	0.24	0.29	73%	22%	8%
Arctic	L-O3	ATom4	1.08	1.09	1.42	1.75	1.94	65%	16%	6%
S.Ocean	L-O3	ATom1	0.07	0.06	0.09	0.13	0.16	66%	21%	8%
S.Ocean	L-O3	ATom2	0.44	0.41	0.60	0.80	0.88	69%	19%	6%
S.Ocean	L-O3	ATom3	0.52	0.42	0.79	1.42	1.69	75%	27%	10%
S.Ocean	L-O3	ATom4	0.07	0.07	0.10	0.14	0.16	68%	19%	7%
Antarctic	L-O3	ATom3	0.25	0.25	0.33	0.43	0.48	65%	17%	6%
Antarctic	L-O3	ATom4	0.01	0.01	0.02	0.04	0.07	89%	35%	17%

L-CH4	react-ivity	deploy-ment	avg R (ppb/d)	mdn R (ppb/d)	avg R (ppb/d) in top50	top10	top03	fraction of total R in top50	top10	top03
Pacific	L-CH4	ATom1	0.63	0.50	1.05	1.71	2.12	84%	27%	10%
Pacific	L-CH4	ATom2	0.58	0.46	0.95	1.40	1.56	83%	24%	8%
Pacific	L-CH4	ATom3	0.63	0.51	1.00	1.58	1.98	79%	25%	10%
Pacific	L-CH4	ATom4	0.58	0.44	0.96	1.50	1.81	83%	26%	9%
Atlantic	L-CH4	ATom1	0.69	0.48	1.18	1.74	1.99	85%	25%	9%
Atlantic	L-CH4	ATom2	0.61	0.45	1.00	1.56	1.69	83%	26%	8%
Atlantic	L-CH4	ATom3	0.68	0.53	1.10	1.83	2.23	82%	27%	10%
Atlantic	L-CH4	ATom4	0.67	0.54	1.09	1.69	2.00	81%	25%	9%
C.Pacific	L-CH4	ATom1	0.71	0.62	1.10	1.56	1.77	78%	22%	8%
C.Pacific	L-CH4	ATom2	0.75	0.69	1.15	1.47	1.62	77%	20%	7%
C.Pacific	L-CH4	ATom3	0.85	0.85	1.26	1.74	2.28	74%	21%	8%
C.Pacific	L-CH4	ATom4	0.76	0.78	1.14	1.56	1.82	75%	21%	7%

E.Pacific	L-CH4	ATom1	1.18	1.19	1.70	2.26	2.52	72%	19%	7%
E.Pacific	L-CH4	ATom2	0.65	0.59	0.95	1.30	1.41	73%	20%	7%
E.Pacific	L-CH4	ATom3	0.74	0.65	1.07	1.36	1.48	73%	19%	6%
E.Pacific	L-CH4	ATom4	0.94	0.95	1.40	1.97	2.20	75%	21%	7%
T.Atlantic	L-CH4	ATom1	0.82	0.68	1.29	1.74	1.98	79%	22%	7%
T.Atlantic	L-CH4	ATom2	0.75	0.72	1.18	1.62	1.72	78%	22%	7%
T.Atlantic	L-CH4	ATom3	0.89	0.80	1.39	2.00	2.40	78%	22%	8%
T.Atlantic	L-CH4	ATom4	0.84	0.74	1.29	1.82	2.09	77%	22%	8%
Arctic	L-CH4	ATom1	0.21	0.17	0.29	0.46	0.56	72%	23%	8%
Arctic	L-CH4	ATom2	0.01	0.01	0.01	0.01	0.02	81%	25%	10%
Arctic	L-CH4	ATom3	0.02	0.02	0.04	0.07	0.10	81%	29%	13%
Arctic	L-CH4	ATom4	0.22	0.20	0.31	0.41	0.47	69%	18%	7%
S.Ocean	L-CH4	ATom1	0.02	0.02	0.04	0.06	0.07	70%	23%	9%
S.Ocean	L-CH4	ATom2	0.28	0.24	0.43	0.59	0.66	76%	21%	7%
S.Ocean	L-CH4	ATom3	0.18	0.15	0.29	0.52	0.65	78%	29%	11%
S.Ocean	L-CH4	ATom4	0.03	0.02	0.04	0.06	0.07	72%	22%	8%
Antarctic	L-CH4	ATom3	0.10	0.09	0.14	0.20	0.22	70%	21%	7%
Antarctic	L-CH4	ATom4	0.00	0.00	0.00	0.01	0.01	91%	38%	14%

L-CO	react-	deploy-	avg R	mdn R	avg R (ppb/d) in			fraction of total R in		
	ivity	ment	(ppb/d)	(ppb/d)	top50	top10	top03	top50	top10	top03
Pacific	L-CO	ATom1	1.30	1.08	2.01	3.36	4.29	78%	26%	10%
Pacific	L-CO	ATom2	1.15	1.15	1.61	2.17	2.56	70%	19%	7%
Pacific	L-CO	ATom3	1.49	1.34	2.10	3.23	4.56	70%	22%	9%
Pacific	L-CO	ATom4	1.49	1.25	2.35	4.08	4.92	79%	27%	10%
Atlantic	L-CO	ATom1	2.11	1.76	3.50	5.98	7.83	83%	28%	11%
Atlantic	L-CO	ATom2	1.76	1.26	2.84	5.95	8.76	81%	34%	15%
Atlantic	L-CO	ATom3	1.94	1.49	2.92	5.71	8.87	75%	30%	14%
Atlantic	L-CO	ATom4	1.80	1.52	2.83	4.92	7.42	79%	27%	13%
C.Pacific	L-CO	ATom1	1.21	1.07	1.66	2.30	2.62	69%	19%	7%
C.Pacific	L-CO	ATom2	1.42	1.43	1.78	2.26	2.57	63%	16%	6%
C.Pacific	L-CO	ATom3	1.76	1.64	2.36	3.69	5.55	67%	21%	10%
C.Pacific	L-CO	ATom4	1.59	1.35	2.28	4.10	4.91	72%	26%	9%
E.Pacific	L-CO	ATom1	2.45	2.37	3.31	4.58	5.17	68%	19%	7%
E.Pacific	L-CO	ATom2	1.53	1.39	1.96	2.85	3.34	64%	19%	7%
E.Pacific	L-CO	ATom3	1.71	1.68	2.20	2.82	3.25	64%	17%	6%
E.Pacific	L-CO	ATom4	2.40	2.18	3.26	4.70	5.65	68%	20%	8%
T.Atlantic	L-CO	ATom1	2.67	2.19	4.14	6.74	8.54	77%	25%	10%
T.Atlantic	L-CO	ATom2	2.41	1.86	3.70	7.22	10.05	77%	30%	13%
T.Atlantic	L-CO	ATom3	2.55	1.98	3.70	6.99	10.24	73%	28%	12%
T.Atlantic	L-CO	ATom4	2.12	1.67	3.14	5.81	8.69	74%	28%	13%

Arctic	L-CO	ATom1	1.03	0.93	1.44	2.28	2.86	70%	22%	9%
Arctic	L-CO	ATom2	0.05	0.04	0.07	0.11	0.12	81%	24%	8%
Arctic	L-CO	ATom3	0.14	0.11	0.22	0.41	0.53	81%	29%	12%
Arctic	L-CO	ATom4	1.33	1.30	1.56	1.91	2.10	59%	15%	5%
S.Ocean	L-CO	ATom1	0.10	0.09	0.13	0.19	0.23	67%	20%	7%
S.Ocean	L-CO	ATom2	0.62	0.60	0.82	1.05	1.22	66%	17%	6%
S.Ocean	L-CO	ATom3	0.64	0.57	0.85	1.33	1.50	67%	21%	7%
S.Ocean	L-CO	ATom4	0.08	0.07	0.12	0.21	0.27	73%	27%	10%
Antarctic	L-CO	ATom3	0.45	0.44	0.55	0.69	0.76	61%	15%	5%
Antarctic	L-CO	ATom4	0.01	0.00	0.01	0.02	0.03	90%	38%	16%

j-O1D	j-value	deploy-ment	avg J 1e-5 /s	mdn J 1e-5 /s	avg J (1e-5 /s) in top50	avg J (1e-5 /s) in top10	avg J (1e-5 /s) in top03	fraction of total J in top50	fraction of total J in top10	fraction of total J in top03
Pacific	j-O1D	ATom1	1.30	1.44	1.89	2.24	2.34	73%	17%	5%
Pacific	j-O1D	ATom2	1.31	1.28	1.94	2.64	2.81	74%	20%	7%
Pacific	j-O1D	ATom3	1.28	1.21	1.86	2.44	2.61	73%	19%	6%
Pacific	j-O1D	ATom4	1.24	1.33	1.85	2.26	2.39	75%	18%	6%
Atlantic	j-O1D	ATom1	1.25	1.46	1.82	2.15	2.27	73%	17%	6%
Atlantic	j-O1D	ATom2	1.25	1.29	1.79	2.29	2.42	72%	18%	6%
Atlantic	j-O1D	ATom3	1.21	1.19	1.74	2.28	2.38	72%	19%	6%
Atlantic	j-O1D	ATom4	1.18	1.33	1.73	2.05	2.15	74%	17%	6%
C.Pacific	j-O1D	ATom1	1.67	1.77	2.08	2.30	2.41	62%	14%	4%
C.Pacific	j-O1D	ATom2	1.76	1.79	2.26	2.74	2.86	64%	16%	5%
C.Pacific	j-O1D	ATom3	1.72	1.68	2.17	2.54	2.68	63%	15%	5%
C.Pacific	j-O1D	ATom4	1.57	1.68	2.02	2.25	2.33	65%	14%	5%
E.Pacific	j-O1D	ATom1	1.86	1.92	2.14	2.33	2.38	57%	13%	4%
E.Pacific	j-O1D	ATom2	1.44	1.48	1.79	2.10	2.18	62%	15%	5%
E.Pacific	j-O1D	ATom3	1.66	1.64	2.01	2.26	2.36	61%	14%	4%
E.Pacific	j-O1D	ATom4	1.95	2.05	2.27	2.46	2.54	58%	13%	4%
T.Atlantic	j-O1D	ATom1	1.55	1.71	1.95	2.21	2.31	63%	14%	5%
T.Atlantic	j-O1D	ATom2	1.61	1.63	1.99	2.36	2.45	62%	15%	5%
T.Atlantic	j-O1D	ATom3	1.58	1.55	1.97	2.33	2.40	63%	15%	5%
T.Atlantic	j-O1D	ATom4	1.46	1.55	1.88	2.10	2.18	65%	15%	5%
Arctic	j-O1D	ATom1	0.51	0.51	0.67	0.80	0.85	65%	16%	5%
Arctic	j-O1D	ATom2	0.01	0.01	0.02	0.02	0.02	79%	23%	8%
Arctic	j-O1D	ATom3	0.04	0.03	0.06	0.09	0.11	82%	26%	9%
Arctic	j-O1D	ATom4	0.73	0.71	0.83	0.96	1.02	58%	13%	4%
S.Ocean	j-O1D	ATom1	0.07	0.06	0.09	0.13	0.14	68%	19%	6%
S.Ocean	j-O1D	ATom2	1.26	1.32	1.68	2.04	2.14	67%	16%	5%
S.Ocean	j-O1D	ATom3	0.79	0.75	1.04	1.32	1.43	66%	17%	6%
S.Ocean	j-O1D	ATom4	0.03	0.03	0.05	0.07	0.08	71%	22%	7%

Antarctic	j-O1D	ATom3	0.50	0.43	0.66	0.90	0.98	66%	18%	6%
Antarctic	j-O1D	ATom4	0.00	0.00	0.01	0.01	0.01	99%	45%	16%

260

j-NO2	j-value	deploy-ment	avg J 1e-2 /s	mdn J 1e-2 /s	avg J (1e-2 /s) in top50	top10	top03	fraction of total J in top50	top10	top03
Pacific	j-NO2	ATom1	0.48	0.52	0.61	0.71	0.75	64%	15%	5%
Pacific	j-NO2	ATom2	0.50	0.53	0.62	0.72	0.76	63%	15%	5%
Pacific	j-NO2	ATom3	0.49	0.53	0.60	0.67	0.70	61%	14%	4%
Pacific	j-NO2	ATom4	0.47	0.50	0.62	0.73	0.78	66%	15%	5%
Atlantic	j-NO2	ATom1	0.48	0.52	0.61	0.70	0.74	64%	15%	5%
Atlantic	j-NO2	ATom2	0.50	0.54	0.62	0.70	0.75	62%	14%	5%
Atlantic	j-NO2	ATom3	0.49	0.52	0.61	0.69	0.73	62%	14%	5%
Atlantic	j-NO2	ATom4	0.47	0.49	0.60	0.70	0.74	64%	15%	5%
C.Pacific	j-NO2	ATom1	0.50	0.53	0.59	0.65	0.68	59%	13%	4%
C.Pacific	j-NO2	ATom2	0.53	0.55	0.62	0.71	0.74	59%	13%	4%
C.Pacific	j-NO2	ATom3	0.52	0.55	0.60	0.67	0.70	58%	13%	4%
C.Pacific	j-NO2	ATom4	0.49	0.52	0.59	0.65	0.67	60%	13%	4%
E.Pacific	j-NO2	ATom1	0.56	0.60	0.65	0.70	0.73	58%	13%	4%
E.Pacific	j-NO2	ATom2	0.51	0.54	0.59	0.63	0.66	58%	12%	4%
E.Pacific	j-NO2	ATom3	0.53	0.56	0.61	0.69	0.72	57%	13%	4%
E.Pacific	j-NO2	ATom4	0.58	0.63	0.68	0.72	0.75	58%	13%	4%
T.Atlantic	j-NO2	ATom1	0.51	0.55	0.61	0.67	0.70	59%	13%	4%
T.Atlantic	j-NO2	ATom2	0.54	0.56	0.61	0.67	0.69	57%	13%	4%
T.Atlantic	j-NO2	ATom3	0.53	0.56	0.62	0.68	0.72	59%	13%	4%
T.Atlantic	j-NO2	ATom4	0.49	0.51	0.58	0.65	0.67	59%	13%	4%
Arctic	j-NO2	ATom1	0.57	0.63	0.71	0.80	0.84	62%	14%	4%
Arctic	j-NO2	ATom2	0.05	0.03	0.08	0.12	0.12	83%	26%	8%
Arctic	j-NO2	ATom3	0.11	0.09	0.18	0.27	0.29	79%	24%	8%
Arctic	j-NO2	ATom4	0.80	0.80	0.90	1.02	1.05	56%	13%	4%
S.Ocean	j-NO2	ATom1	0.13	0.13	0.19	0.24	0.27	71%	19%	6%
S.Ocean	j-NO2	ATom2	0.61	0.68	0.73	0.79	0.82	60%	13%	4%
S.Ocean	j-NO2	ATom3	0.49	0.53	0.60	0.66	0.68	60%	14%	4%
S.Ocean	j-NO2	ATom4	0.09	0.08	0.14	0.21	0.24	75%	23%	8%
Antarctic	j-NO2	ATom3	0.49	0.48	0.56	0.64	0.68	58%	13%	4%
Antarctic	j-NO2	ATom4	0.01	0.00	0.02	0.04	0.06	99%	48%	22%

Table notes: The primary ocean basins (Pacific & Atlantic) use the over-ocean flight data from 53°S to 60°N, see Figure 2. The tropical ocean sections are Central Pacific (30°S-30°N, near Dateline), Eastern Pacific (0°-30°N, ~121°W), and Tropical Atlantic (30°S-30°N). All 10 s data are weighted inversely by frequency of occurrence in 10º latitude by 100 hPa bins and by

cosine(latitude). For the high-latitude sections – Arctic (66°N-90°N), Southern Ocean (66°S-55°S), and Antarctica (90°S-66°S) – parcels are weighted only by frequency of occurrence in 100 hPa bins.

3.2 Curtain plots

The spatial structures and variability of P-O3 as sampled by the four ATom transects over the Pacific Ocean are presented as 2D latitude-height curtain plots in Fig. 6. The full set of plots covering all four reactivities and also the Atlantic Ocean are shown sequentially in Fig. 6-13. For these curtain plots, the 10 s reactivities (2 km by 80 m thick parcels) are averaged and plotted in 1° latitude by 200 m thick cells. For both Atlantic and Pacific basins, the reactivities (L-O3, L-CH4, L-CO) generally follow the sun with more southerly hot parcels in ATom-23 (Feb, Oct) and northerly hot parcels in ATom-14 (Aug, May). The P-O3 hot spots have no simple seasonality, bring dominated by middle- to upper-tropospheric regions with high NOx presumably from the outflow of deep convection from the nearby continents.

Because the E. Pacific flights (~121 °W) are clearly influenced by continental outflow from Northern and Central America, we separate them from the C. Pacific in our examination of the tropical oceans (see Fig. 2). Curtain plots of the four reactivities for ATom-1234 in the C. Pacific are shown in Fig. 14-17; in the E. Pacific, in Fig. 18-21; and in the T. Atlantic, in Fig. 22-25. In terms of P-O3, the C. Pacific shows a few hot spots, but generally no large regions > 3 ppb/d. The T. Atlantic shows extensive regions in the middle-to-upper troposphere with P-O3 > 3 ppb/d; and these look like continental outflow with both NOx and HOx sources. The E. Pacific shows extensive 1-2 km thick, 10° latitude layers of mostly above 8 km. In the E. Pacific these P-O3 layers are clearly separated from the moderately high (ATom-23) to extremely high (ATom-14) L-O3 > 5 ppb/d layers below 8 km. The large L-O3 (and also L-CH4 and L-CO) layers contain highly reactive HOx-VOC chemistry but little NOx, and these are associated with continental outflow, see discussion in G2023. The T. Atlantic, in contrast with the C. Pacific, shows large 20-30° wide tropical regions below 8 km with L-O3 > 4 ppb/d, L-CH4 > 1.5 ppb/d and L-CO > 4 ppb/d. These regions follow the sun, northward in ATom-14 and southward in ATom-23. For L-O3 and L-CO, the T. Atlantic has 50% greater loss than the C. Pacific.

Overall, these figures (Fig. 6-25) show the dominance of the tropics (30°S - 30°N) for photochemical reactivity over the oceans. Only the northern mid-latitudes (30°N - 60°N) contribute almost a fifth tropics-like reactive region in summer (ATom-14), especially in the Atlantic.

Curtain profiles for the Arctic are presented only for ATom-1 (Fig. 26) and ATom-4 (Fig. 27) when there was enough sunlight to generate non-negligible reactivities. The very low reactivity statistics for ATom-23 Arctic are seen in Table 1. Stratospheric air parcels are excluded in these Arctic statistics. Reactivities appear moderately high, but the color scale is 3 times smaller than in Figures 6-25. Similar to the ocean basins, in the Arctic much of the P-O3 occurs above 8 km, and losses (L-O3, L-CH4, L-CO) occurs between 1 and 6 km. Curiously, there is a region of high L-CO above 10 km in the region of high P-O3. Notably, that rate (R4) is not sensitive to cold temperatures. Only one of the two Antarctic flights had enough sunlight to produce much reactivity (ATom-3, Fig. 28). Like the Arctic, P-O3 is concentrated in the upper troposphere, while L-O3 and L-CH4 are in the lower. Note that the color scale is 6-to-12 times smaller than in Fig. 6-25.

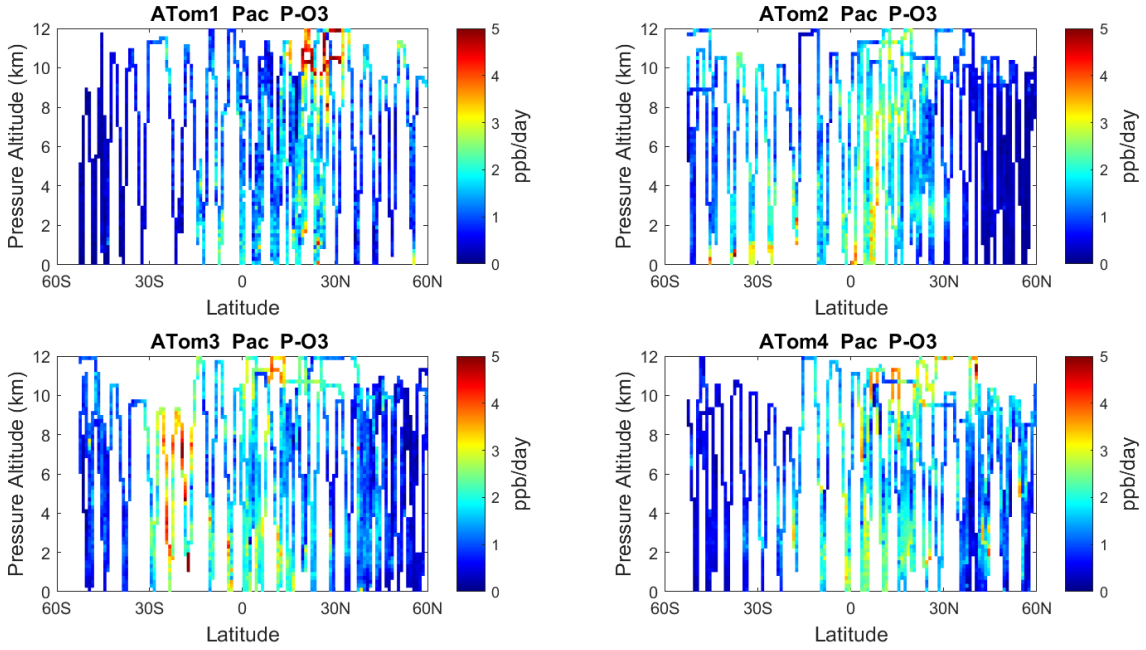

Figure 6. 2D curtain plots (altitude-latitude profiling) of P-O3 (ppb/day) in Pacific basin (53°S-60°N) for ATom-1234. In all these curtain plots, ATom 10s parcel data are weighted by cosine (latitude) and sampling frequency, and then they are averaged into 1° latitude and 200 m altitude bins.

305

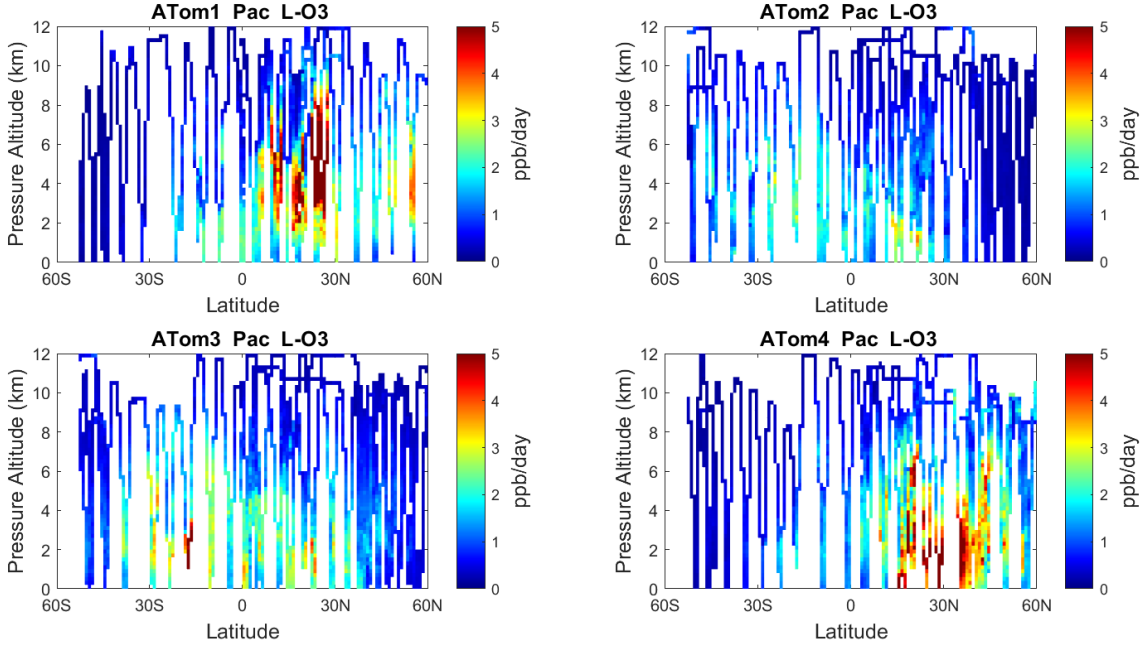

Figure 7. Curtain plots of L-O3 (ppb/day) in Pacific basin (53°S-60°N) for ATom-1234. See Fig. 6

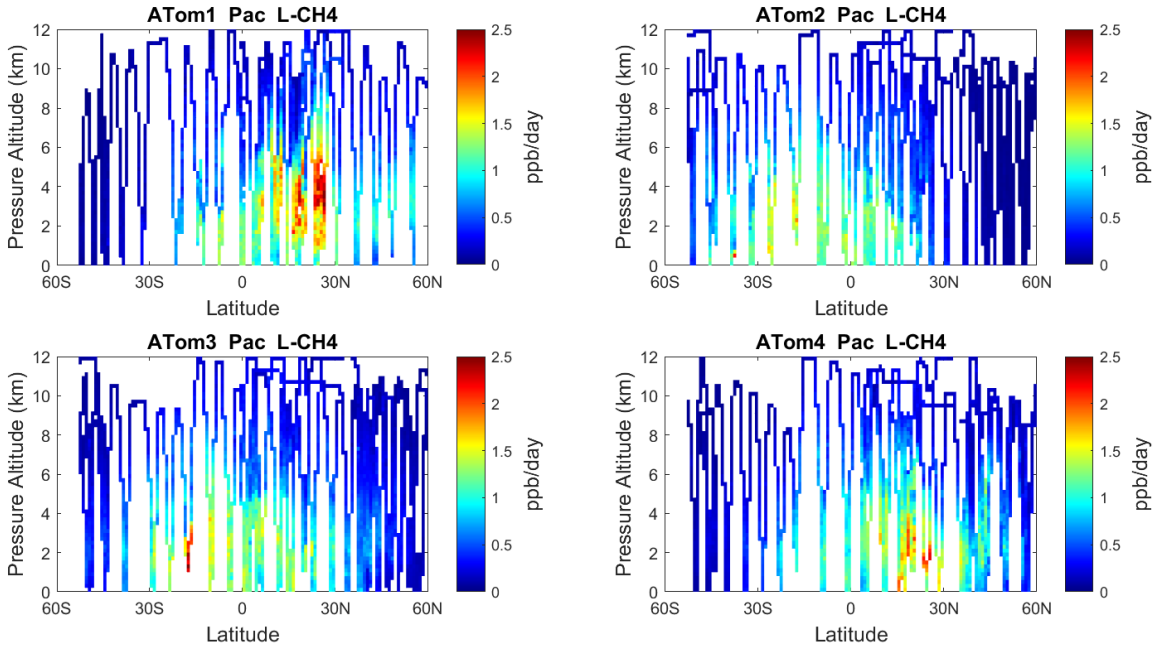

Figure 8. Curtain plots of L-CH4 (ppb/day) in Pacific basin (53°S-60°N) for ATom-1234. See Fig. 6

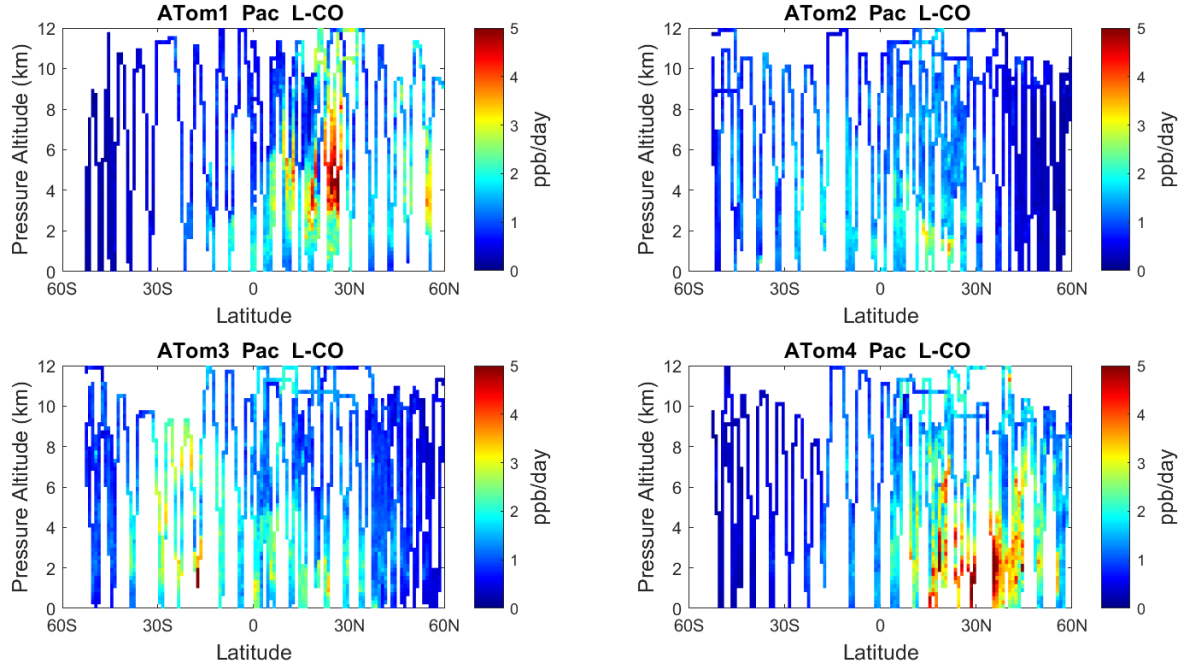

Figure 9. Curtain plots of L-CO (ppb/day) in Pacific basin (53°S-60°N) for ATom-1234. See Fig. 6

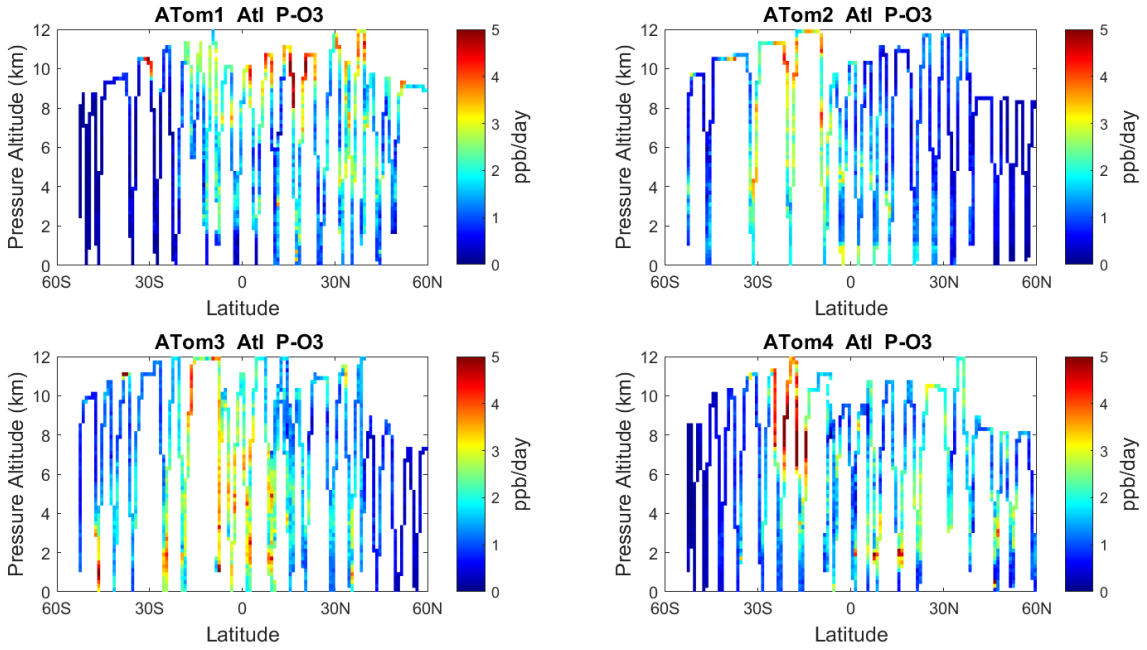

Figure 10. Curtain plots of P-O3 (ppb/day) in Atlantic basin (53°S-60°N) for ATom-1234. See Fig. 6.

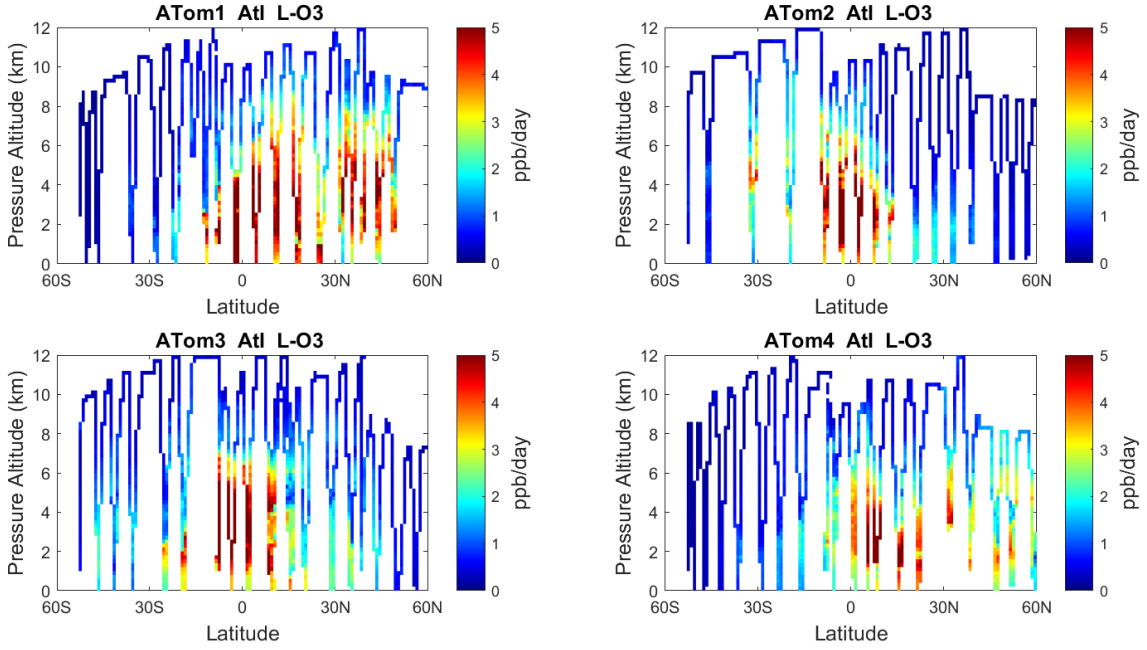

320

Figure 11. Curtain plots of L-O3 (ppb/day) in Atlantic basin (53°S-60°N) for ATom-1234. See Fig. 6.

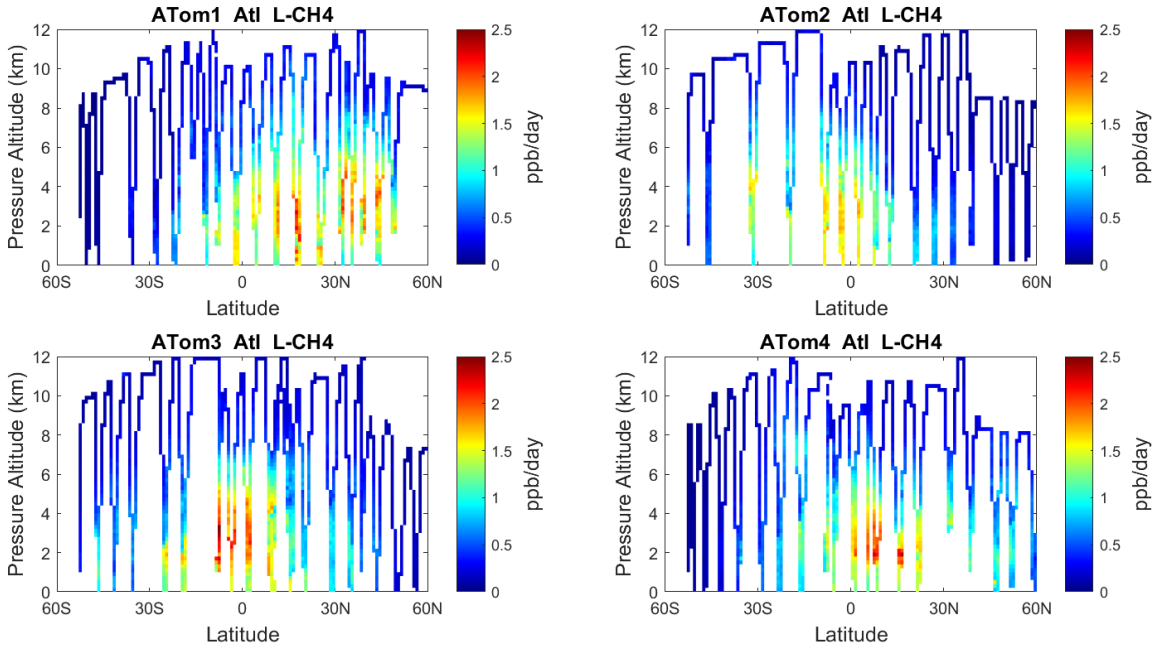

325 **Figure 12**. Curtain plots of L-CH4 (ppb/day) in Atlantic basin (53°S-60°N) for ATom-1234. See Fig. 6.

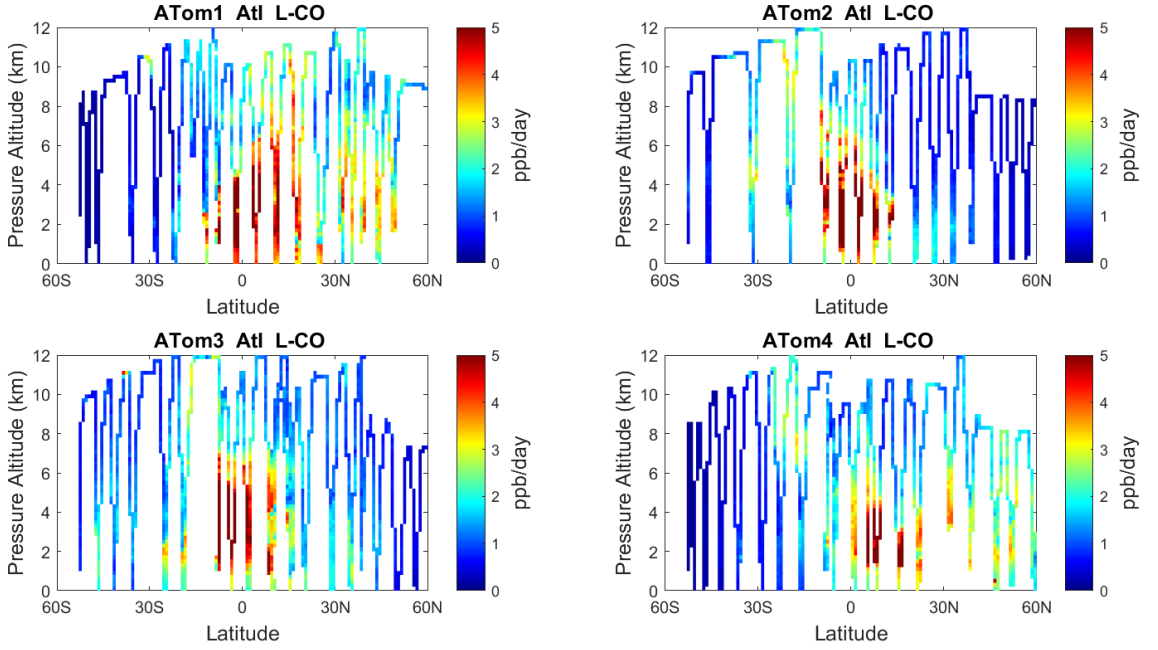

Figure 13. Curtain plots of L-CO (ppb/day) in Atlantic basin (53°S-60°N) for ATom-1234. See Fig. 6.

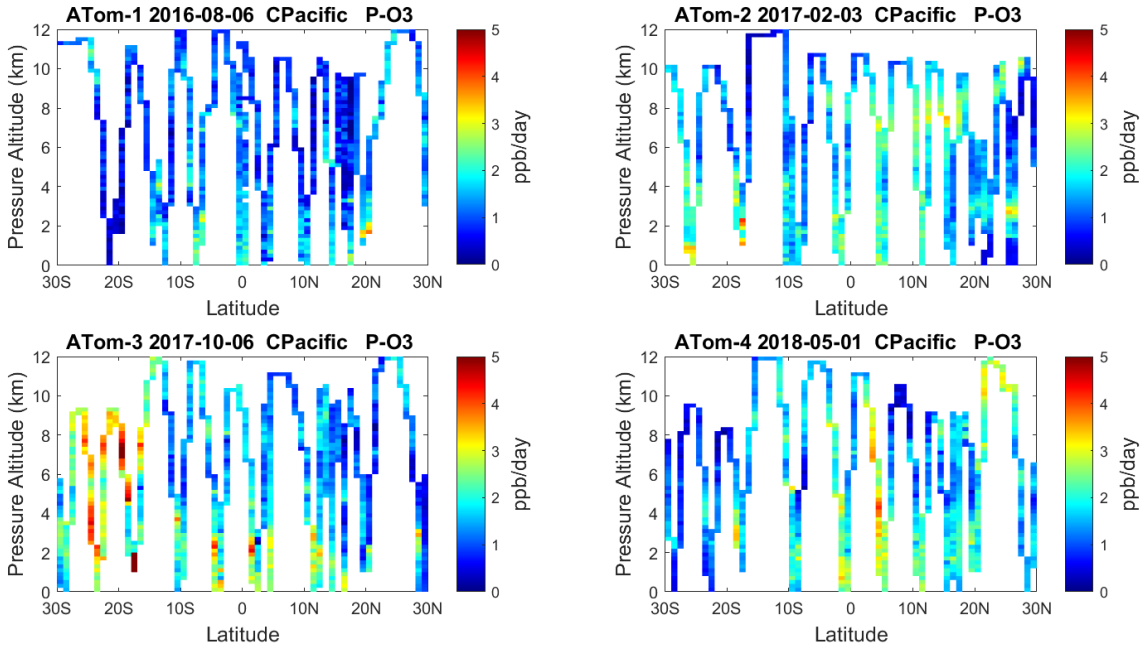

Figure 14. Curtain plots of P-O3 (ppb/day) in the tropical Central Pacific (30°S-30°N) for ATom-1234. See Fig. 6. The date of the flight crossing the equatorial Pacific for each deployment are given.

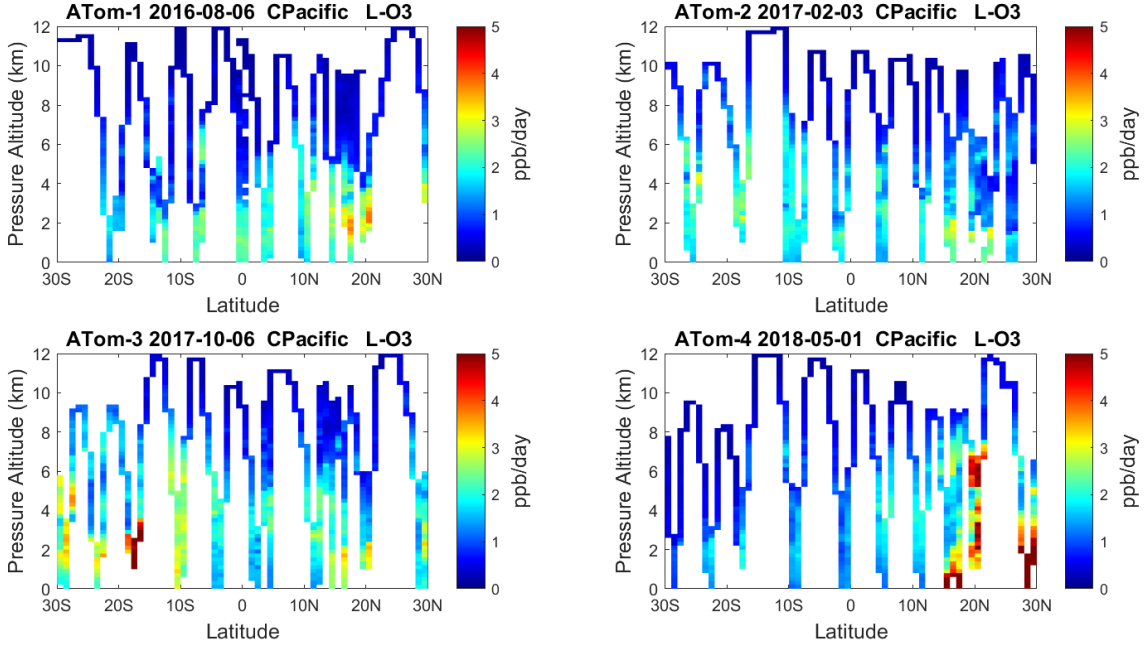

Figure 15. Curtain plots of L-O3 (ppb/day) in the tropical Central Pacific (30°S-30°N) for ATom-1234. See Fig. 6.

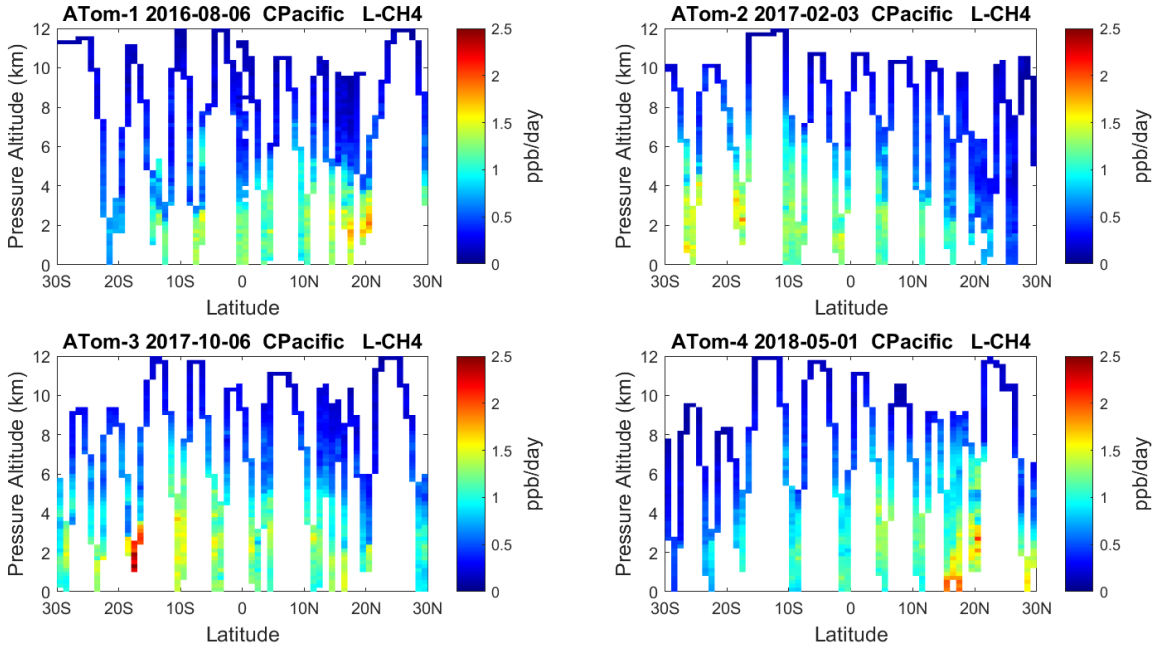

Figure 16. Curtain plots of L-CH4 (ppb/day) in the tropical Central Pacific (30°S-30°N) for ATom-1234. See Fig. 6.

340

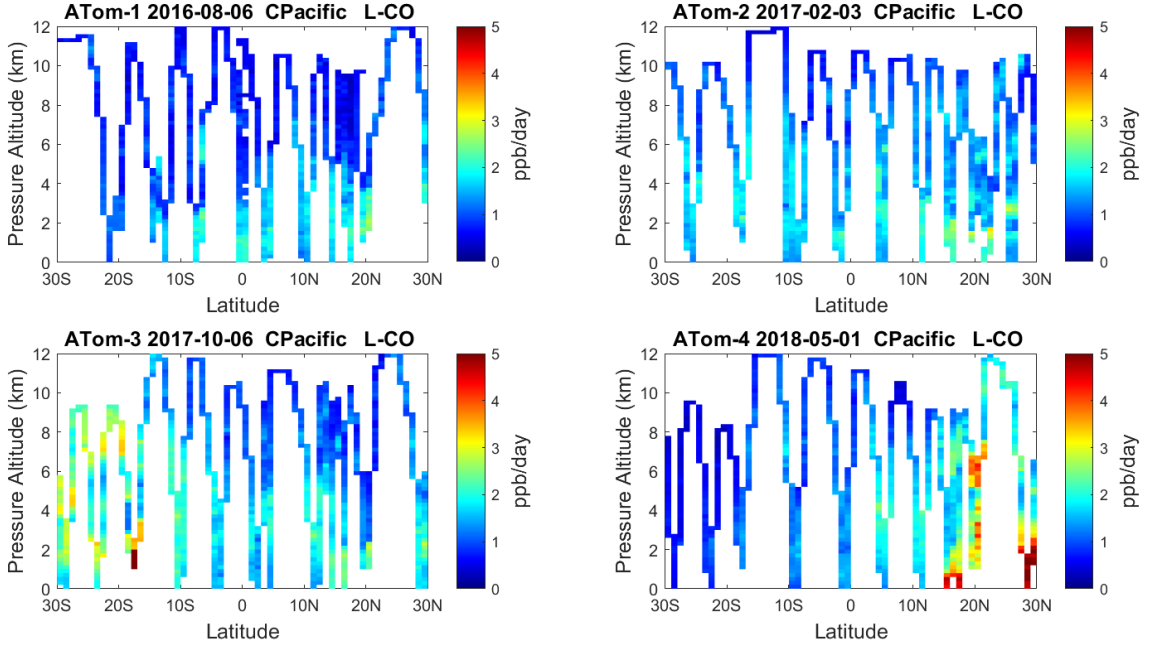

Figure 17. Curtain plots of L-CO (ppb/day) in the tropical Central Pacific (30°S-30°N) for ATom-1234. See Fig. 6.

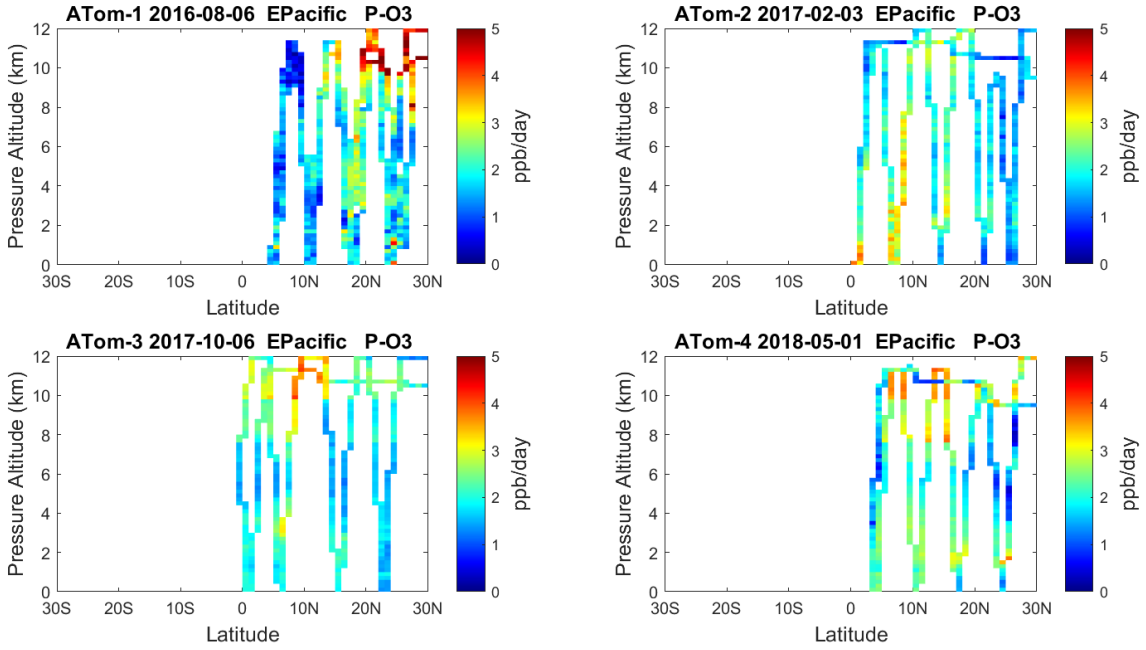

Figure 18. Curtain plots of P-O3 (ppb/day) in the tropical Eastern Pacific (0°-30°N) for ATom-1234. See Fig. 6.

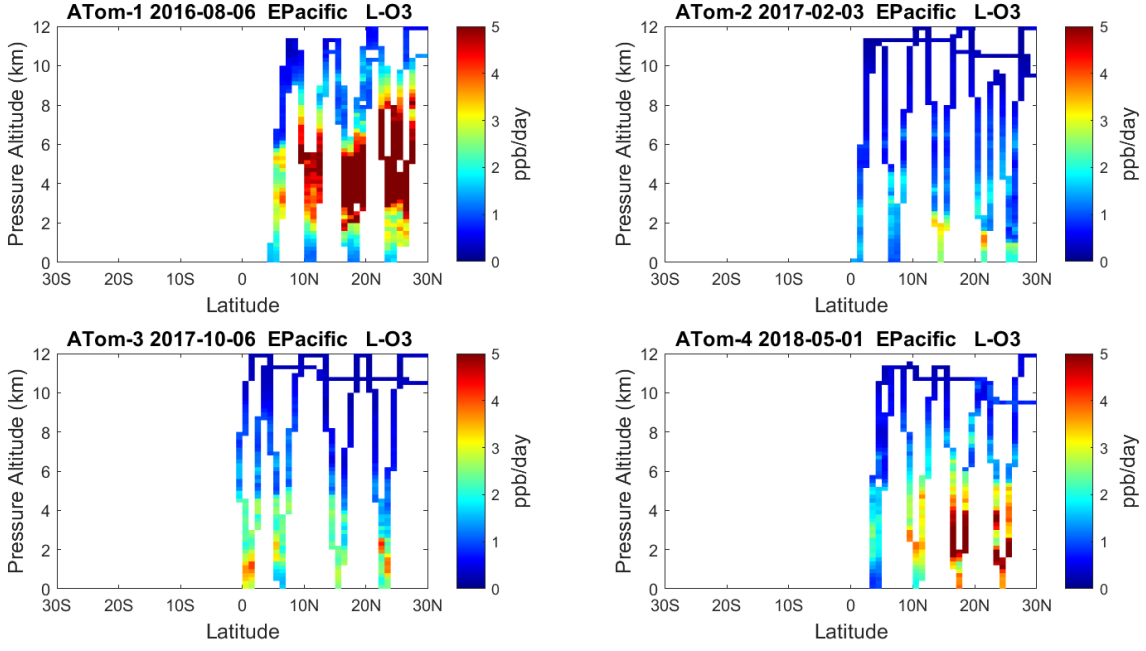

Figure 19. Curtain plots of L-O3 (ppb/day) in the tropical Eastern Pacific (0°-30°N) for ATom-1234. See Fig. 6.

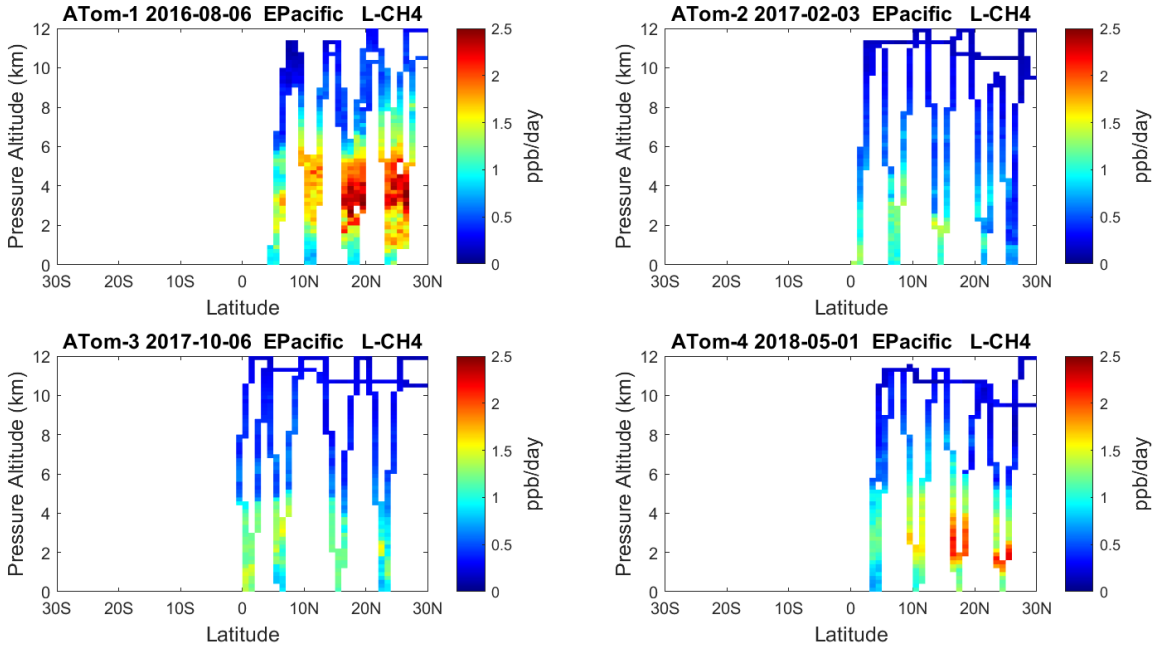

Figure 20. Curtain plots of L-CH4 (ppb/day) in the tropical Eastern Pacific (0°-30°N) for ATom-1234. See Fig. 6.

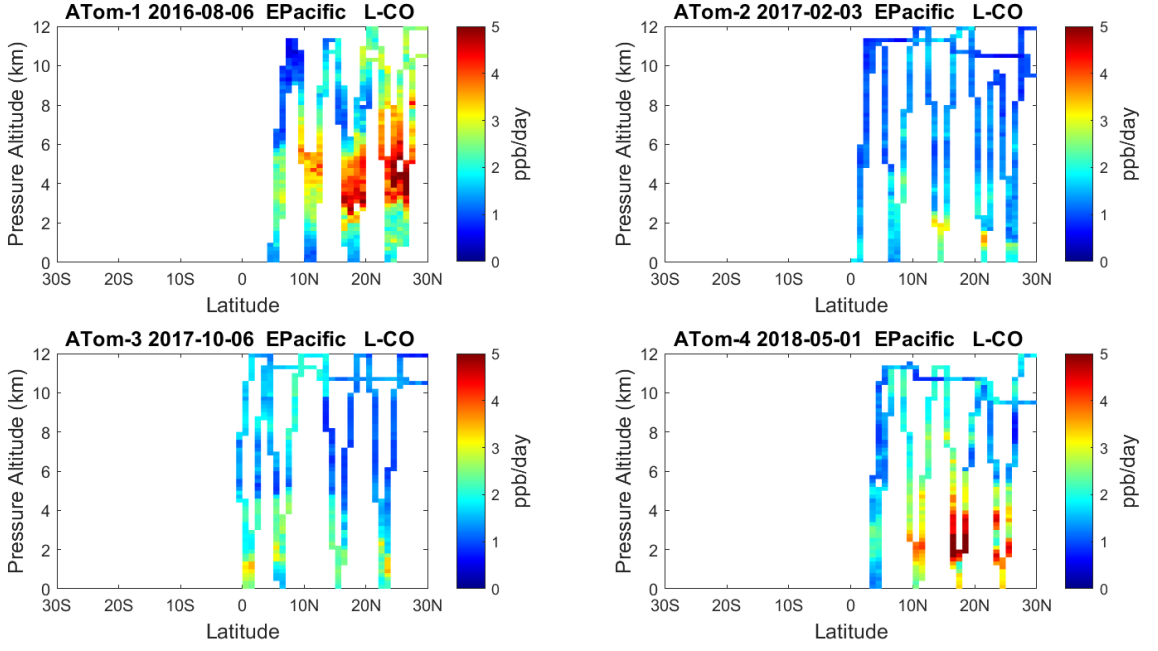

355

Figure 21. Curtain plots of L-CO (ppb/day) in the tropical Eastern Pacific (0°-30°N) for ATom-1234. See Fig. 6.

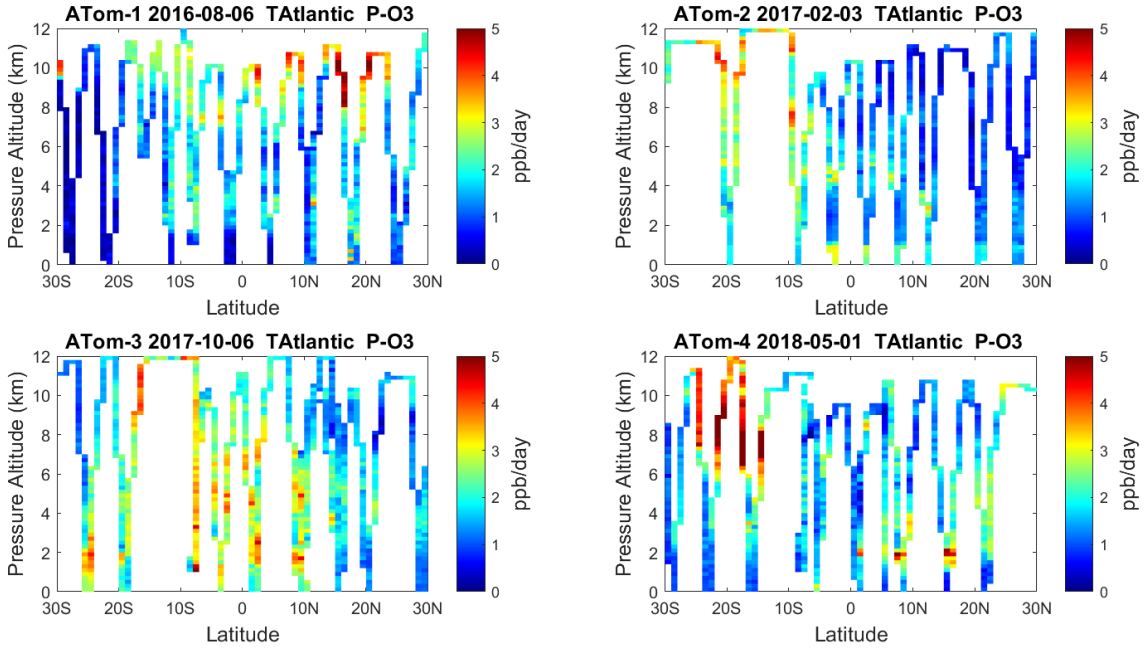

Figure 22. Curtain plots of P-O3 (ppb/day) in the tropical Atlantic (30°S-30°N) for ATom-1234. See Fig. 6.

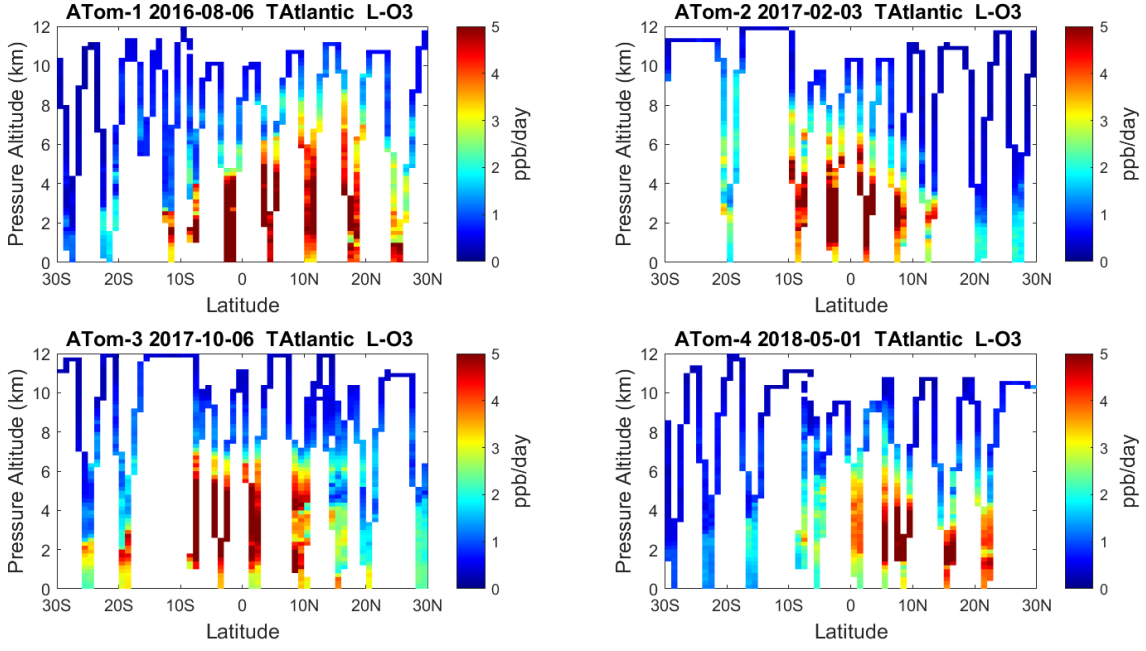

Figure 23. Curtain plots of L-O3 (ppb/day) in the tropical Atlantic (30°S-30°N) for ATom-1234. See Fig. 6.

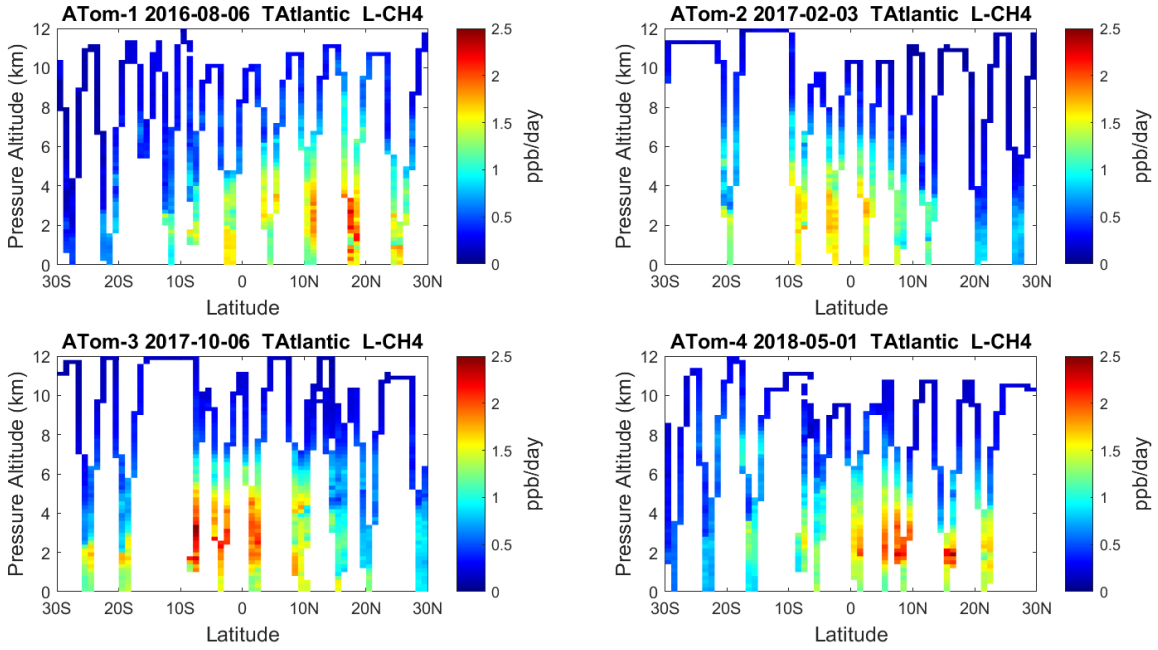

Figure 24. Curtain plots of L-CH4 (ppb/day) in the tropical Atlantic (30°S-30°N) for ATom-1234. See Fig. 6.

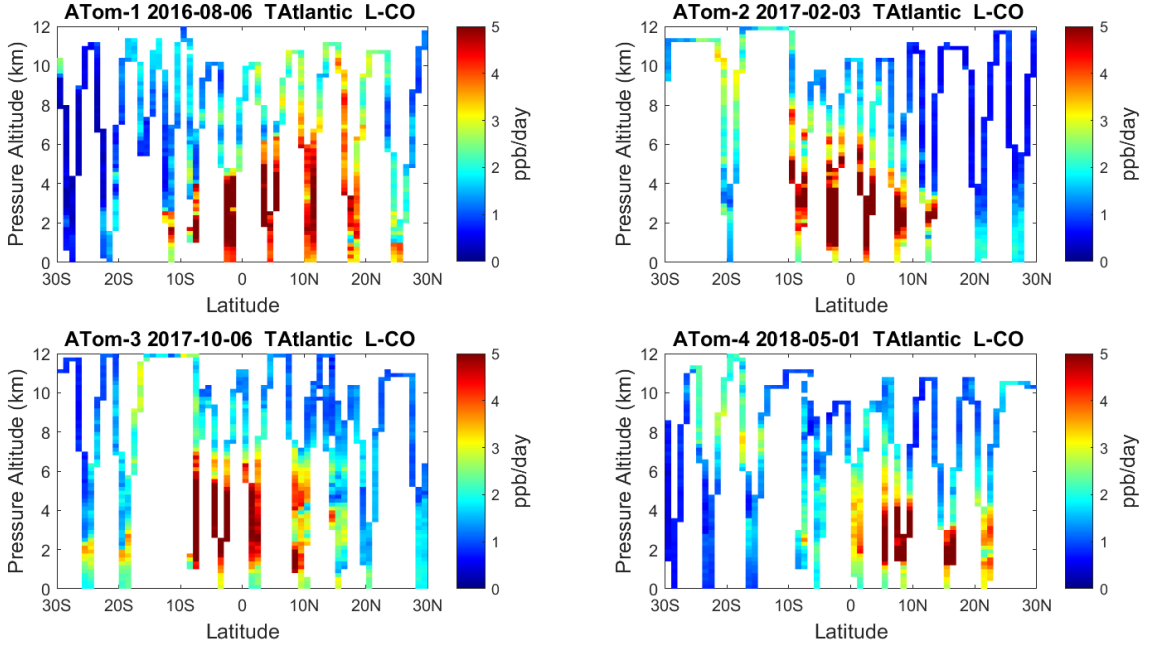

Figure 25. Curtain plots of L-CO (ppb/day) in the tropical Atlantic (30°S-30°N) for ATom-1234. See Fig. 6.

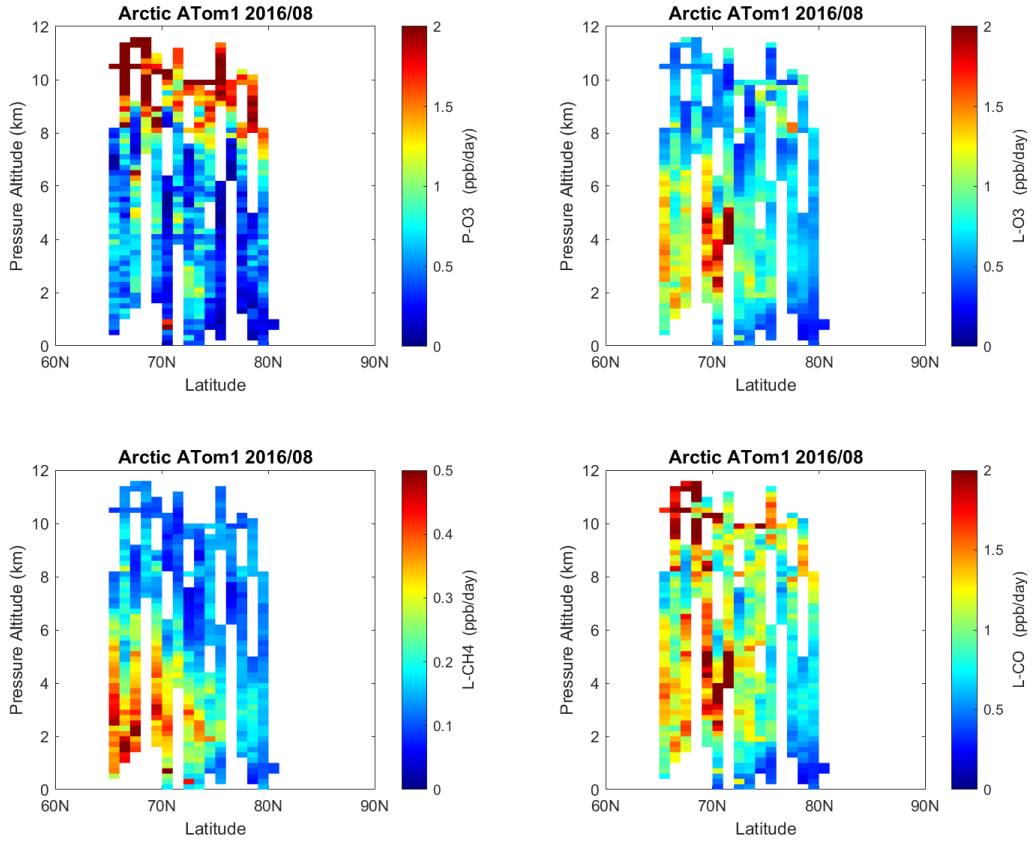

375 **Figure 26.** Curtain plots of the 4 reactivities (P-O3, L-O3, L-CH4, L-CO ppb/day) over the Arctic for ATom-1. Note the color bars have a much smaller range than in the Pacific and Atlantic basin plots. Troposphere-only parcels are shown, with stratosphere defined as (H_2O < 30 ppm) and (O_3 > 80 ppb) and (CO < 120 ppb). See Fig. 6.

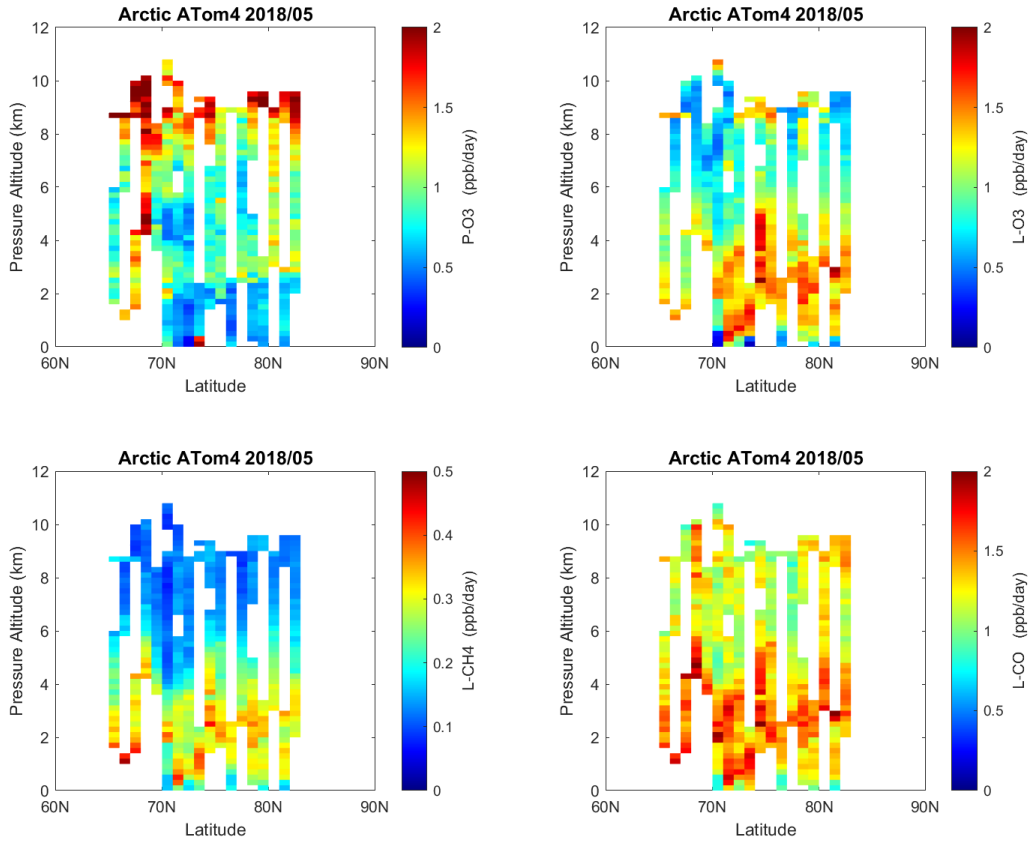

Figure 27. Curtain plots of the 4 reactivities (P-O3, L-O3, L-CH4, L-CO ppb/day) over the Arctic on ATom-4. Troposphere-only parcels, see Fig. 6 & 26.

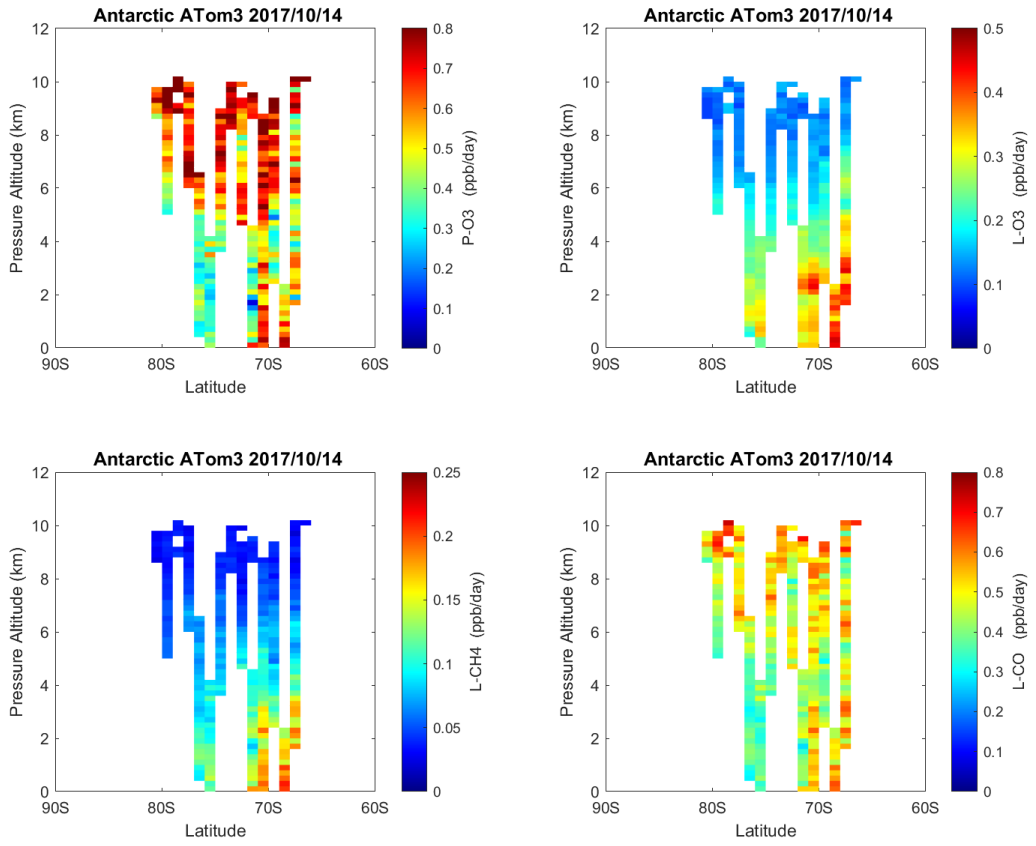

390

Figure 28. Curtain plots of the 4 reactivities (P-O3, L-O3, L-CH4, L-CO, ppb/day) over Antarctica on ATom-3. Note the color bars have a smaller range than in the Pacific and Atlantic and Arctic basin plots. Troposphere-only parcels. See Fig. 6 & 26.

3.3 Mean altitude profiles

Given the inherent synoptic variability plus the large seasonal shifts in chemical reactivity across the Pacific and Atlantic basins seen in the individual profiles (Figures 6-13), one might ask how useful or representative the four ATom transects are for testing model statistics. Because the 53°S-60°N Pacific and Atlantic transects contain the north-south seasonal shifts and most of the reactivity (see Southern Ocean, Arctic and Antarctic reactivities above), a mean profile should average over some of the synoptic variability and give us a seasonal variation in the basin-mean reactivity that could test chemistry-climate models. Seasonal variability in the mean reactivity profiles is clearly due to shifts in the chemical composition caused, for example, in the Atlantic by the cycle of African biomass burning and convection. A similar reasoning applies to basin-wide probability densities, see Section 3.4 below.

Altitude profiles of the weighted mean P-O3 for the three tropical basins and 4 deployments are compared in Fig. 29. For other reactivities, see Fig. 30-32. These profiles highlight the consistency in basin averages across the four ATom deployments with some exceptions. In the Pacific, the P-O3 profiles are similar, but ATom-1 is systematically less below 6 km. Although the hot spots of P-O3 are dominated by the higher altitudes, the mean profile shows only a modest increase above 10 km. In the Atlantic, ATom-3 has much greater P-O3 below 6 km, but above 8 km, all deployments show a wide range of mean values, with ATom-1 exceeding 2.5 ppb/d above 10 km. For L-O3 and L-CH4, the spread is much larger with ATom-1 largest in both Pacific and Atlantic. For L-CO, the variation is different still, with a relatively large spread, e.g., in the Pacific, ATom-4 is 50-100% larger than ATom-2.

Mean reactivity profiles for the three tropical basins are shown in Fig. 33-36. Here the C. Pacific shows small variability across deployments (except for P-O3 minimum in ATom-1) while the E. Pacific shows little range in P-O3 but very large L-O3, L-CH4 and L-CO below 8 km for ATom-14. The end of the biomass burning season in Central America (15°N-20°N) is probably the cause of the peak L-O3 below 6 km in ATom-4 (May); while the start of the North American Monsoon season is probably the cause of the extensive highly reactive deep-convection layer (2-10 km) in ATom-1 (August). With this high level of variability, it will be important to re-examine the time period of the ATom flights with a chemistry-transport model to assess the spatio-temporal scales and origins of these events.

In the Arctic (Fig. 37), ATom-14 show similar profiles but with different shapes for each reactivity; while ATom-23 have negligible reactivities as expected from the limited sunlight. P-O3 peaks at 8-12 km with values from 1-2 ppb/day; while L-O3 and L-CH4 peak around 2-4 km. As in the curtain plots, L-CO peaks with L-O3 in the lower troposphere and also with P-O3 in the upper. The reactivities in the Arctic, even in summer are less than the average over the Pacific and Atlantic oceans and thus have little impact on the global O_3 or CH_4 budgets.

In the Antarctic (Fig. 38), reactivities are much less than the Arctic and only reported for ATom-3; however, due to the limited sampling of the Antarctic, this may underestimate its role in the global or even regional budgets. The S. Ocean reactivity profiles (Fig. 39) can be directly compared with the Arctic (Fig. 37) since both use the same axes scale. For L-CH4, they are almost identical (S. Ocean ATom-23 with Arctic ATom-14), and the differences in L-CO are simply attributable to the smaller CO abundance in the southern hemisphere. The O_3 reactivities are much less in the S. Ocean, however, and the there is no peak in P-O3 (1-2 ppb/d) above 8 km as found in the Arctic. The Arctic clearly has much greater pollution in the upper troposphere, including possibly aviation NOx sources.

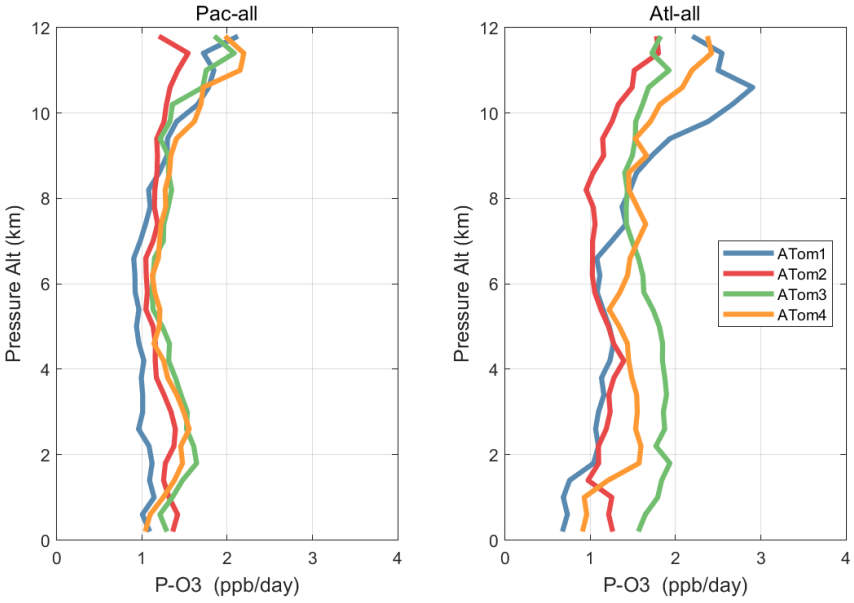

Figure 29. Mean altitude profile of P-O3 (ppb/day) over the Pacific and Atlantic basins (53°S-60°N) for ATom-1234.

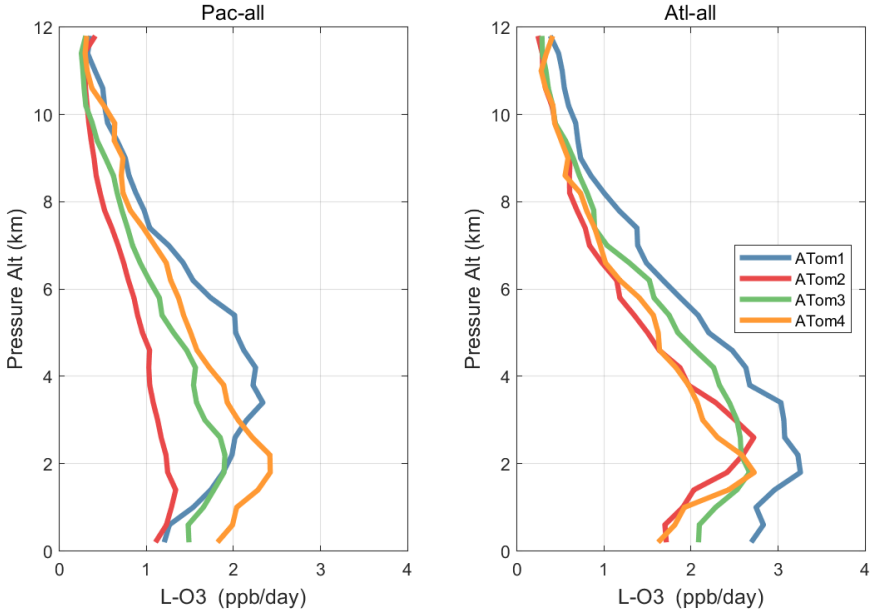

435 **Figure 30.** Mean altitude profile of L-O3 (ppb/day) over the Pacific and Atlantic basins (53°S-60°N) for ATom-1234.

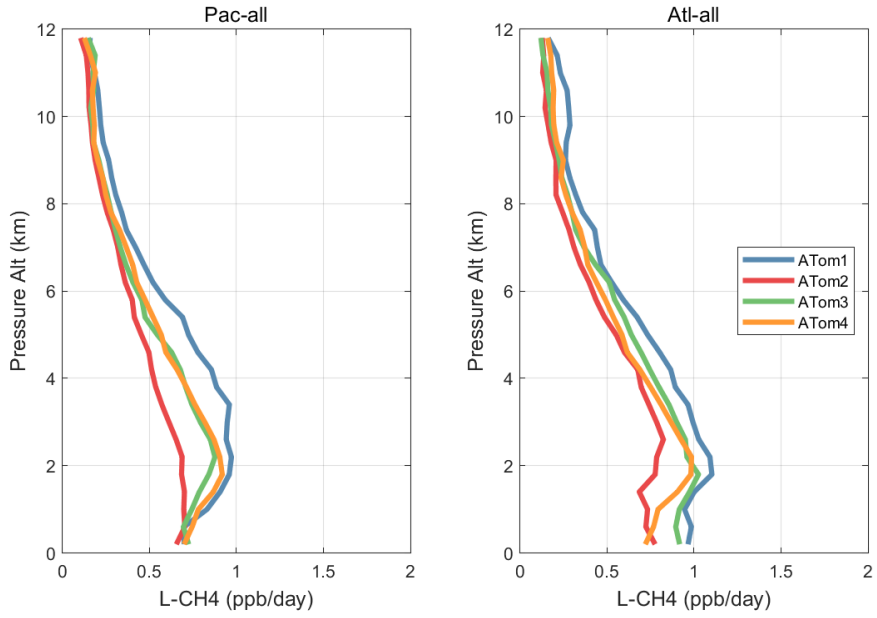

Figure 31. Mean altitude profile of L-CH4 (ppb/day) over the Pacific and Atlantic basins (53°S-60°N) for ATom-1234.

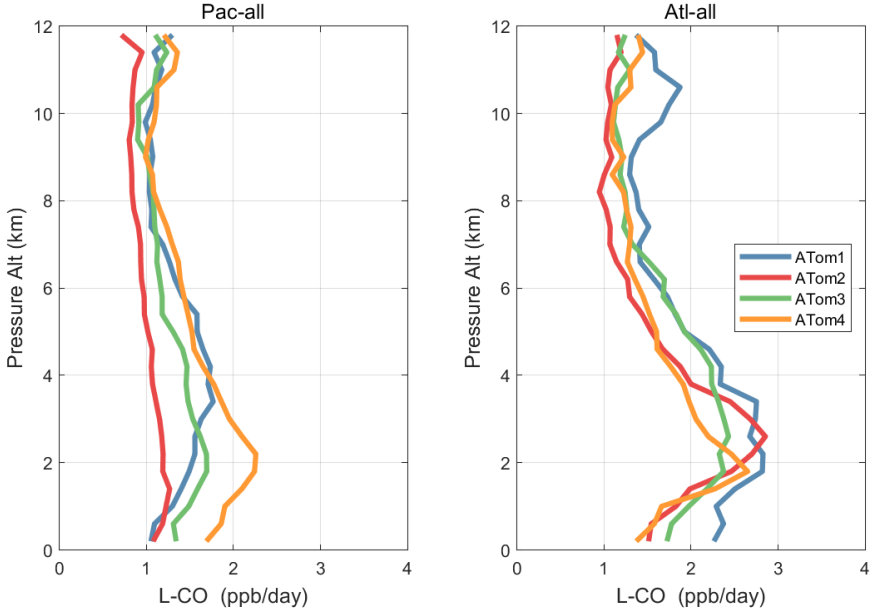

440

Figure 32. Mean altitude profile of L-CO (ppb/day) over the Pacific and Atlantic basins (53°S-60°N) for ATom-1234.

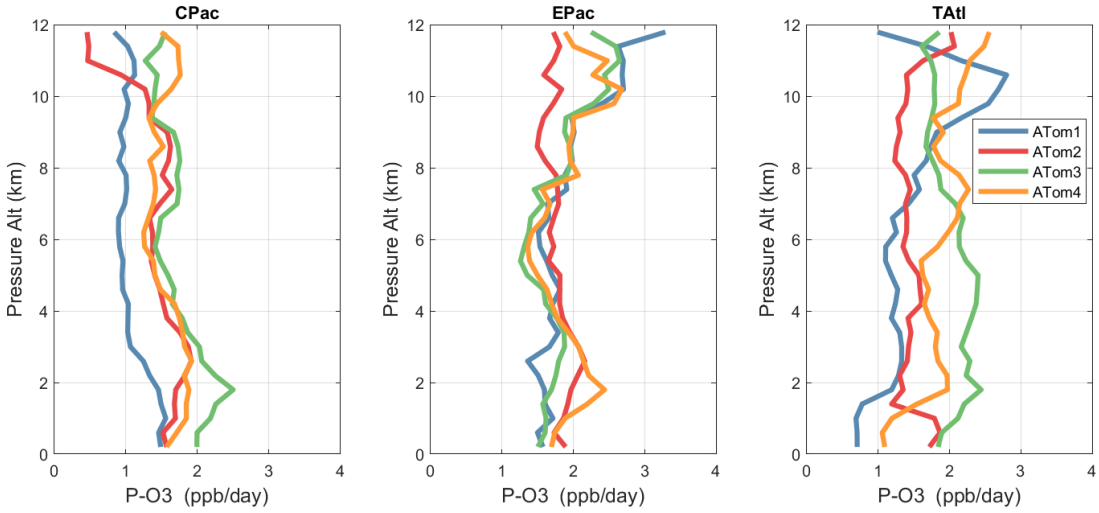

Figure 33. Mean altitude profile of P-O3 (ppb/day) over the 3 tropical basins for ATom-1234.

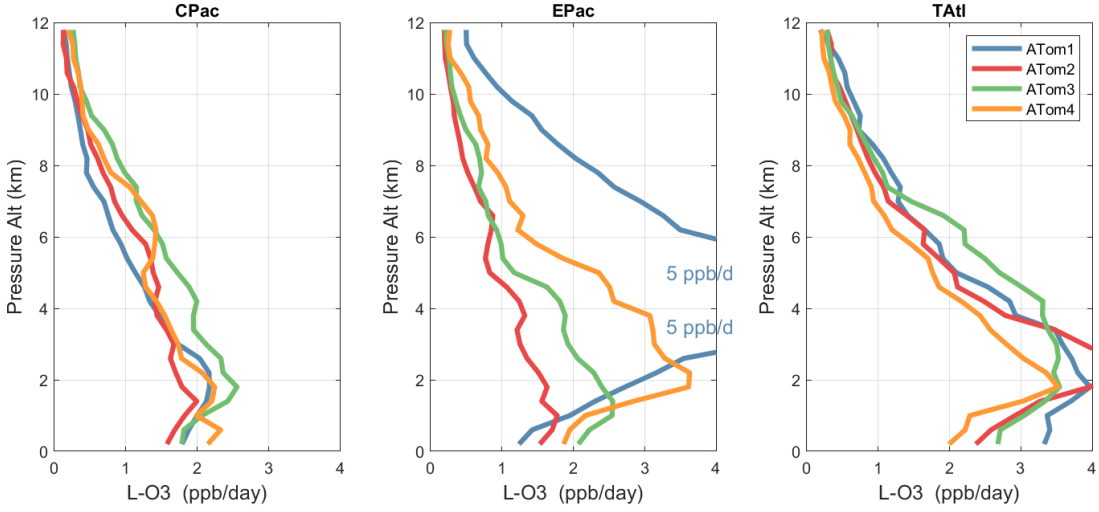

Figure 34. Mean altitude profile of L-O3 (ppb/day) over the 3 tropical basins for ATom-1234.

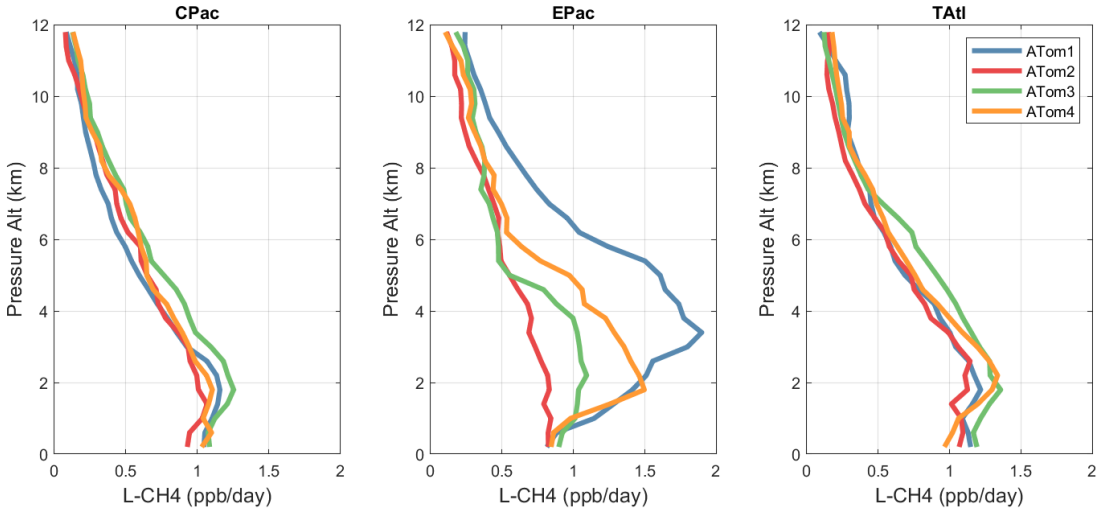

Figure 35. Mean altitude profile of L-CH4 (ppb/day) over the 3 tropical basins for ATom-1234.

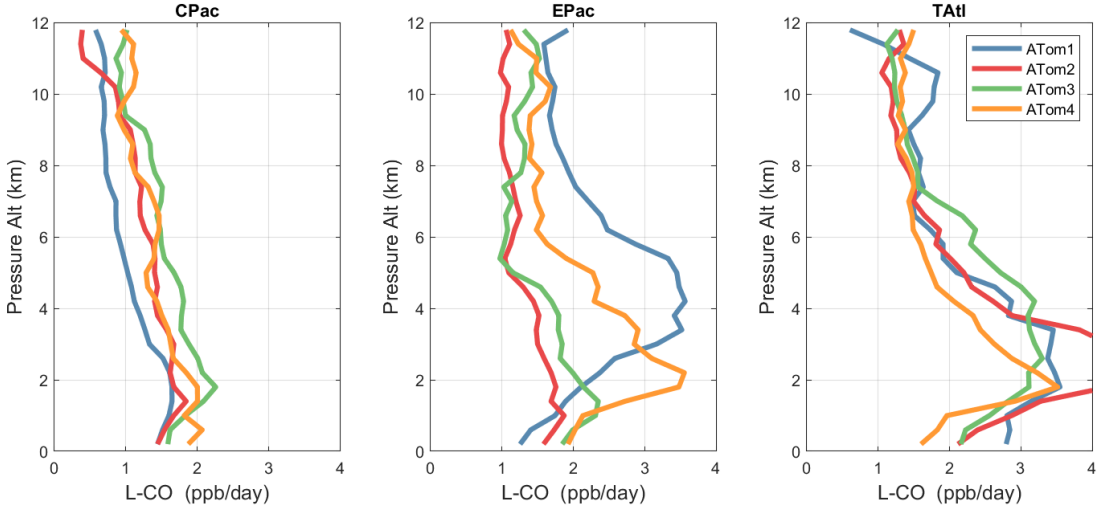

Figure 36. Mean altitude profile of L-CO (ppb/day) over the 3 tropical basins for ATom-1234.

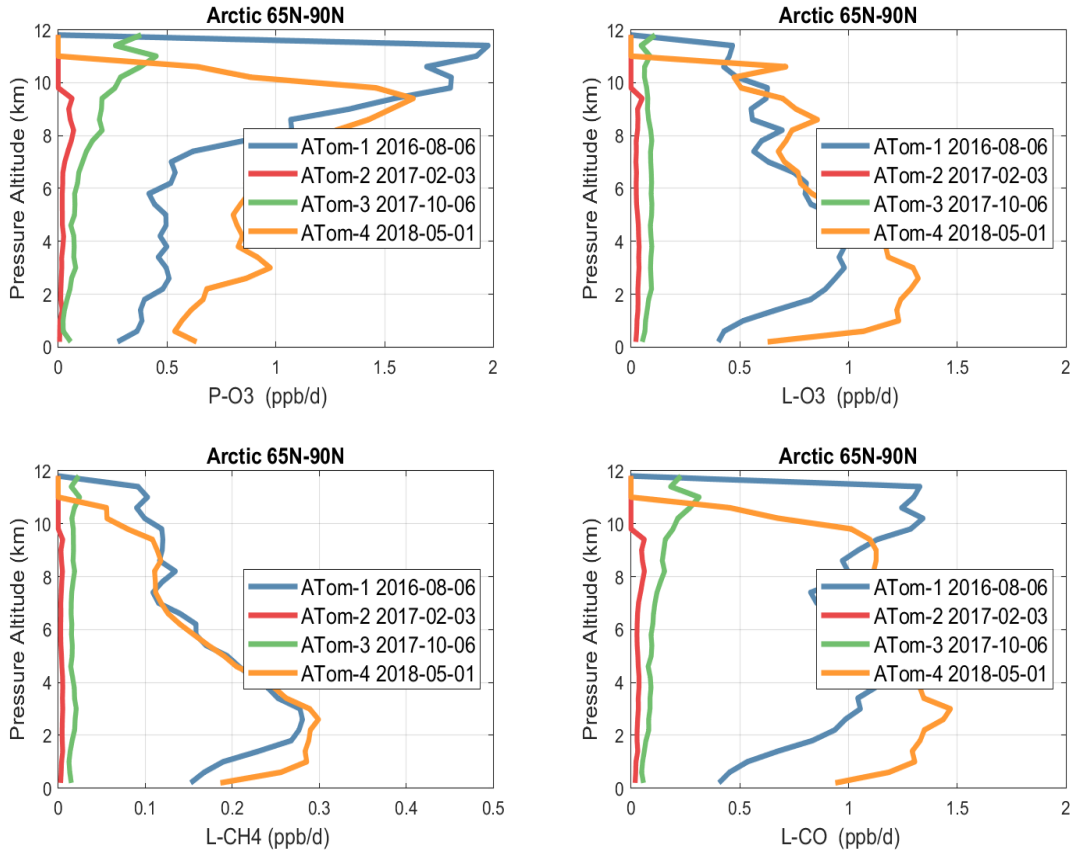

Figure 37. Mean altitude profile of the 4 reactivities (P-O3, L-O3, L-CH4, L-CO, ppb/day) over the Arctic (66°N-90°N) for ATom-1234. All ATom 10s parcels are weighted by frequency of pressure sampling only. Troposphere-only parcels. Dates in the legend are the day of crossing the equator in the Pacific for each deployment

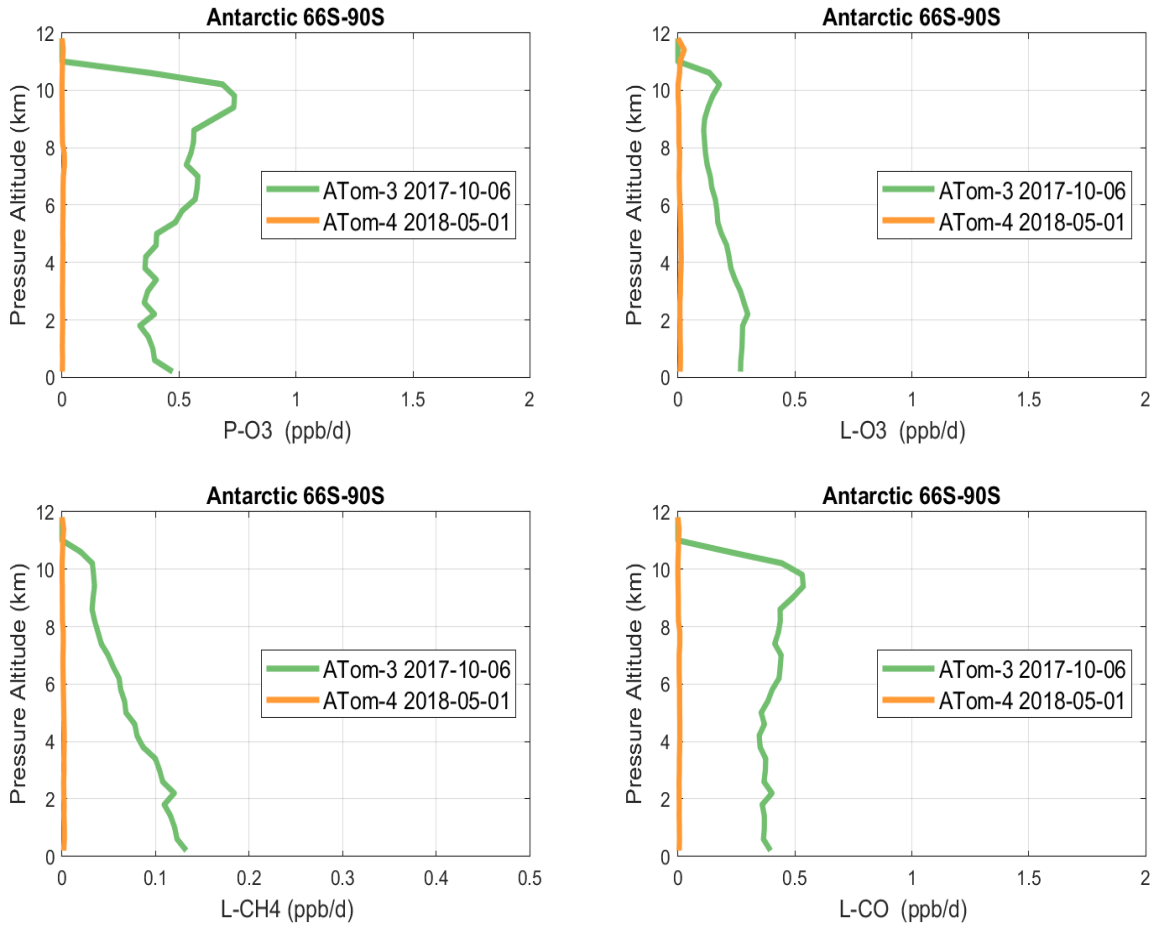

Figure 38. Mean altitude profile of the 4 reactivities (P-O3, L-O3, L-CH4, L-CO, ppb/day) over Antarctica on ATom-34. All ATom 10s parcels are weighted by frequency of pressure sampling only. Troposphere-only parcels. See Fig. 37.

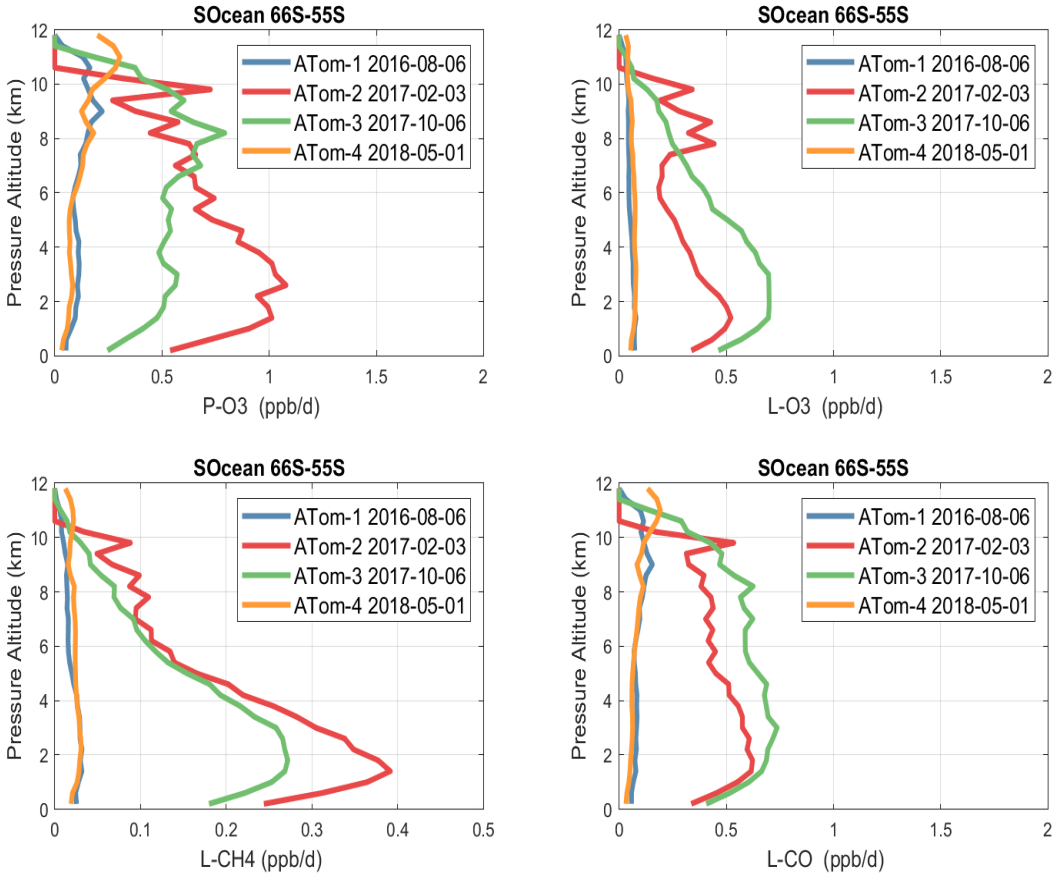

Figure 39. Mean altitude profile of the 4 reactivities (P-O3, L-O3, L-CH4, L-CO, ppb/day) over the Southern Ocean (66°S-55°S) on ATom-1234. All ATom 10s parcels are weighted by frequency of pressure sampling only. Troposphere-only parcels. See Fig. 34.

3.4 Probability densities of photochemical reactivities

The probability densities (PDs) of the ATom reactivities have proven useful in testing model climatologies (see G2023) and are shown for the Pacific and Atlantic basins and the four reactivities in Fig. 40-43. All four deployments are shown in each panel. The relatively low P-O3 PD stands out for both Pacific and Atlantic. The L-CH4 PD peaks at the lowest value with a secondary peak above 1 ppb/d. The very low values of L-CH4 simply reflect the sampling of the upper troposphere where the OH+CH4 rate coefficient proportional to exp(-1775/T) is very small. Thus, the L-CO PD, which is also proportional to OH peaks at higher values. Restricting our PDs to the three tropical regions (Fig. 44-47), we find some distinct deployments (e.g., low P-O3 in C. Pacific for ATom-1; high P-O3 in T. Atlantic for ATom-3; high L-CH4 in E. Pacific for ATom-1), but for the most part the reactivity PDs present similar patterns for each reactivity in each tropical basin. Thus, the ATom PDs provide a useful climatology for model comparisons.

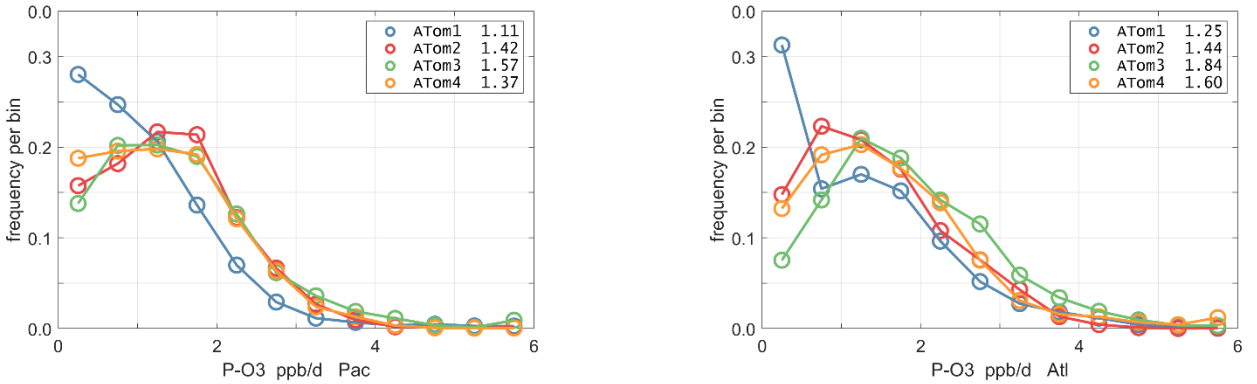

Figure 40. Probability Density of P-O3 (ppb/day) in Pacific and Atlantic basins (53°S-60°N) for ATom-1234. Values in the legend are the basin-wide weighted averages for each deployment. The frequency of parcels with reactivities greater than the maximum shown are added to the last point.

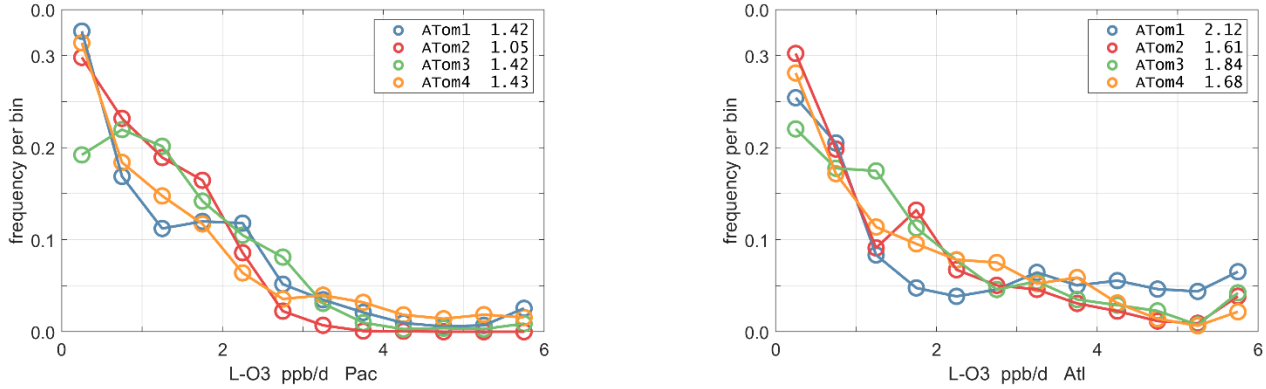

Figure 41. Probability Density of L-O3 (ppb/day) in Pacific and Atlantic basins for ATom-1234. See Fig. 40

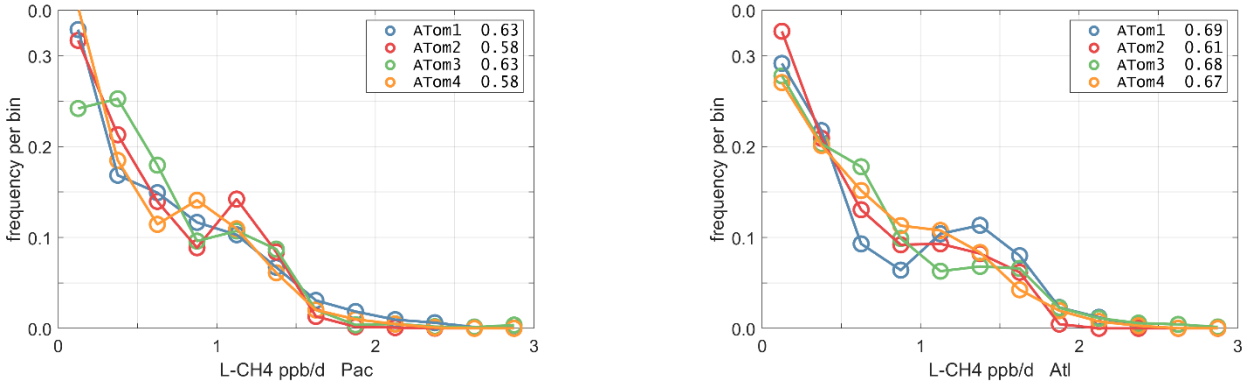

Figure 42. Probability Density of L-CH4 (ppb/day) in Pacific and Atlantic basins for ATom-1234. See Fig. 40.

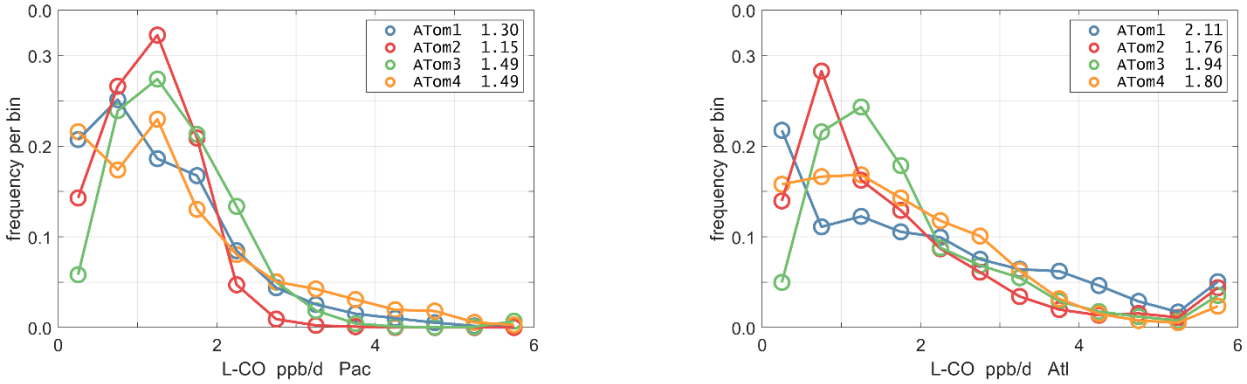

Figure 43. Probability Density of L-CO (ppb/day) in Pacific and Atlantic basins for ATom-1234. See Fig. 40.

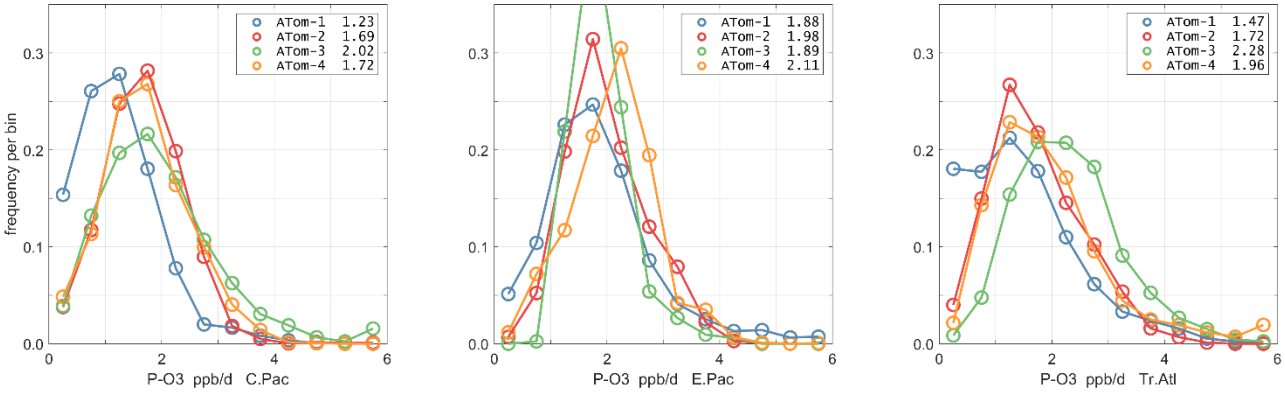

Figure 44. Probability Density of P-O3 (ppb/day) in the 3 tropical basins (30°S-30°N) for ATom-1234. See Fig. 40.

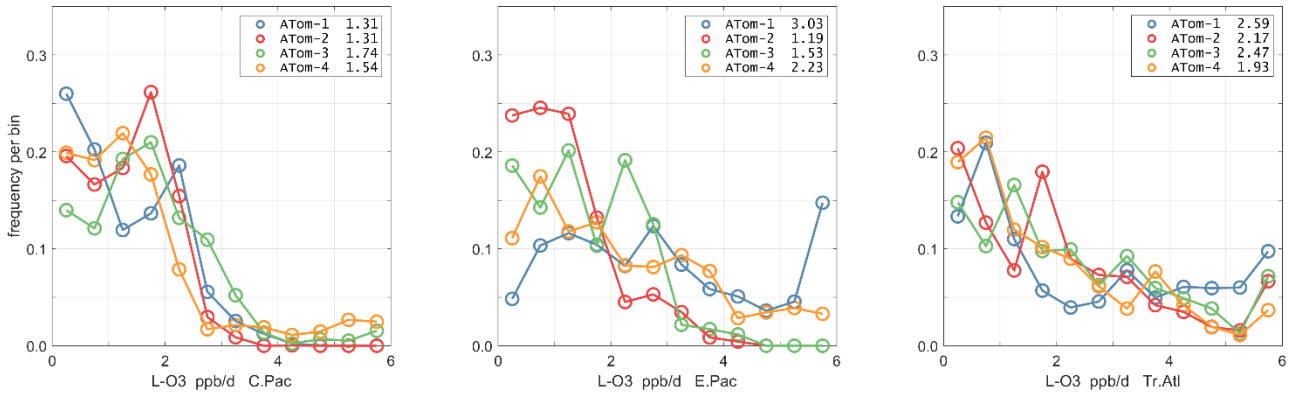

505 **Figure 45**. Probability Density of L-O3 (ppb/day) in the 3 tropical basins for ATom-1234. See Fig. 40.

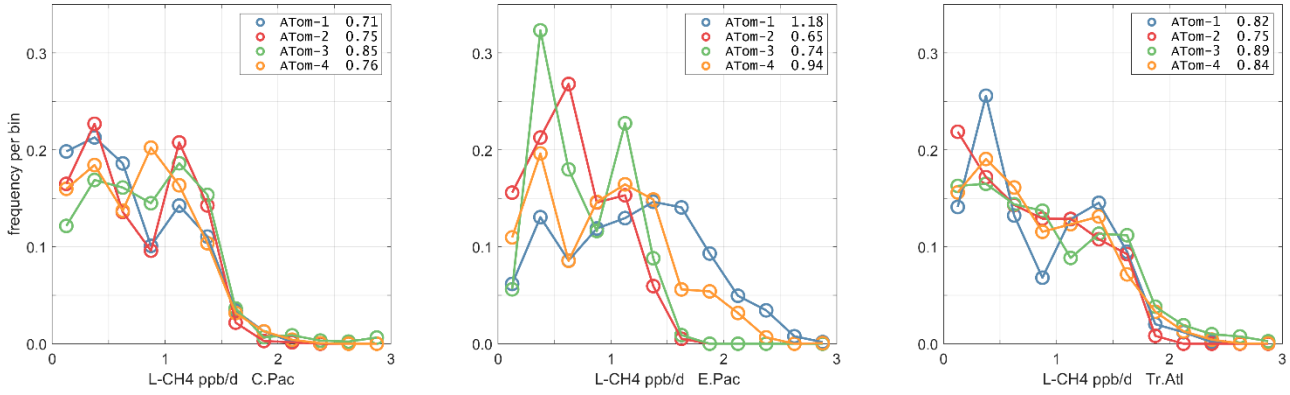

Figure 46. Probability Density of L-CH4 (ppb/day) in the 3 tropical basins for ATom-1234. See Fig. 40.

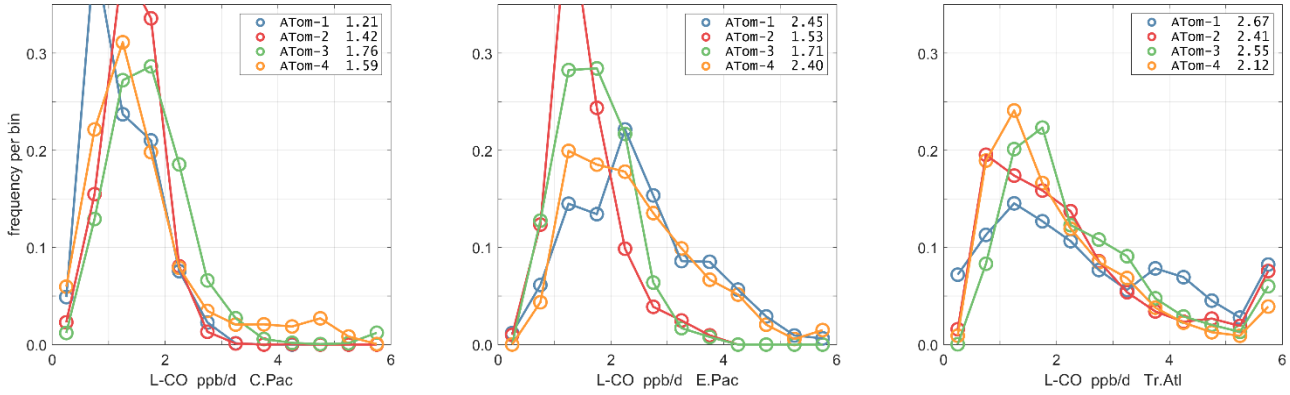

Figure 47. Probability Density of L-CO (ppb/day) in the 3 tropical basins for ATom-1234. See Fig. 40.

4 Chemical sensitivity analysis

4.1 First-order sensitivities

To identify the critical species controlling the tropospheric budgets of O_3 and CH_4, we calculate the sensitivity of the weighted mean reactivity for the Pacific or Atlantic oceanic flights of ATom-1 (53°S to 60°N) with respect to the species measured by ATom. Sensitivity analyses are often calculated with CCMs to assess the factors controlling trends and variability in CH_4 lifetime (Holmes et al., 2013). With CCMs, the calculation includes emissions, scavenging, transport and chemistry, but here using ATom observations we are limited to a 24-hour snapshot with only chemical evolution of the parcels. We believe this limitation does not affect our goal of estimating the errors in the modeled budgets caused by errors in the modeled values of the critical species.

The sensitivity S of reactivity R to species X is calculated from the fractional change in R per fractional change in X (dimensionless, e.g., % per %). We use $\Delta = 10\%$.

$$S \equiv d\{\ln(R)\} / d\{\ln(X)\} = \ln(R[X(1+\Delta)] / R[X]) / \ln(1+\Delta) \quad (1)$$

Results from 20 variables (19 chemical species plus T) for the four reactivities over the Pacific and Atlantic basins for ATom-1 are given in Table 2. The mean sensitivities are calculated using basin-wide averages and have only been calculated using one day's cloud fields (day 223), instead of the 5 days of different cloud fields (e.g., days 213, 218, 223, 228, 233) used for the reactivities in Section 3. Basin-mean differences between two separated days (day 213 and 223) due to cloud fields and ozone column are evaluated and found to be small: <1 % of the value of S, or smaller than 0.002 in absolute. Thus evaluating S with one day is adequate.

Individual parcels show highly variable individual S values, see examples in Fig. 48. The scatter is particularly large because we have included all ATom-1 parcels, including continental data and very low sun angles. For comparison, the basin-mean values (large blue and red dots) are also plotted. Differences across basins and deployments are modest (not shown) and the Pacific-Atlantic comparison for ATom-1 covers this range, remembering that ATom-1 Pacific has unusually low P-O3 values. Surprisingly, the initial value of many species has negligible or small impact on the reactivities. Species like alkanes and alkenes are unimportant because their average abundances are low over the oceans; and species like HCHO and HNO_4, because their abundances are reset by the chemistry during the 24-hour integration.

The lessons from Table 2 are quite interesting. (i) T, H_2O (Q) and O_3 are absolutely critical for all the chemical budgets; (ii) NOx is critical for P-O3, but less so for L-CH4 and L-CO, and even less so for L-O3; (iii) CO as expected controls OH and L-CH4; (iv) CH_4 is like CO, but plays a bigger role in P-O3 through HOx production via HCHO; (v) HOOH plays a modest role (S ~ 0.06) in OH and thus L-CH4 and L-CO; (vi) CH_3OOH plays a surprisingly large role in P-O3 because of the additional HOx release through HCHO; yet (vii) the initial HCHO plays a small role in P-O3 because it is reset quickly by the chemistry in response to the other species listed here. PAN and HNO_3 contribute noticeably to P-O3 through their slow decomposition to NOx. Acetaldehyde (CH_3CHO) stands out in reducing P-O3, L-CH4, and L-CO, presumably from NOx to PAN conversion, with S ranging from -0.05 to -0.09.

One of the most interesting features of Table 2 is the impact of O_3 on it net P-O3 minus L-O3. With O_3 increases, the sum of reactions going into L-O3 increases almost linearly, while the P-O3 reactions decrease. Thus, the net sum decreases faster than linearly. The implications of this for the lifetime of O_3 perturbations is discussed with chemical feedbacks in Section 6.

Table 2. Sensitivities (S = dln[R]/dln[X], dimensionless) for ATom-1

	Pacific				Atlantic			
dln	P-O3	L-O3	L-CH4	L-CO	P-O3	L-O3	L-CH4	L-CO
/dlnT(/10)	**0.715**	**0.292**	**0.753**	**0.775**	**0.628**	**0.279**	**0.751**	**0.771**
/dlnQ	**0.072**	**0.612**	**0.473**	**0.440**	**0.084**	**0.590**	**0.498**	**0.476**
/dlnO3	**-0.304**	**0.978**	**0.442**	**0.390**	**-0.407**	**1.007**	**0.483**	**0.444**
/dlnNOx	**0.734**	**0.055**	**0.188**	**0.209**	**0.724**	0.044	**0.156**	**0.172**
/dlnCO	0.017	0.009	**-0.337**	**0.637**	**0.060**	0.016	**-0.403**	**0.571**
/dlnCH4	**0.184**	-0.031	**0.764**	**-0.209**	**0.196**	-0.038	**0.799**	**-0.176**
/dlnHOOH	0.028	0.029	**0.066**	**0.072**	0.037	0.032	**0.062**	**0.063**
/dlnMeOOH	**0.085**	0.016	-0.047	-0.034	**0.076**	0.010	-0.041	-0.033
/dlnEtOOH	-0.006	-0.001	-0.008	-0.007	-0.008	-0.001	-0.007	-0.006
/dlnHCHO	0.019	0.013	-0.001	0.004	0.034	0.017	0.005	0.008
/dlnPAN	**0.066**	0.006	0.014	0.017	**0.062**	0.005	0.013	0.013
/dlnHNO3	**0.083**	0.008	0.019	0.019	**0.109**	0.008	0.021	0.024
/dlnHNO4	0.029	0.001	0.004	0.012	0.038	0.001	0.005	0.011
/dlnC2H6	0.000	-0.001	-0.003	-0.003	0.000	-0.001	-0.004	-0.004
/dlnAlkane	0.000	0.000	-0.001	-0.001	0.000	0.000	-0.001	-0.001
/dlnAlkene	0.000	0.000	0.000	0.000	-0.001	0.000	-0.001	-0.001
/dlnIsoprn	0.000	0.000	0.000	0.000	0.000	0.000	0.000	0.000
/dlnAcetone	-0.019	0.000	-0.009	-0.009	-0.026	-0.001	-0.011	-0.009
/dlnAcetAld	**-0.055**	-0.007	**-0.053**	-0.048	**-0.086**	-0.010	-0.045	-0.041
/dlnMeNO3	0.007	0.001	0.002	0.001	0.004	0.000	0.001	0.001

Table Notes: Sensitivities are calculated as S = dln[R]/dln[X], in % per % with a 10% perturbation being applied to all 10 s parcels. Q is H_2O and was perturbed 10% like all the chemical species. T is an exception with a 1% perturbation being used, and thus dln[R]/dln[T] should be multiplied by 10 to get % per %. Sensitivities that would round to |S| > 0.1, are shown in bold. The average sensitivity over the basin is calculated here from (a) the single basin-wide average of R. Alternative but less desirable methods would average the individual parcel S values weighted by (b) frequency-of-occurrence and the R value or (c) just frequency of occurrence. Methods (a) and (b) are very close but not identical; while method (c) is clearly different. For any of the large S values (|S| >. 0.1), the difference between (a) and (b) are <1 %, except for dln[P-O3]/dln[T]. As an example the (a)/(b)/(c) values in the Pacific are 0.715 / 0.694 / 0.811 for dln[P-O3]/dln[T](/10); 0.764 / 0.764 / 0.796 for dln[L-CH4]/dln[CH4]; and -0.304 / -0.305 / -0.311 for dln[P-O3]/dln[O3].

560

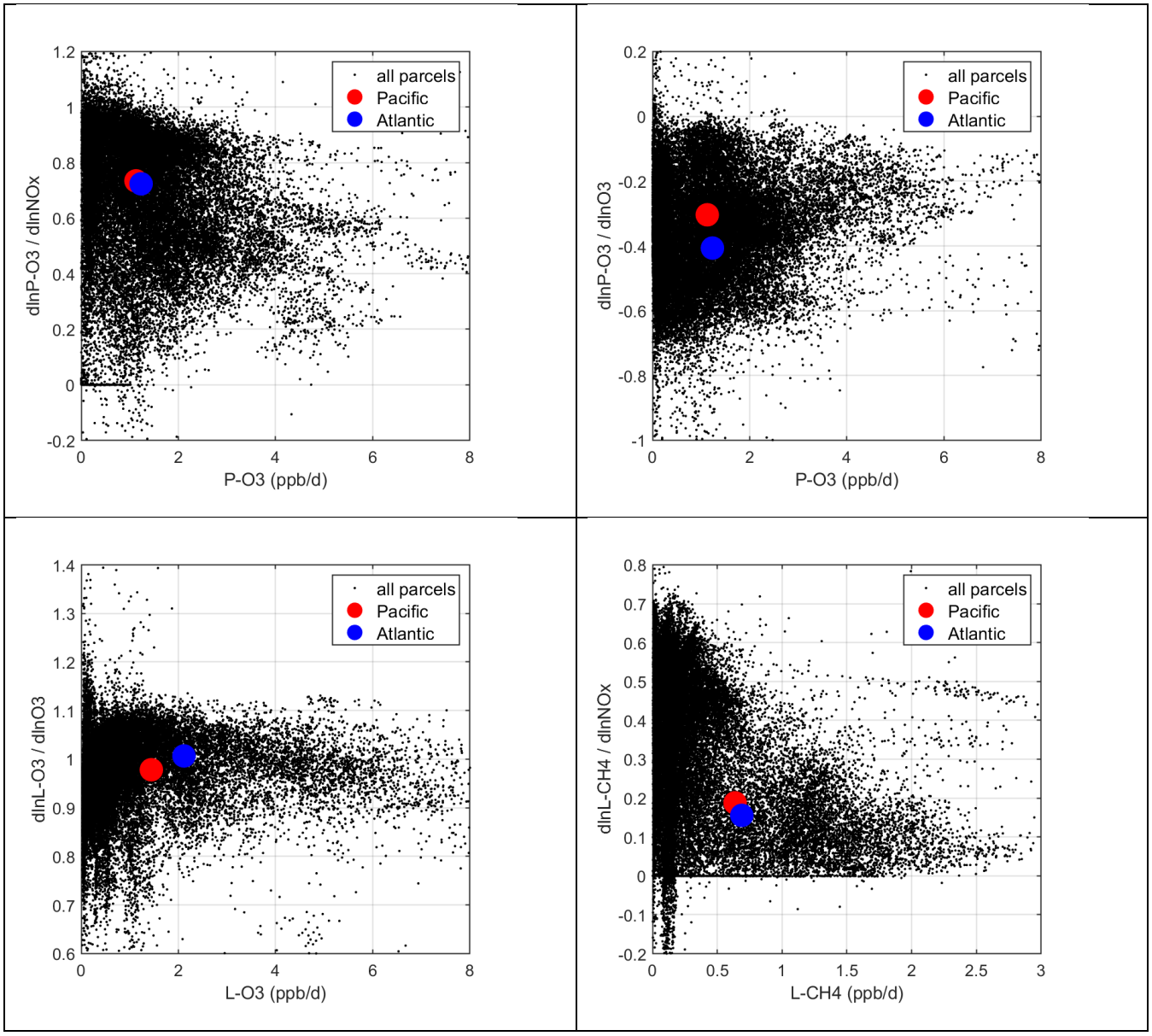

Figure 48. Sensitivity (% per %) plotted against reactivity (ppb/d) for ATom-1: (a) dln[P-O3]/dln[NOx], (b) dln[P-O3]/dln[O_3], (c) dln[L-O3]/dln[O_3], and (d) dln[L-CH4]/dln[NOx]. All ATom-1 parcels, including continental data, are plotted as small black dots; the basin-mean values for the Pacific, as large red dots; and the Atlantic, as large blue dots.

4.2 Second-order terms

Considering that most chemical reactions are of the form R = k(T) X Y or k(T) X^2, we should evaluate the 2nd-order terms in the Taylor expansion. We first tested the quadratic nature of our S values by re-calculating with Δ = 20%, but the results hardly changed and so we are in a linear regime. The second-order cross-species terms are potentially more interesting. We calculate these from a coupled 10% perturbation of two different variables.

$$S_{XY} \equiv S(X+10\% \ \& \ Y+10\%) - S(X+10\%) - S(Y+10\%) \quad (2)$$

We calculated these cross terms only for X = O_3, NOx, CO, CH_4, Q and T, using ATom-1 only as in Table 2. Table 3 shows the deviations from linearity (S_{XY}) for each of the 15 XY-pair combinations, listing the Pacific basin in the upper triangular part of the matrix, and the Atlantic basin in the lower triangular part. The diagonals simply give the mean first-order S_X values for Pacific plus Atlantic. These off-diagonal S_{XY} terms are clearly second-order in importance for the chemistry: e.g., the importance of the S_{XY} term in d^2ln(L-CO) / dln(O3) dln(Q) for the Pacific is given as +0.017, which is a small fraction of the 1st order terms of +0.42 for dln(L-CO) / dln(O3) and +0.46 for dln(L-CO) / dln(Q). The near symmetry of the four matrices in Table 3 indicate that average S_{XY} sensitivities are similar for both basins. Hence we find no evidence that coupled perturbations must be considered when modelers explore the factors driving changes in the lifetime of CH_4 (e.g., Holmes et al., 2013).

Although we have long known that H_2O and T are important factors (e.g., Table 2 of Holmes et al., 2013), these quantities have often been relegated to the physical climate system and not often thought of a major source of model error in the chemical system. Thus, when we are diagnosing the future tropospheric O_3 or CH_4 from the multi-model comparisons (Stevenson et al., 2013; Voulgarakis et al., 2013; Young et al., 2018; Griffiths et al., 2021), we need to document biases in T and H_2O. For example, from Thornhill et al., (2021a) we estimate an increase in CH_4 loss frequency of about 4.5 %/K for the two consistent models. (The two other models in the Thornhill study each seem aberrant in their own way.) From Table 4, a +1 K change increases L-CH4 by 2.5%, and the Clausius-Clapeyron inferred 7% increase in Q adds 3.4% for a total of 5.9 %/K, a reasonable first-order result considering that other climate driven changes, such as O_3, are not included. For model evaluation, comparing T with mean profiles is straightforward, but H_2O is more difficult, even with profiles, because of the three orders of magnitude change over the troposphere. Thus, we recommend that relative humidity over liquid water (RHw, %) be used to detect bias. See statistics on critical species and RHw in the next section.

Table 3. Second-order cross-term sensitivities S_{XY} calculated as S(+dX+dY) – S(+dX) – S(+dY) for Pacific (upper triangular) and Atlantic (lower triangular) basins in ATom-1

P-O3	dO3	dNOx	dCO	dCH4	dQ	dT
dO3	***-0.36***	0.000	-0.001	0.004	0.004	0.003
dNOx	-0.005	***0.73***	0.004	0.001	-0.003	-0.016
dCO	-0.005	0.003	***0.04***	-0.005	0.000	0.002
dCH4	0.003	-0.001	-0.014	***0.19***	0.002	0.002
dQ	0.002	-0.006	-0.002	-0.005	***0.08***	0.004
dT	0.001	-0.023	-0.001	0.003	0.000	***0.67***
L-O3	dO3	dNOx	dCO	dCH4	dQ	dT
dO3	***0.99***	-0.004	0.001	-0.003	0.000	-0.002
dNOx	-0.003	***0.05***	-0.001	0.001	-0.002	0.002
dCO	0.001	-0.001	***0.01***	0.001	-0.001	0.000
dCH4	-0.003	0.001	0.000	***-0.03***	0.001	-0.001
dQ	0.000	-0.002	-0.002	0.001	***0.60***	-0.004
dT	-0.001	0.001	0.001	-0.001	-0.003	***0.29***
L-CH4	dO3	dNOx	dCO	dCH4	dQ	dT
dO3	***0.46***	-0.014	0.003	-0.002	0.016	-0.009
dNOx	-0.015	***0.17***	0.001	0.001	-0.008	0.003
dCO	0.002	0.001	***-0.37***	0.008	0.000	0.011
dCH4	-0.003	0.001	0.007	***0.78***	-0.002	-0.010
dQ	0.014	-0.008	-0.001	-0.003	***0.49***	-0.005
dT	-0.008	0.000	0.011	-0.008	-0.006	***0.75***
L-CO	dO3	dNOx	dCO	dCH4	dQ	dT
dO3	***0.42***	-0.015	0.004	-0.003	0.017	-0.009
dNOx	-0.016	***0.19***	0.001	0.002	-0.008	0.003
dCO	0.003	0.001	***-0.40***	0.008	0.001	0.011
dCH4	-0.004	0.001	0.006	***0.81***	-0.003	-0.009
dQ	0.015	-0.008	-0.001	-0.003	***0.46***	-0.005
dT	-0.009	0.000	0.011	-0.008	-0.006	***0.77***

Table Notes: T is temperature and was perturbed only 1%; Q is H_2O and was perturbed 10% like all the chemical species. The diagonal elements are the average (Pacific and Atlantic) 1st order sensitivities S(+dX), see Table 2. The upper triangular (Pacific) and lower triangular (Atlantic) matrices show the 2nd order sensitivities S_{XY} = S(+dX+dY) – S(+dX) – S(+dY).

5 Key ATom species and NOx version 3

5.1 NOx version 3 and MDS flags

When completing this paper's analysis of the reactivities (Section 3) and re-examining the problems with NOx (NO_2 + NO) profiling that led to MDS version 2b (described in G2023), we re-examined the NOx long-gap interpolation. There were long stretches of these gaps (flag=4), as well as missing flight data (flag=5), that resulted in critical flight segments being filled with mean profile data. These gaps are caused by the lack of NO_2 rather than NO measurements as shown in Fig. 49 (4 ATom deployments x 2 ocean basins). The number of profiles with NO data but no NO_2 data (red dots) is extensive and covers some key regions (e.g., the lower troposphere in the Atlantic in ATom-2; the E. Pacific in ATom-34). Thus, we developed a secondary measurement of NOx (flag=2) based on the measured value of NO.

We look for a linear relationship between NOx and NO, i.e., $[NOx^{fit}] = A\,[NO]$, and use the Pacific and Atlantic Ocean basins to avoid continental pollution. Adding a multiplier of $[O_3]$ the right-hand side did not improve the fit. The ratio A does not depend noticeably on altitude. A linear fit of A minimizing the errors, NOx^{fit} – NOx, for oceanic NOx values < 250 ppt gives A = 2.055. The unweighted mean value of NOx is 50 ppt; the one-sigma range of errors (16^{th}-84^{th} %) is ±22 ppt; and the rmse is 31 ppt. Figure 50 shows the oceanic NOx^{fit} points (red) as well as all others (blue) plotted against NOx. The new 8400 NOx^{fit} parcels are labeled with flag=2 and eliminate most of the long-gap parcels and all of the missing-flight parcels. The G2023 Table S4 percentage of flags = 0-1-2-3-4-5 for NOx changes from 0.8 - 80.8 - 0.0 - 8.3 - 7.6 - 2. 5% to 0.8 - 80.8 - 5.7 - 8.7 - 4.0 - 0.0 %. This new NOx^{fit} is named 'NOxadd' in version 3 of the MDS (ATom_MDS3.nc). In this paper the figures with the new version 3 NOx^{fit} is labeled NOxx.

Caution should be taken when using the MDS data for observational statistics because of the gap filling needed to calculate the RDS. MDS data flagged with a 1 or 2 are reliable because they are based on primary or secondary instrument observations. Short-gap interpolation (flag =3) has been tested (G2023) and found to be reasonably accurate. Further, adding a short-gap, linearly interpolated flight segment (< 1 km in altitude) will have little effect on species statistics here because of the parcel weighting that is used to achieve equal sampling with altitude and latitude. Flags 4-5-6 are more worrisome as these long-gap or missing-flight methods cannot be evaluated for accuracy. In MDS v3, the chemical species with >10 % of parcels with flags 4-5-6 are HNO_4, CH_3OOH, C_2H_6, alkanes, C_2H_4, alkenes, C_2H_2, all alkyl nitrates, and SF_6. Fortunately, the only one of these species that has a significant impact on the RDS ($|S| \sim 0.1$) is CH_3OOH.

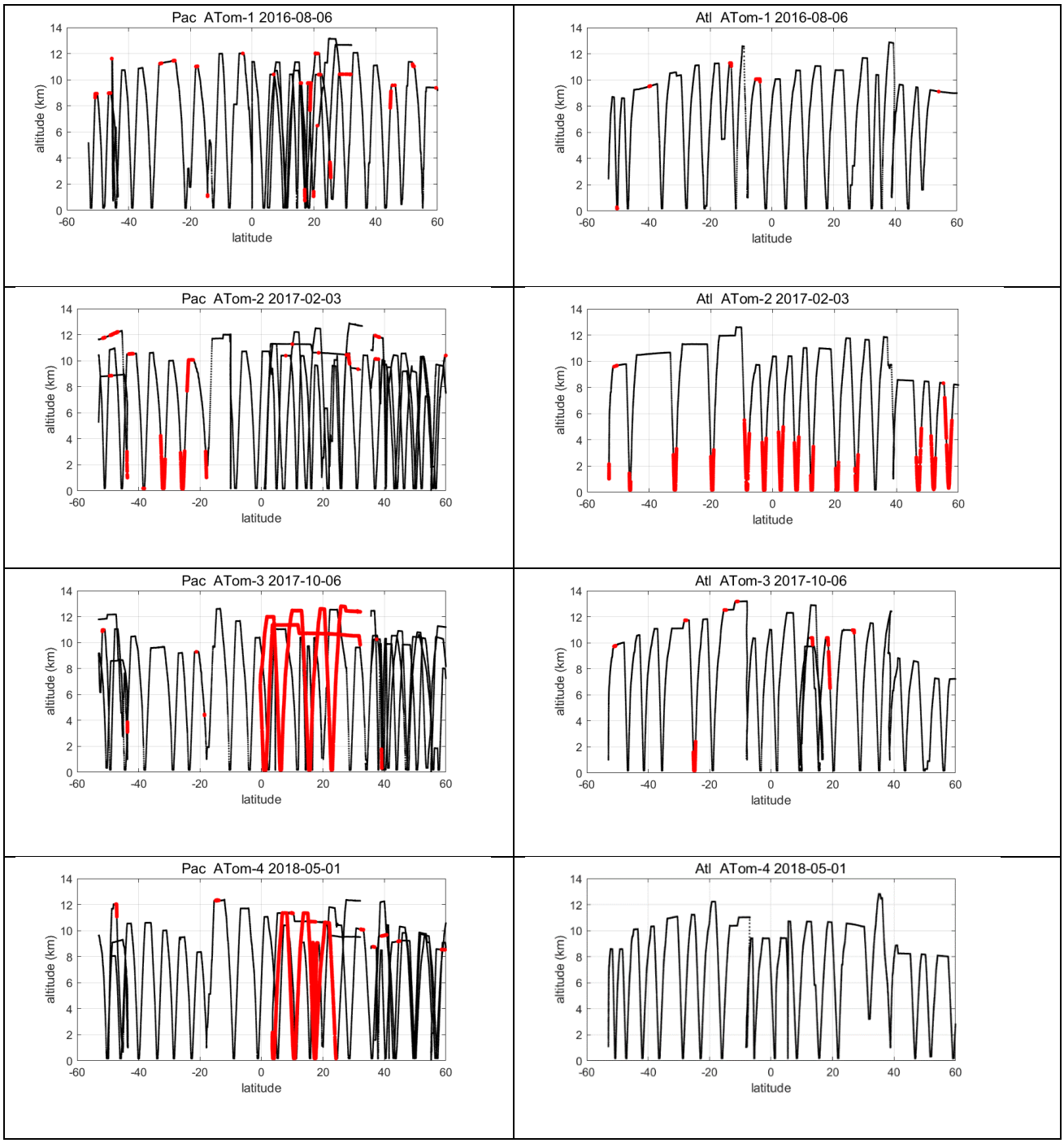

Figure 49. ATom-1234 profiling in Pacific and Atlantic basins showing parcels (large red dots) where NO_2 observations are missing, where long-gap interpolation was used in MDS version 2b, and where shifting to NOx^{fit} based on NO observations in MDS version 3 results in a change in NOx of >1 ppt.

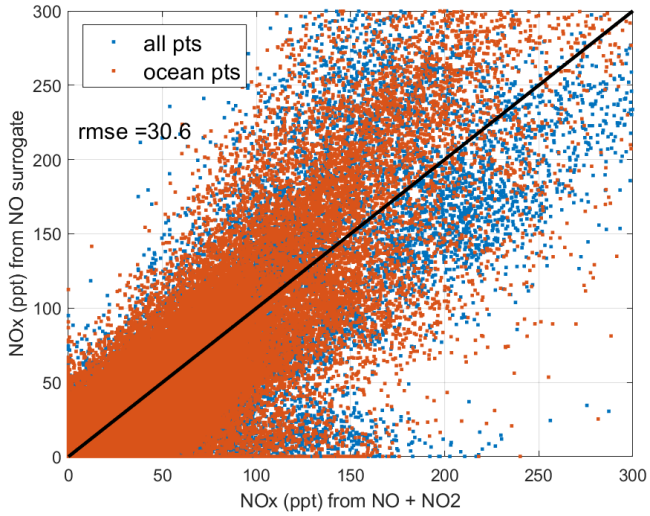

Figure 50. Scatter plot of NOx using NO as a surrogate (NOx = 2.055 x NO, y-axis) and directly measured NOx (x-axis) for all ATom parcels where NO_2 is measured. The red points are all ocean basin parcels; and the blue points are all others. The 1:1 black line is for reference.

5.2 Updated version 3 reactivities

We did not have the resources to repeat all the calculations (5-day averages, sensitivities) with version 3 NOx, and so choose to redo all reactivity calculations with just the first day in each deployment (i.e., days 32, 121, 213, and 274). Comparisons of reactivities must then be done with the same single-day calculation with version 2b. Given the range in reactivities for ATom-1 Pacific and Atlantic, we also did not redo the sensitivities for MDS-3. Table 4 provides a summary of the changes in Pacific and Atlantic basin-mean and -median reactivities for ATom-1234 calculated using only the first day. Almost all the changes from v2b to v3 are negative. P-O3 has, as expected, the largest changes for ATom-3 Pacific and ATom-2 Atlantic. Here the median decrease (-13% and -16%, respectively) is twice as large as the mean, implying a large shift in the mid-level values of P-O3. The remaining changes in the mean reactivities are small, 0 to -3 %.

Vertical profiles of the four mean reactivities are shown in Figures 51-54, with separate panels for Pacific and Atlantic basins and ATom-1234 shown in each panel. The solid colored lines are calculated for one day with v3 NOx^{fit}; and the dashed colored lines, for v2b NOx. For P-O3, the difference is visible at different altitudes for ATom-234, but the profile shape is clearly changed for ATom-3 Pacific 10-12 km and ATom-2 Atlantic 0-2 km. Remembering that only NOx changes here with v3 and that P-O3 has highest sensitivity to NOx, we expect the other reactivities (L-O3, L-CH4, L-CO) to change little. That is the case except for L-CH4 and L-CO for ATom-2 Atlantic 0-2 km.

The probability densities (PDs) for the reactivities in each ocean base are shown in the 8 panels of Figure 55. The weighted mean reactivities (ppb/d) in each basin are given for ATom-1234 in the figure legend with the v2b value followed by the v3 value. The PDs and mean values here are for one day only and thus differ slightly from the five-day averages analyzed in Section 3. Similar to the profiles, the PDs show detectable but insignificant changes from v2b to v3 and remain robust (i.e., compare with Fig. 40-43). For the most part, the mean reactivities change by < 0.01 ppb/d, with major exceptions for P-O3

in Pacific ATom-34 and Atlantic ATom-23, where the v3 value is 0.03 to 0.10 ppb/d smaller than the v2b value. The L-CO also shows some decreases with v3 of about 0.03 ppb/d (Pacific ATom-3, Atlantic ATom-2), and in a relative sense (~2%) this might be true for L-CH4, but it is not apparent with the precision shown given that L-CH4 is 2-3 times smaller than L-CO.

Table 4. Reactivity change (%) from MDS v2b to v3

	ATom1	ATom2	ATom3	ATom4	ATom1	ATom2	ATom3	ATom4
	Pacific mean				Pacific median			
P-O3	-1%	-1%	-6%	-3%	0%	-2%	-13%	-4%
L-O3	0%	0%	-1%	0%	0%	0%	-1%	0%
L-CH4	0%	0%	-2%	-2%	0%	2%	0%	0%
L-CO	0%	0%	-3%	-1%	0%	-2%	-4%	-1%
	Atlantic mean				Atlantic median			
P-O3	-1%	-8%	-2%	0%	0%	-16%	-2%	0%
L-O3	0%	-1%	-1%	0%	0%	-3%	0%	0%
L-CH4	0%	-2%	-1%	0%	0%	0%	0%	0%
L-CO	0%	-2%	-1%	0%	0%	-3%	-1%	0%

Table notes: Unweighted mean of all parcels. Calculated for day 1 only, not averaged over 5 separate days.

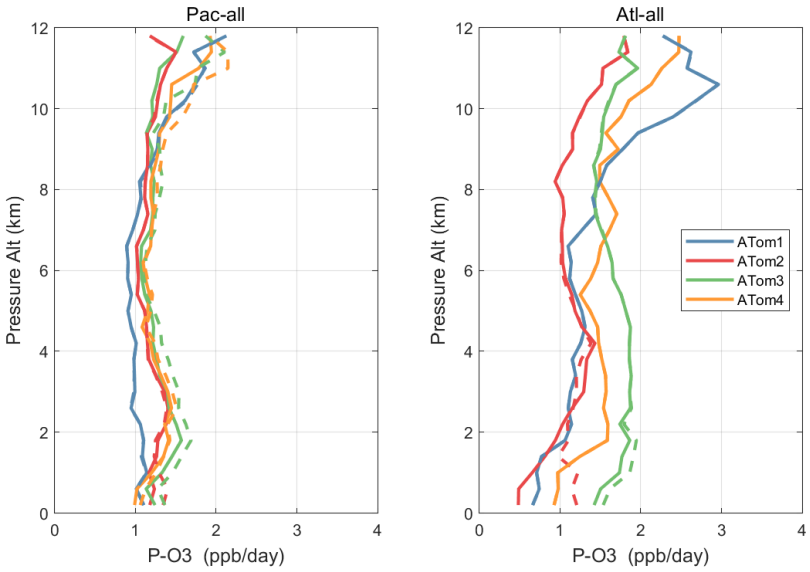

Figure 51. Altitude profiles of mean P-O3 (ppb/d) over Pacific and Atlantic basin for ATom-1234. Results are for one day only in each deployment (days 32, 121, 213, 274). Compare with Fig. 29. The solid lines are for version 3 NOx and the dashed for version 2b.

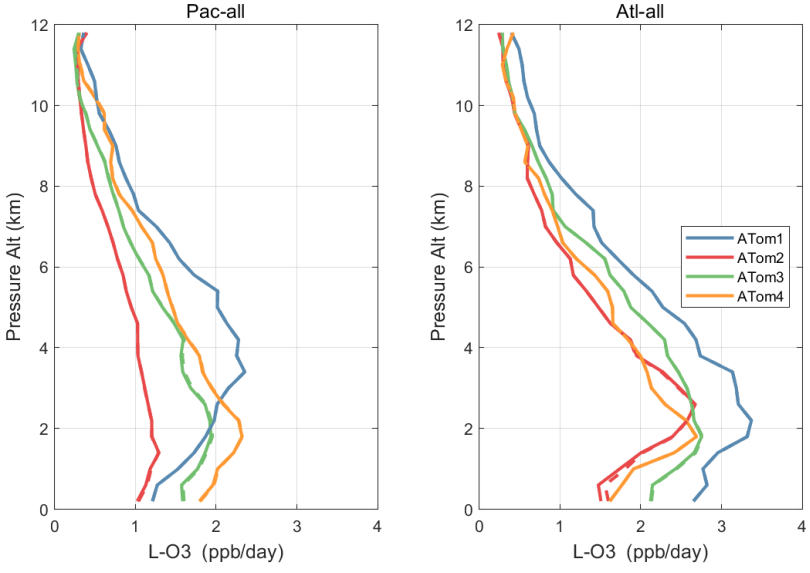

Figure 52. Altitude profiles of mean L-O3 (ppb/d) over Pacific and Atlantic basin for ATom-1234. See Fig. 51. Compare with Fig. 30. Solid lines are MDS-3, and dashed lines are MDS-2b.

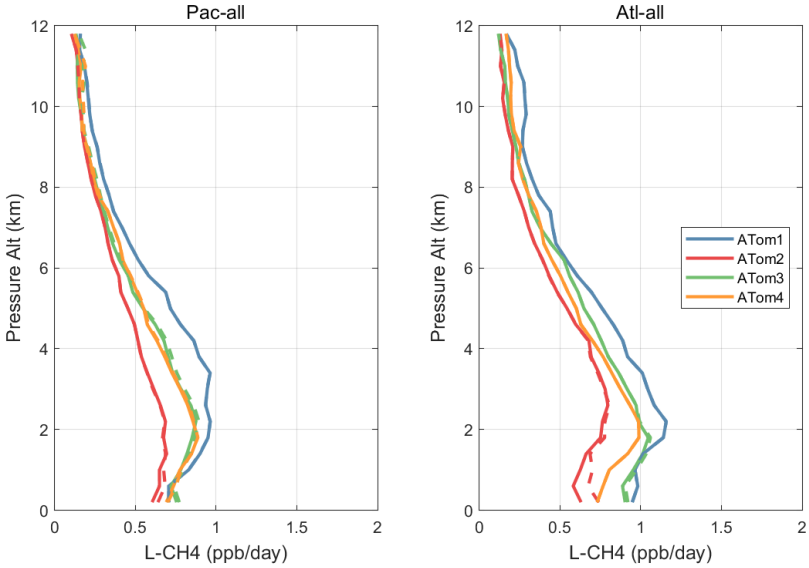

Figure 53. Altitude profiles of mean L-CH4 (ppb/d) over Pacific and Atlantic basin for ATom-1234. See Fig. 51. Compare with Fig. 31. Solid lines are MDS-3, and dashed lines are MDS-2b.

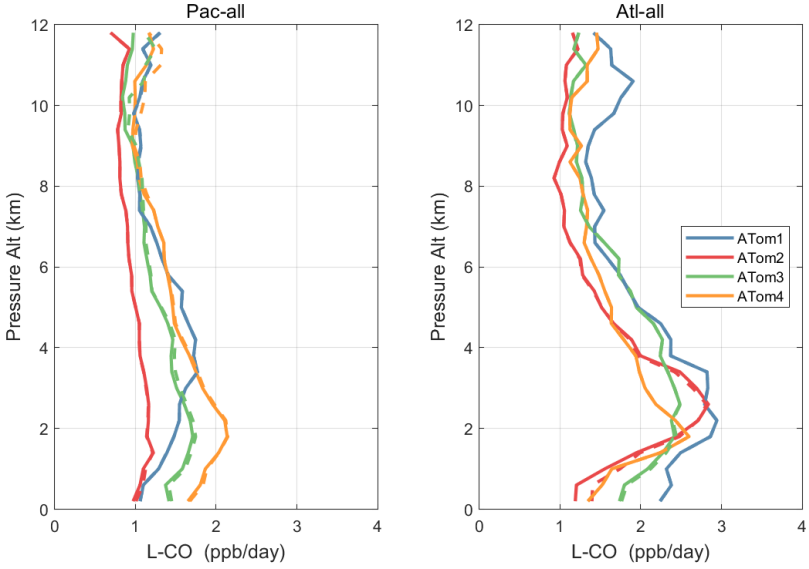

Figure 54. Altitude profiles of mean L-CO (ppb/d) over Pacific and Atlantic basin for ATom-1234. See Fig. 51. Compare with Fig. 32. Solid lines are MDS-3, and dashed lines are MDS-2b.

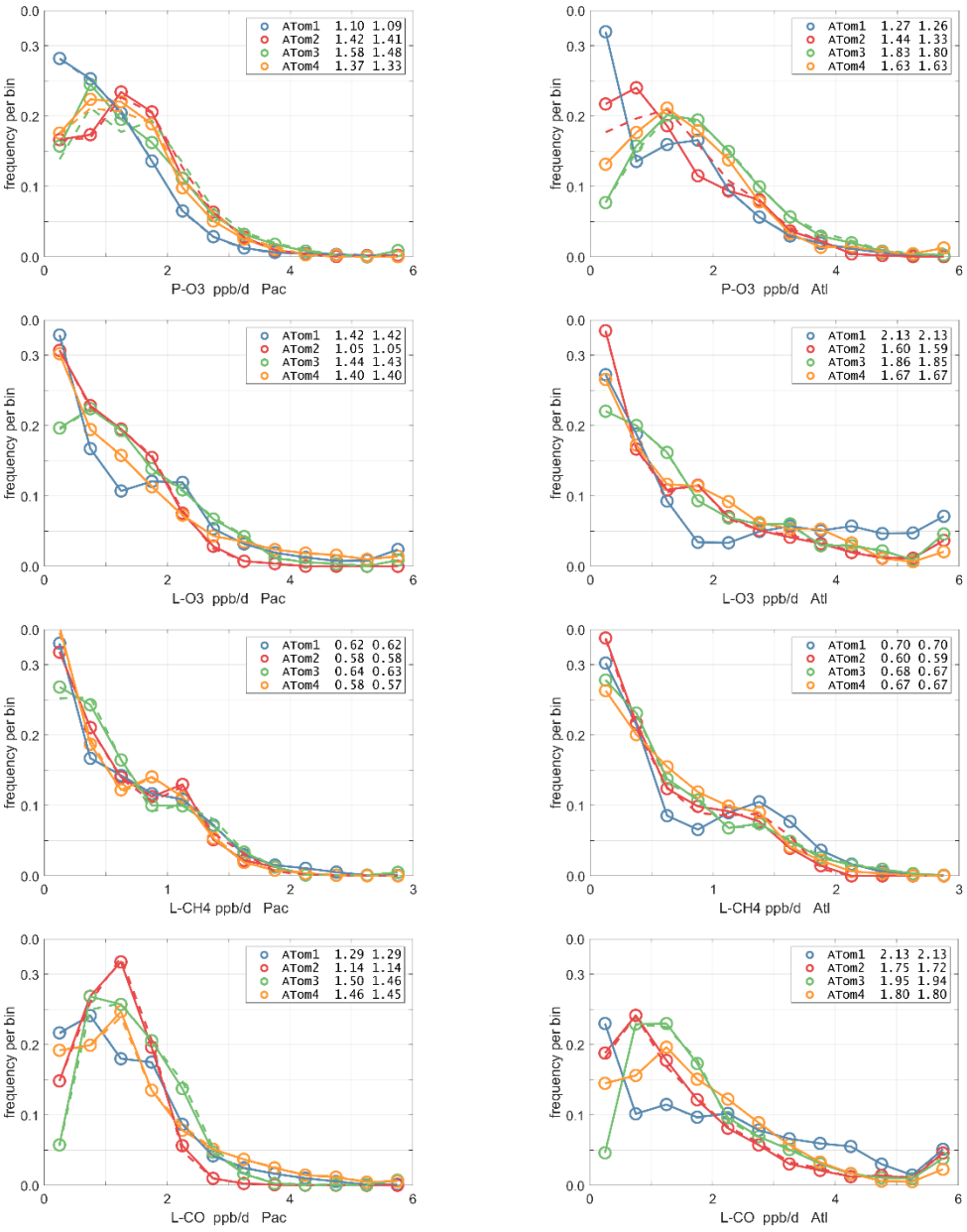

Figure 55. Probability Density of the 4 reactivities (P-O3, L-O3, L-CH4, L-CO, all in ppb/day) in **(left)** Pacific and **(right)** Atlantic basins (53°S-60°N). All 4 ATom deployments are shown in each panel. Only the first day of each deployment is shown (hence these are not identical to Figures 40-43). Values in the legend are the basin-wide averages for each deployment, given as v2b (dashed lines) and then v3 (solid lines). See Figure 40.

720

5.3 Distribution of key ATom species

We examine the distribution of key species over the Pacific and Atlantic ocean basins with mean profiles of NOx (v2b), NOx^{fit} (v3), and HOOH in Fig. 56. In the Pacific, the impact of v3 NOx (labeled NOxx) is to reduce some high values in ATom-34 and make ATom-234 almost identical in the Pacific. ATom-1 NOx remains much smaller than the other
725 deployments. In the Atlantic, the v2b-v3 changes are not obvious, except for reducing the ATom-2 values below 3 km to look more like ATom-1. HOOH profiles often show a peak (500-1000 ppt) in the lower troposphere, 1-5 km, with the Atlantic usually being larger. For Pacific ATom-1, NOx (and P-O3) is particularly low, but HOOH (and L-O3) is particularly high.

Given the importance of the tropics, we replot these profiles of NOx(v2b), NOx^{fit}(v3), and HOOH for the three tropical
730 regions in Fig. 57. The C. Pacific is not much affected by the v2b-v3 update, but the E. Pacific and T. Atlantic noticeably change. For Pacific HOOH, we find the 1-5 km peak is mostly in the E. Pacific, and thus relate high levels of HOOH and related HOx activity with outflow from continents.

The 2D curtain files for the Pacific and Atlantic basins show the level of heterogeneity in NOx for ATom-1234 in Fig. 58-59. These two figures compare NOx(v2b) with NOx(v3) in the Pacific and Atlantic, respectively. The biggest changes v2b
735 to v3 in the Pacific occur for ATom-34 and are due to the E. Pacific flights as noted earlier. In these plots the E. Pacific profiles overlap with the C. Pacific profiles, and so some heterogeneity in this region is caused by longitudinally distant, not-along-flight parcels. Similarly, for ATom-234, the N. Pacific curtain plots here includes two separate flights: one in the E. Pacific from Palmdale to Anchorage and, a few days later, one in the C. Pacific from Anchorage to Kona. Overall, the NOx shows that high values (> 100 ppt) consistently but sporadically occur at the uppermost flight levels. These high-NOx
740 parcels are probably due to lightning from deep convection, predominantly over continents, and they are the cause of high P-O3 values in the 10-12 km region of most ATom flights.

Figure 60 shows HOOH for both basins (8 panels). Unlike NOx, the HOOH patterns show extensive regions, 30° in latitude or wider, mostly tropical, with abundances >1000 ppt between 1 and 6 km. This pattern is expected with a large, somewhat homogeneous chemical source of HOOH that partly follows the sun with each ATom deployments. We often find high-NOx
745 regions are separated from the high-HOOH ones. An unusual block of mid-tropospheric air was sampled in the southern Pacific (30°S-15°S) during ATom-3 (Figure 58). This air mass had uniformly high NOx values (60-100+ ppt), not typical of convective high-altitude NOx. These NOx values were directly measured and not affected by the v2b-v3 shift. The anti-correlation with HOOH (Figure 60) is surprising: high levels of HOOH surround the separate high-NOx air mass. Given the overall importance of high-NOx and (separately) high-HOOH regions to the chemical budgets, it would be valuable to check
750 the CTM/CCM modeling of this feature to understand its cause.

Figures 61-64 show the probability densities (PDs) of CO (ppb), O_3 (ppb), relative humidity over water (RHw, %), and NOx (log(ppt)) for the tropical ocean regions (C. Pacific, E. Pacific, T. Atlantic). The PDs are calculated for lower troposphere (0-6 km) and the full ATom-sampled troposphere (0-12 km). For the first three quantities, the legend for each deployment lists the mean value, standard deviation, and skewness; while for NOx whose PD is uses log([NOx]), the legend lists just the
755 mean value (ppt) and the mean log value (converted back to ppt).

G2023 in their Figure 4 compared the ATom-1 PDs for NOx, HCHO, and HOOH with 6 CTM/CCM climatologies for August, and showed some clearly divergent model results. We believe these ATom PDs provide a valuable model metric

and can be used to track down model errors. Here we compare the ATom-1234 PDs for CO, O_3, RHw, and NOx because these are critical species based on the sensitivities (Table 2). The NOx PDs are paired with v3 versus v2b panels; they show large shifts in the E. Pacific as expected from earlier comparisons. The T. Atlantic NOx PDs also show large shifts with version. Thus, the NOx PDs should be used with caution, although the C. Pacific PDs look similar across the four deployments and should provide a robust statistic on the NOx distributions in the 0-12 km altitude range. For CO, O_3, and RHw, we find that the C. Pacific and T. Atlantic PDs are stable across deployments and should present an excellent observational climatology metric for the models. The E. Pacific PDs vary greatly with deployment and do not represent a stable climatology.

The RHw PDs are quite different from the chemical species. RHw has a bimodal distribution for the tropical regions with a narrow peak probability below 10% RHw and a broad maximum about 80% RHw. Thus, RHw clearly distinguishes between two types of tropical air masses reflecting the Hadley cell: a humid, generally upwelling tropical air mass, and a dry descending sub-tropical air mass. As for other species and reactivities, the E. Pacific RHw is highly variable with deployment, showing that ATom-14 (the more reactive periods) lack dry air with RHw < 20%, consistent with the sensitivity to H_2O and the high reactivities noted above. For convenience in model comparisons, a tabulated version of the CO, O_3, and RHw PDs, giving values for the 5^{th}, 20^{th}, 50^{th}, 80^{th}, and 95^{th} percentiles for each basin and deployment, are provided in Table 5.

The use of two-dimensional PDs for species as a way of comparing models and measurements was investigated previously (P2017, P2018, and Fig. 7 of G2023). We do not pursue examples here, but recommend that these 2D PDs of critical species defined from the sensitivity analyses, including the fitted ellipses, be tested as model metrics.

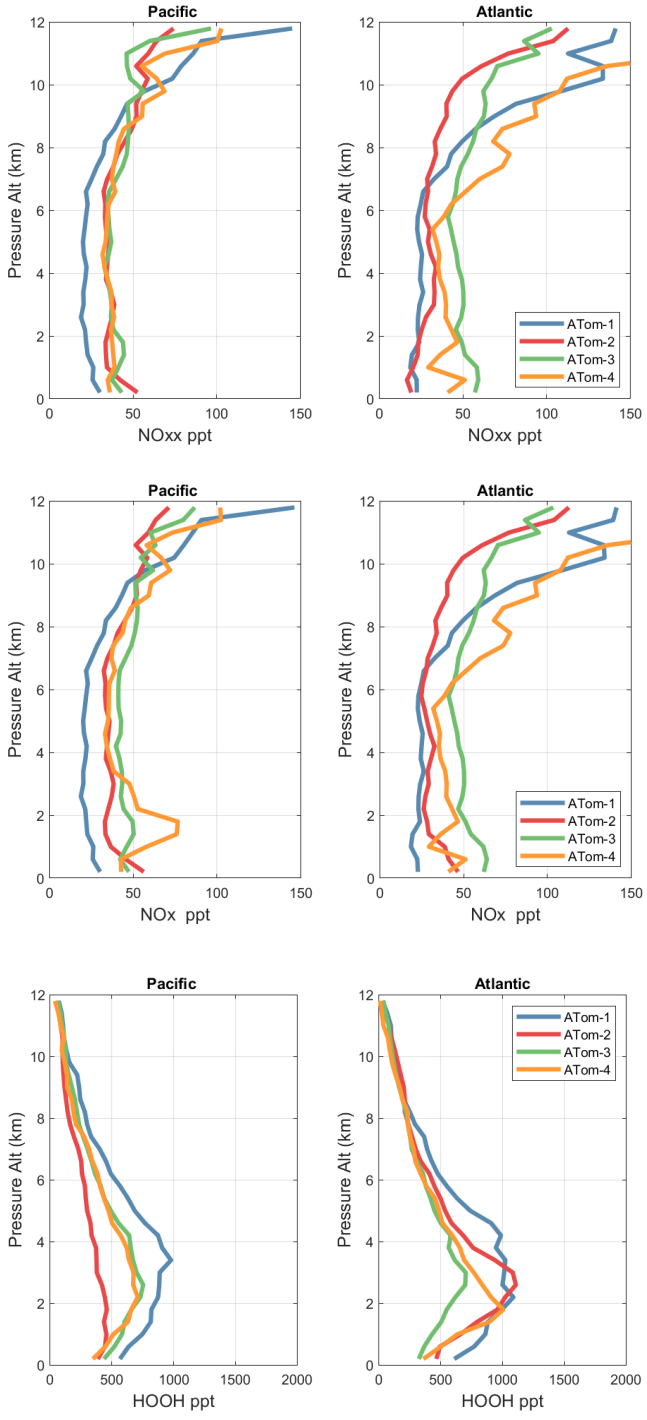

780

Figure 56. Vertical mean profiles (ppt vs pressure altitude) of NOx (v2b), NOxx (=NOx v3) and HOOH over the Pacific and Atlantic basins. Standard weighting, see text.

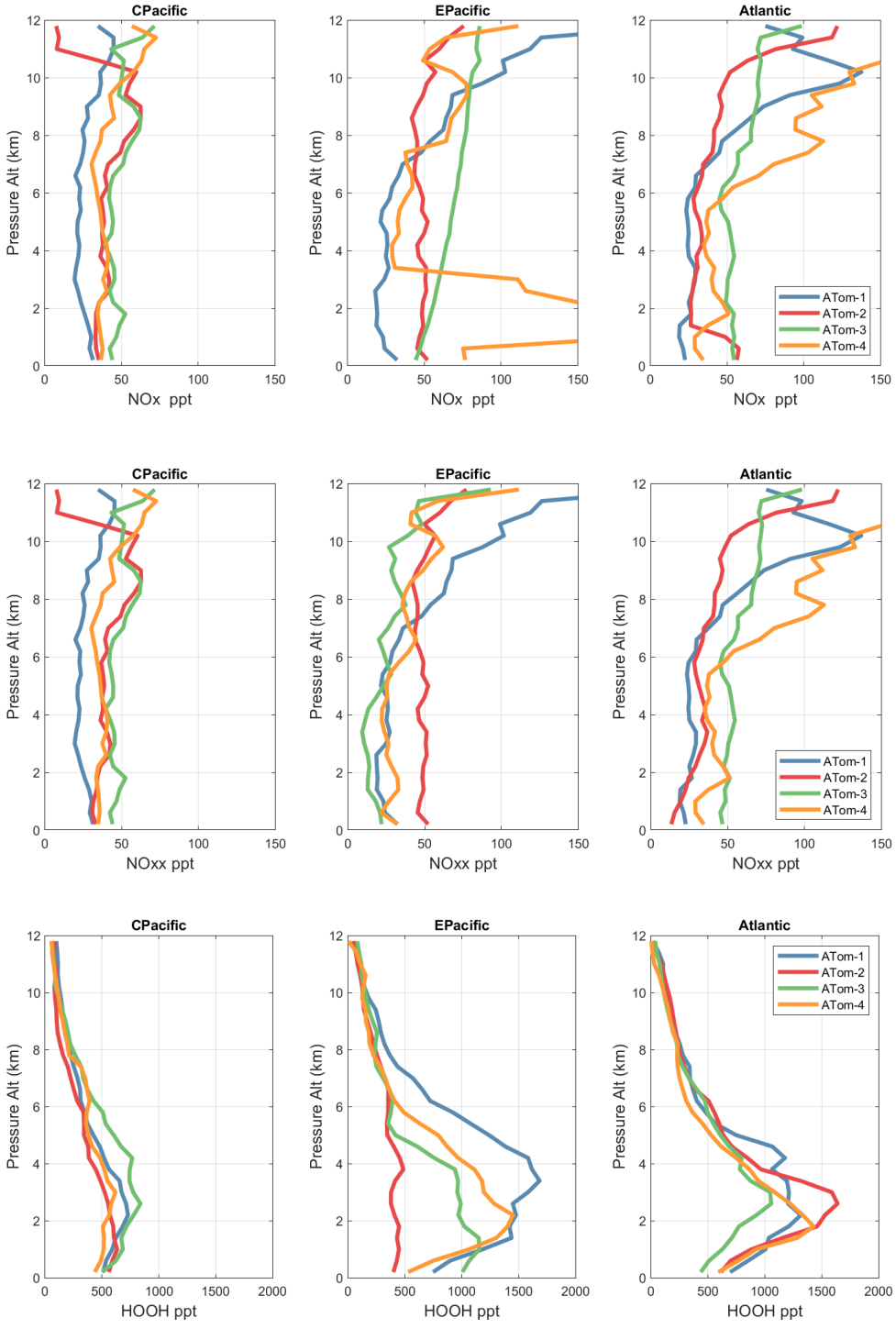

785

Figure 57. Vertical mean profiles (ppt vs pressure altitude) of NOx (v2b), NOxx (=NOx v3), HOOH (v2b) over the three tropical ocean regions (Central Pacific, Eastern Pacific, Atlantic). See Fig. 56.

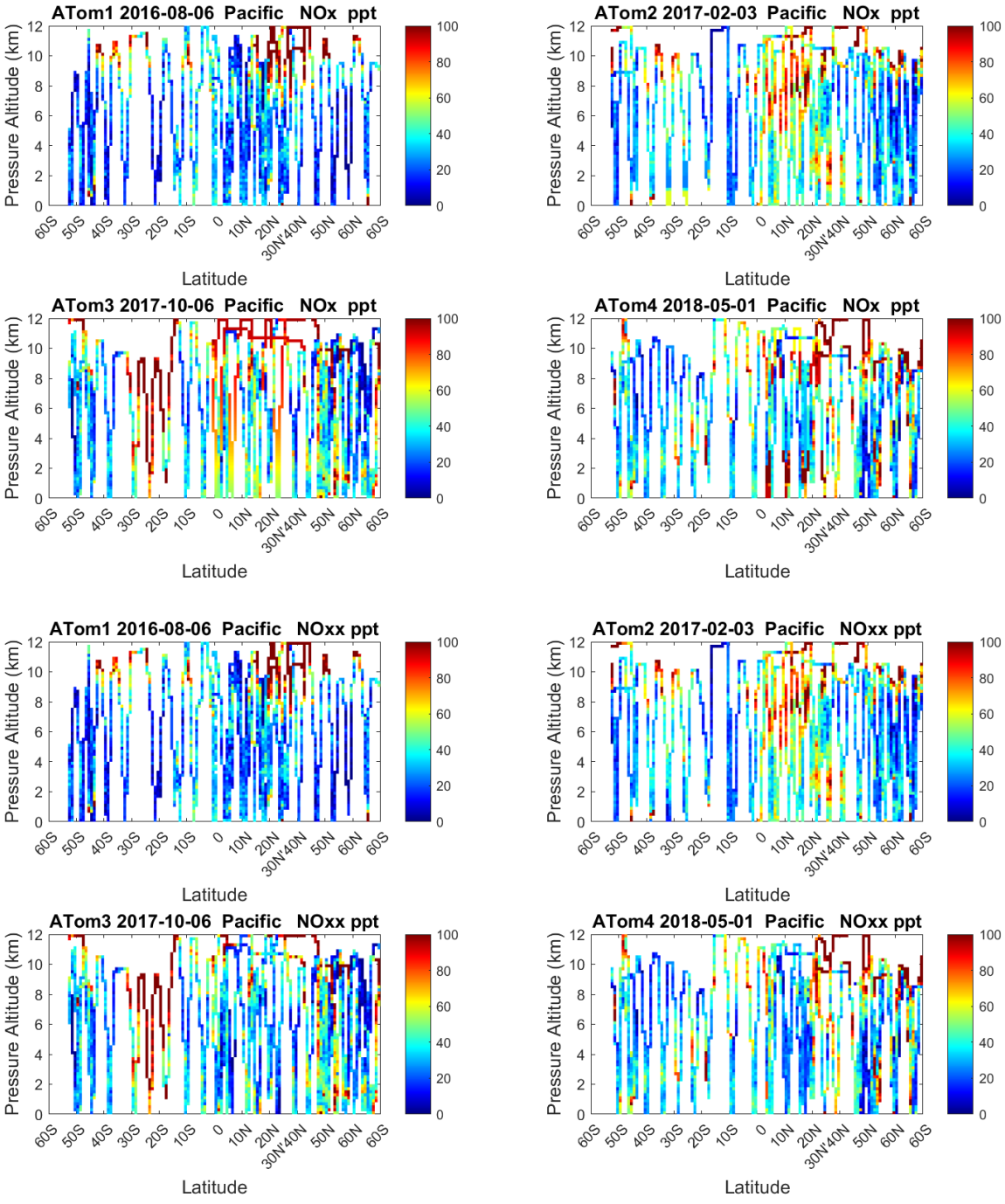

790

Figure 58. 2D Pacific curtain profiles for ATom-1234 of NOx (v2b) and NOxx (=NOx v3).

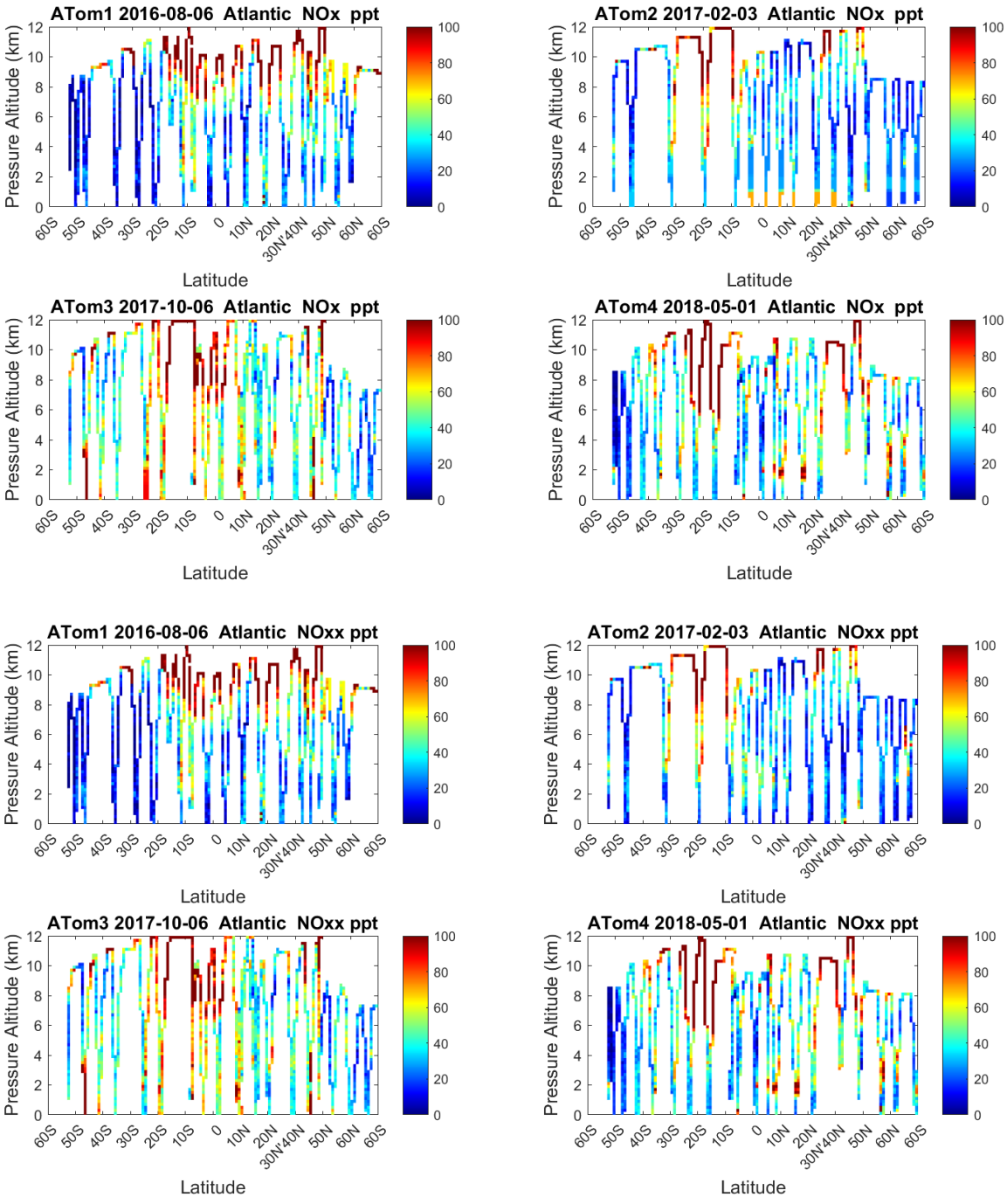

795

Figure 59. 2D Atlantic curtain profiles for ATom-1234 of NOx (v2b) and NOxx (=NOx v3).

800

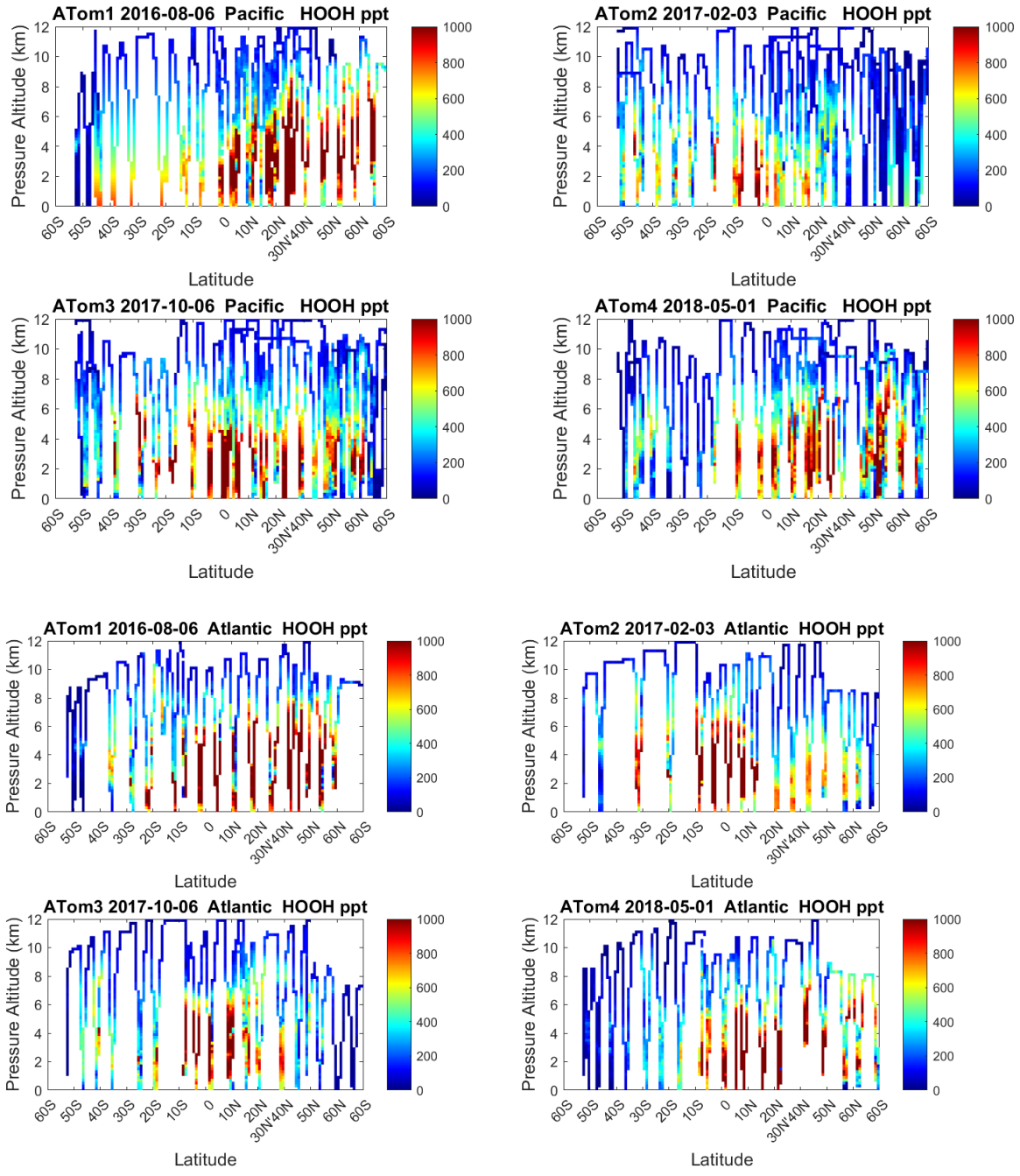

Figure 60. 2D Pacific and Atlantic curtain profiles for ATom-1234 of HOOH.

805

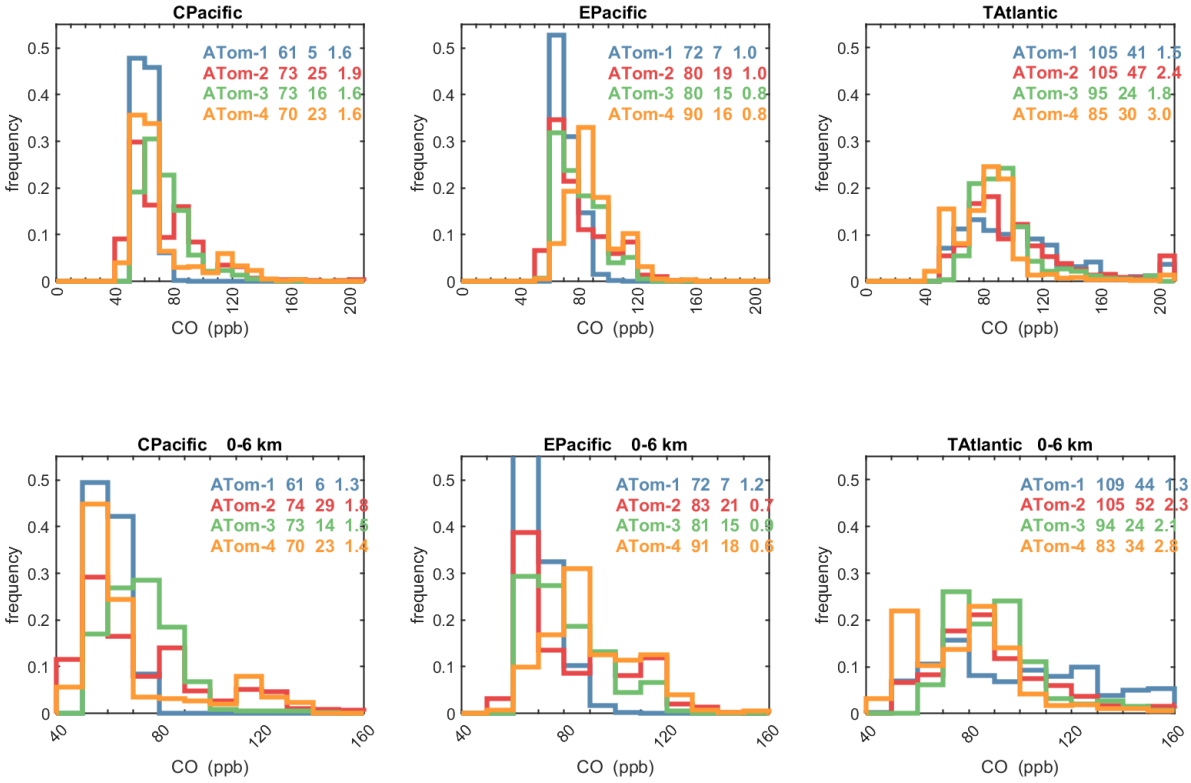

Figure 61. Probability Density of CO (ppb) in the 3 tropical basins (30°S-30°N) for ATom-1234. The standard weighting of ATom 10s air parcels is used. The lower panel shows 0-6 km pressure altitude where most of the chemical reactivity is located; while the upper panel shows the full troposphere, approximately 0-12 km. The color coding in the legend identifies the 4 ATom deployments. The numbers in the legend are, successively, the mean value, standard deviation, and skewness in ppb.

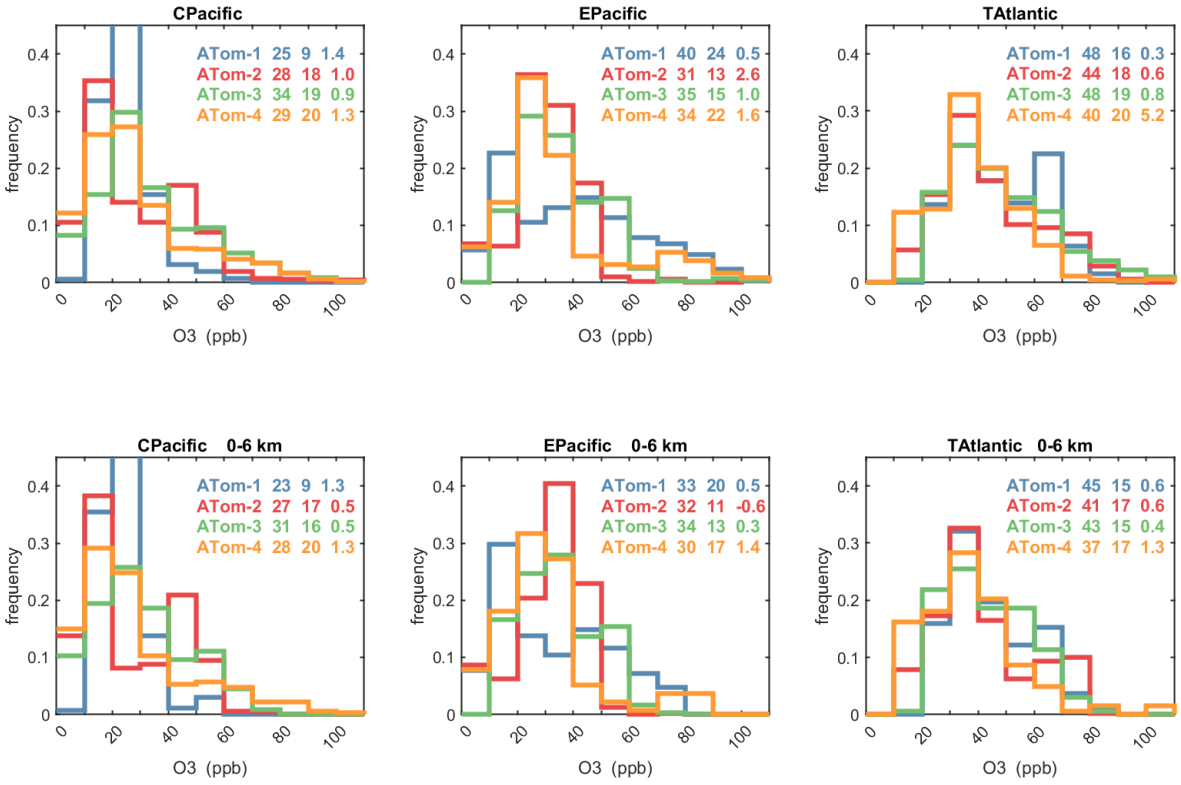

820 **Figure 62.** Probability Density of O_3 (ppb) in the 3 tropical basins (30°S-30°N) for ATom-1234. See Fig. 61. The numbers in the legend are, successively, the mean value, standard deviation, and skewness in ppb.

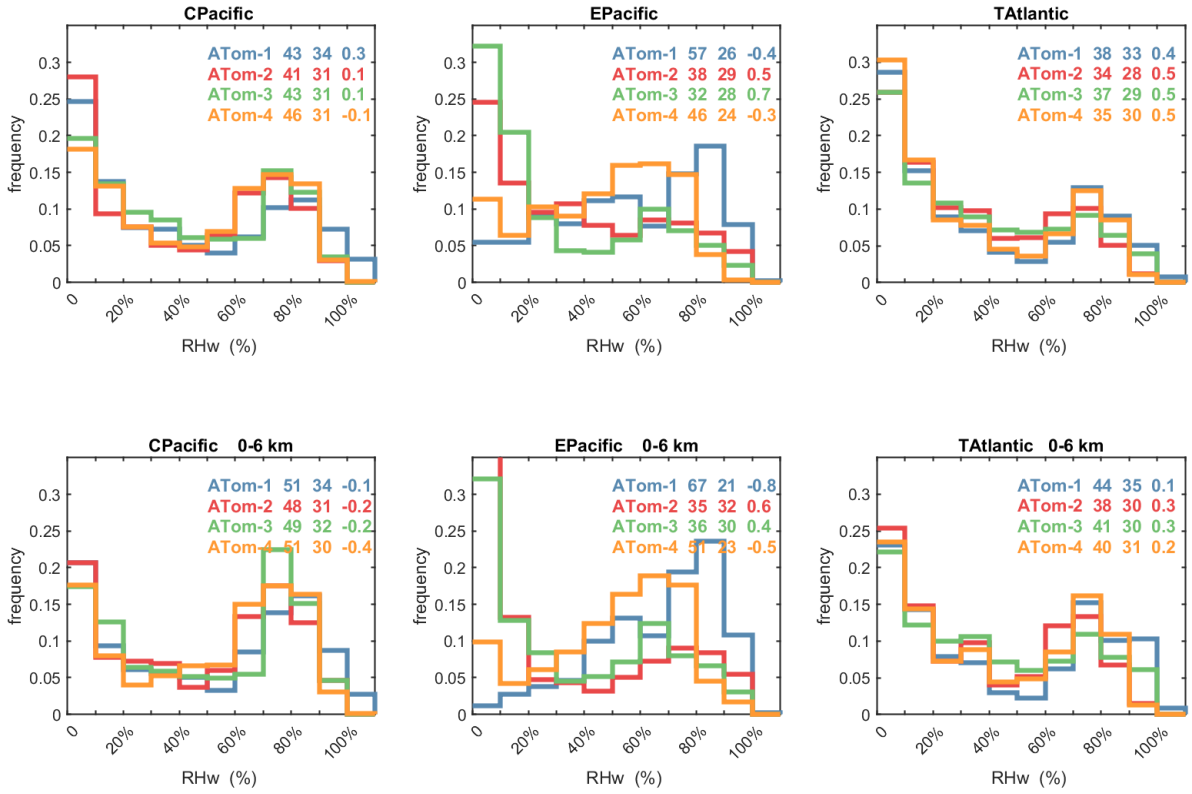

825

Figure 63. Probability Density of the relative humidity over liquid water (RHw, %) in the 3 tropical basins (30S-30N) for ATom-1234. See Fig. 61. The numbers in the legend are, successively, the mean value, standard deviation, and skewness in %.

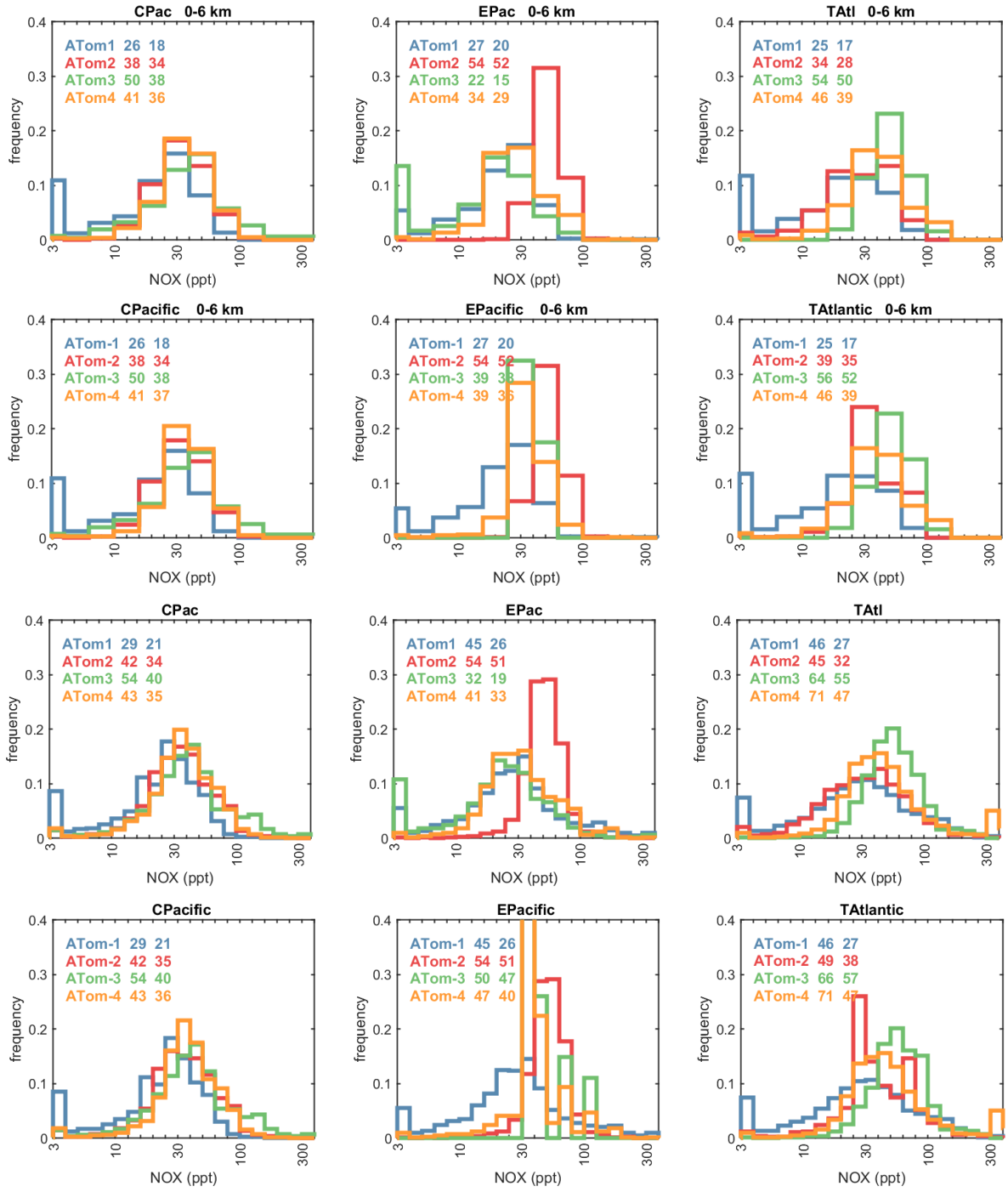

Figure 64. Probability Density of $\log_{10}$(NOx, ppt) in the 3 tropical basins (30°S-30°N) for ATom-1234, comparing MDS versions 3 and 2b. See Fig. 61. The numbers in the legend are, successively, the mean value of NOx and the mean value of the $\log_{10}$(NOx), both in ppt. The 4 successive rows are: 0-6 km, MDS V3 and V2b; and 0-12 km, MDS V3 and V2b.

Table 5. Probability densities of three key quantities for the tropical oceans: (a) CO (ppb), (b) O3 (ppb), (c) Relative humidity over water (%).

(a)	C.Pacific (30°S-30°N)					E.Pacific (0°-30°N)					T.Atlantic (30°S-30°N)			
	ATom1	ATom2	ATom3	ATom4		ATom1	ATom2	ATom3	ATom4		ATom1	ATom2	ATom3	ATom4
CO 0-12 km (ppb)														
mean	**61.4**	**73.4**	**73.5**	**70.5**		**72.1**	**80.1**	**80.2**	**89.6**		**104.6**	**105.3**	**94.9**	**84.8**
95%	72.4	122.2	108.1	125.9		85.1	118.5	111.4	119.4		187.8	202.3	145.5	127.9
80%	65.3	89.7	83.5	80.5		78.0	96.1	93.3	101.6		128.1	125.3	104.5	96.5
50%	60.2	64.5	70.3	62.7		69.7	74.5	77.3	87.5		97.9	92.7	90.8	84.4
20%	57.5	53.4	60.1	55.3		67.1	64.8	66.5	77.0		71.6	73.2	76.8	61.5
5%	54.9	48.1	57.7	50.1		63.5	58.9	63.0	67.0		57.9	56.0	69.5	51.1
CO 0-6 km (ppb)														
mean	**61.2**	**74.5**	**73.2**	**69.6**		**71.5**	**82.8**	**81.0**	**91.0**		**108.9**	**104.9**	**94.0**	**83.0**
95%	75.6	126.7	94.0	124.0		85.0	118.9	114.1	120.1		197.2	214.6	144.7	141.7
80%	65.1	91.7	83.4	86.2		76.6	103.1	92.4	108.7		140.3	123.1	101.4	98.4
50%	60.1	64.0	72.4	59.9		69.3	73.0	77.7	87.4		101.0	87.4	89.0	80.2
20%	56.8	52.7	60.4	53.8		66.5	64.2	66.7	76.5		72.0	70.6	75.8	55.6
5%	54.7	46.9	57.8	49.8		63.2	61.0	62.6	67.3		58.3	53.3	69.5	50.6

(b)	C.Pacific					E.Pacific					T.Atlantic			
	ATom1	ATom2	ATom3	ATom4		ATom1	ATom2	ATom3	ATom4		ATom1	ATom2	ATom3	ATom4
O_3 0-12 km (ppt)														
mean	**24.6**	**28.3**	**33.7**	**29.1**		**40.4**	**30.5**	**35.3**	**34.1**		**48.5**	**44.0**	**48.0**	**39.7**
95%	41.1	57.2	73.0	71.4		84.2	46.0	58.7	81.3		73.0	77.3	84.5	64.3
80%	30.4	46.5	50.7	41.3		63.3	39.8	48.5	42.8		64.6	62.6	63.3	51.5
50%	23.2	22.5	28.7	23.9		37.5	30.1	32.7	27.6		46.7	39.8	44.2	37.5
20%	16.8	11.2	18.5	12.7		15.1	22.1	21.7	19.8		32.6	29.5	30.9	25.8
5%	13.4	8.9	7.8	6.7		9.7	7.9	14.9	8.1		26.0	17.7	23.2	15.8
O_3 0-6 km (ppt)														
mean	**23.4**	**26.7**	**30.5**	**27.9**		**33.2**	**31.7**	**33.8**	**29.8**		**44.7**	**40.9**	**43.1**	**37.4**
95%	39.1	53.2	60.4	70.1		69.8	46.6	55.0	72.3		69.5	71.8	68.3	64.9
80%	29.1	46.8	47.3	41.3		51.0	41.6	46.0	37.2		60.4	58.1	56.9	47.8
50%	22.1	18.4	26.8	22.8		29.4	33.4	32.0	26.5		40.3	35.6	41.2	35.1
20%	15.4	10.7	16.2	11.3		12.9	23.4	21.1	16.8		30.9	28.2	29.6	21.7
5%	12.8	8.7	7.3	6.4		9.1	7.7	14.2	6.9		25.8	15.8	22.5	15.4

(c)	C.Pacific					E.Pacific					T.Atlantic			
	ATom1	ATom2	ATom3	ATom4		ATom1	ATom2	ATom3	ATom4		ATom1	ATom2	ATom3	ATom4
RHw 0-12 km (%)														
mean	**43.4**	**41.5**	**43.1**	**46.2**		**57.0**	**37.6**	**31.7**	**46.3**		**38.1**	**34.5**	**36.9**	**34.6**
95%	97.4	85.9	87.4	88.2		92.3	88.9	85.6	79.0		90.9	82.2	87.3	84.5
80%	81.1	74.7	77.2	77.7		82.7	68.8	64.7	68.5		76.7	66.2	69.3	72.1
50%	34.9	40.1	38.4	51.1		59.4	31.9	17.9	50.2		26.4	27.5	29.7	22.5
20%	7.6	6.0	10.1	11.0		29.6	7.8	6.8	22.1		5.7	6.1	7.7	6.3
5%	3.7	1.9	2.9	2.4		8.1	3.7	2.1	4.9		1.5	1.9	3.3	2.3
RHw 0-6 km (%)														
mean	**50.7**	**47.9**	**48.6**	**50.9**		**66.9**	**34.8**	**36.4**	**50.9**		**44.3**	**37.8**	**40.8**	**40.5**
95%	97.5	88.9	89.4	88.5		93.6	90.5	87.8	81.3		95.6	83.7	91.0	85.3
80%	84	78.3	79.7	79.8		84.6	72.7	68.9	73.7		80.9	71.2	74.9	74.7
50%	59.9	57.1	55.1	61.4		74.3	17.5	28.3	54.3		34.9	32.1	35.0	35.2
20%	9.2	9.2	11.1	11.1		48.0	6.2	8.2	29.8		4.8	5.3	8.8	8.4
5%	3.4	2.5	2.8	1.7		23.8	3.1	2.2	4.1		1.4	1.5	3.1	1.2

5.4 Heterogeneous Chemistry

The potential role of heterogeneous (gas-aerosol) chemical reactions—which are not included in this study—is illustrated with the profiles of aerosol surface area density SAD ($\mu m^2\ cm^{-3}$) in Fig. 65. We calculate SAD as the sum of the four reported modes (nucleation, Aitken, accumulation, coarse) with most of the area coming from accumulation and coarse modes. In the Pacific, above the marine boundary layer, SAD is usually < 20 $\mu m^2\ cm^{-3}$), while in the Atlantic SAD is much larger, 20-80 $\mu m^2\ cm^{-3}$ everywhere below 4 km. This difference is extensive in all seasons and clearly due to low-altitude continental convection from, e.g., biomass burning. There is one example in these profiles where such convection delivers high aerosol loading near 6 km in the E. Pacific (ATom-4). We calculate the frequency distribution of reactions for all parcels in ATom-1 Pacific and Atlantic assuming a high reactivity coefficient gamma = 0.10 in Fig. 66. If we are looking for heterogeneous reactions to compete with radical chemistry rates (e.g., ROO, HO_2), then we need a high gamma and reaction frequency > 2 per hour. For ATom-1 Pacific, that occurs in only 3% of the parcels, while for ATom-1 Atlantic, it is 17% of the parcels (as seen by the large SAD below 4 km). This evidence indicates that heterogeneous chemical reactions are not likely important in the reactivity statistics here, but a more thorough analysis considering the aerosol composition and realistic gammas is needed.

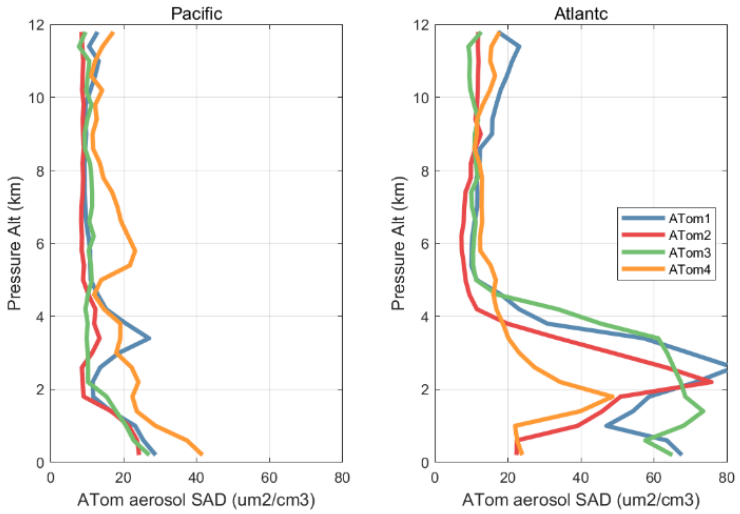

Figure 65. Vertical mean profiles of aerosol surface area density SAD ($\mu m^2\ cm^{-3}$), over the Pacific and Atlantic basins. Standard weighting, see text. SAD is the sum of the four reported modes (nucleation, Aitken, accumulation, coarse) with most of the area from accumulation and coarse modes.

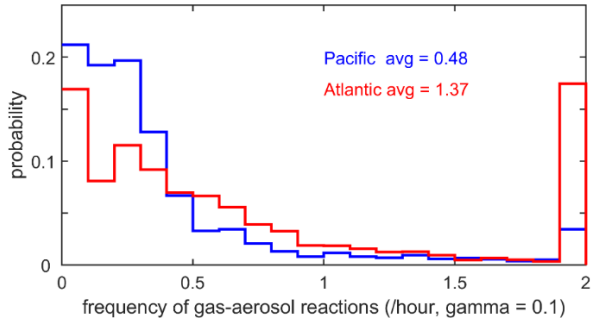

Figure 66. Frequency distribution of gas-aerosol reactions (per hour) for ATom-1 Pacific (blue) and Atlantic (red) assuming a high reactivity coefficient gamma = 0.10.

6. Chemical feedbacks

6.1 Timescale for O_3 perturbations

The sensitivities calculated for the parcels in ATom-1 allow us to estimate the timescale for an O_3 perturbation. Most modeling studies make the simplistic assumption that the P-O3 and L-O3 derived from the rates defined above are the key terms in the continuity equation and, further, that P-O3 is constant while L-O3 is linear in $[O_3]$.

$$d[O_3]/dt = \text{P-O3} - \text{L-O3} = P^{constant} - [O_3]\{\text{L-O3}/[O_3]\} = P^{constant} - [O_3]/T^A \quad (3)$$

The approximate timescale, $T^A = [O_3]/\text{L-O3}$, is often called the O_3 lifetime because the steady-state concentration is proportional to it: $[O_3]^{steady\text{-}state} = P^{constant}\, T^A$. This approximation is valid only if

$$d\ln[\text{L-O3}] / d\ln[\text{O3}] \equiv 1 \quad \text{and} \quad d\ln[\text{P-O3}] / d\ln[\text{O3}] \equiv 0 \quad (4)$$

but instead from Table 4 we have for ATom-1 Atlantic

$$d\ln[\text{L-O3}] / d\ln[\text{O3}] \equiv 1.01 \quad \text{and} \quad d\ln[\text{P-O3}] / d\ln[\text{O3}] \equiv -0.41 \quad (5)$$

So, L-O3 is very close to linear in $[O_3]$, but P-O3 decreases as $[O_3]$ increases, and thus the net P-minus-L (Eq 3) decreases faster, and an $[O_3]$ increase decays faster than given by T^A. The true timescale T^T is given by the linearized O_3 loss frequency.

$$1/T^T = d[-dO_3/dt] / d[O_3] \approx d[\text{L-O3} - \text{P-O3}] / d[O_3] \quad (6)$$

Figure 67 shows this linearized O_3 loss frequency ($1/T^T$, units of per day) for the Pacific and Atlantic flight profiles of ATom-1. High values, > 0.15 /d occur throughout the northern tropics below 5 km. In the upper troposphere, the timescale

for O_3 is slow, 20 days or longer. Basin mean loss frequency is similar in both Pacific (0.065 /d) and Atlantic (0.061 /d) corresponding to a mean timescale T^T ~ 16 days.

Profiles of the mean loss frequency, both $1/T^T$ and $1/T^A$, are shown for Pacific and Atlantic basins in Fig. 68. Both basins show almost the same profiles, increasing from 0.01 /d at 12 km to ~ 0.1 /d near the surface, with near constant differences, $1/T^T$ - $1/T^A$, of about +0.01 /d. Thus, the relative error in T^A decreases from 100% at 12 km to 10% at 0 km. The profiles of P-O3 and L-O3 in the basins in Fig. 68 indicate the shifting importance of the d[P-O3]/d[O_3] term with altitude.

Our sensitivity calculations are made with 24-hour integrations, and over this time the HOx and NOx radicals readjust to the O_3 increase, other species like HOOH partially respond, but for longer-lived key species such as CO (90 days) the adjustment is negligible. For O_3, the timescales for decay of the perturbation are 10-30 days, and thus we can ignore to first order any feedbacks on the chemistry caused by changes in CO or C_2H_6 or CH_4. Other, longer-chain alkanes might readjust in 10-30 days to the new levels of O_3, but these species are not very important for the ATom oceanic flights. Thus, our 24-hour sensitivity calculations should be adequate for deriving the timescale for decay of an O_3 perturbation.

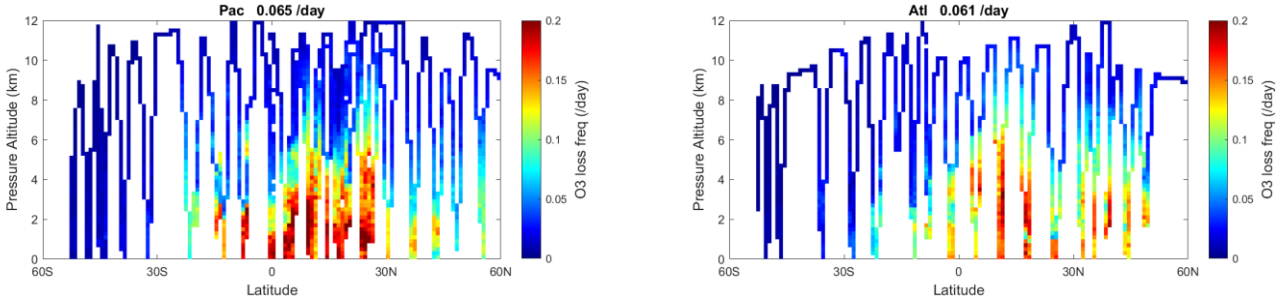

Figure 67. 2D curtain plots of the linearized loss frequency for O_3 ($1/T^T$ in units of per day) for ATom-1 Pacific and Atlantic basins. The loss frequency is calculated from the sensitivity calculation dln(L-O3 minus P-O3)/dln(O_3).

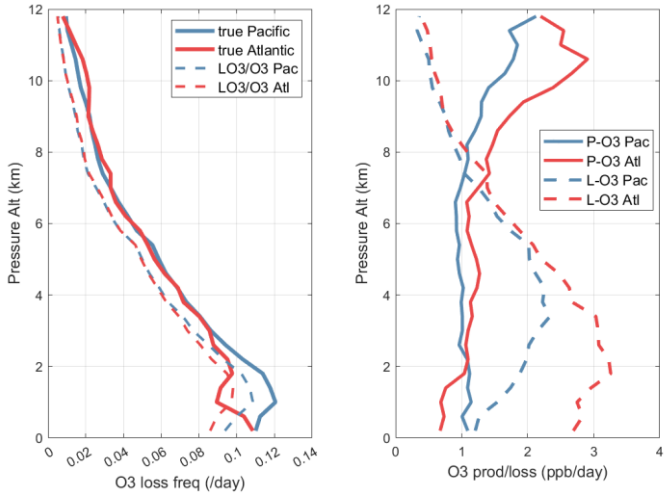

Figure 68. (left) O_3 loss frequency (/day) versus pressure altitude (km), averaged over Pacific (blue) and Atlantic (red) basins for ATom-1. True linearized loss frequency ($1/T^T$, solid lines) is compared with the often-used approximation ($1/T^A$ = L-O3/O_3. dashed lines). (right) Altitude profiles for both ocean basins of P-O3 (solid) and L-O3 (dashed), both in ppb/d.

6.2 CH_4 lifetime feedback

A positive perturbation to the CH_4 abundance reduces tropospheric OH and thus increases the timescale of the perturbation relative to its steady-state lifetime (Prather 1994, 1996). A measure of this chemical feedback is the sensitivity, dln[L-CH4]/dln[CH4] (% per %), calculated here. These sensitivities, for all ATom-1 10 s parcels including continental data, are plotted versus L-CH4 as small black dots in Fig. 69. The basin-mean values are shown for Pacific (large red dot, 0.76 % per %) and Atlantic (large blue dot, 0.80 % per %). The number we want from these calculations is the sensitivity of the OH weighted by the CH_4 loss (i.e., including the temperature factor in the rate coefficient, exp(-1775/T)).

$$s_{OH} = \text{dln[L-CH4]/dln[CH4]} - 1 \quad (7)$$

The values of s_{OH} for the ATom-1 parcels are plotted for the Pacific and Atlantic flight profiles in Fig. 70 (top panels), and the mean values are -0.24 and -0.20, respectively. The value of s_{OH} is most negative, about -0.3 in the lower troposphere, where CH_4 dominates the chemistry and controls much of the OH loss. The value of s_{OH} drops to below -0.1 in the upper troposphere where cold temperatures make the OH+CH4 reaction very slow compared with the OH+CO reaction. The CH4 feedback factor describes the increase in the timescale for a CH_4 perturbation relative to the OH lifetime in steady state (i.e., OH lifetime = atmospheric burden divided by loss to OH reactions).

$$ff_{CH4} = 1 / (1 + s_{OH}) \quad (8)$$

The values of ff_{CH4} along the flights tracks vary from about 1.2 to 1.6, see Fig. 70 (bottom panels). Averaging the two basins for s_{OH}, we calculate a mean $ff_{CH4} \sim 1.28$.

This 24-hour calculation, however, does not include the adjustment to other key species that will occur in response to the decadal decay of a CH_4 perturbation. The correct way to model this is to run CTM/CCM perturbation+control sequences for several years with different CH_4 lower boundary conditions (e.g., Holmes, 2018). During this time other species, specifically CO, which is the other major sink of OH radicals, will adjust to the CH_4-driven changes in OH. The CO change, an increase, will then further reduce OH and amplify the ff_{CH4}.

We can make a simple, first-order estimate of this CO adjustment to a 10% CH_4 increase. The s_{OH} directly from the CH_4 change averages -0.22 (Table 2, average of Pacific & Atlantic), or -2.2% change in the loss frequency of CH_4. The change in L-CO from the 10% CH_4 increase is -1.9% (Table 2, average of Pacific & Atlantic). If CO is in balance between sources and L-CO, then CO will increase by 1.9%. The two-basin average sensitivity of L-CH4 to CO is -0.37, so the CO increase will decrease L-CH4 by a further -0.7% to -2.9%. The updated s_{OH}* = -0.29, a 30% increase in magnitude, and the ff_{CH4}* = 1.41. This CO amplification may be an overestimate as some of the CO source, from CH_4 specifically, will be reduced with OH. Another correction is that the feedback factor used to calculate the perturbation time for a CH_4 pulse must be derived from the total CH_4 lifetime that includes losses in the stratosphere and to soils where the loss frequencies do not respond to a CH_4 perturbation (e.g., Holmes, 2018). This full budget calculation gives a reduced s_{TOTAL} = -0.25 and ff = 1.34, quite in line with recent global model results (1.30±0.07, Thornhill et al., 2021b). We do not support the use ATom-like chemical climatologies as a comparable result relative to the CTM/CCMs, but it does provide a measurement check point and estimate of first-order responses of tropospheric chemistry to global change.

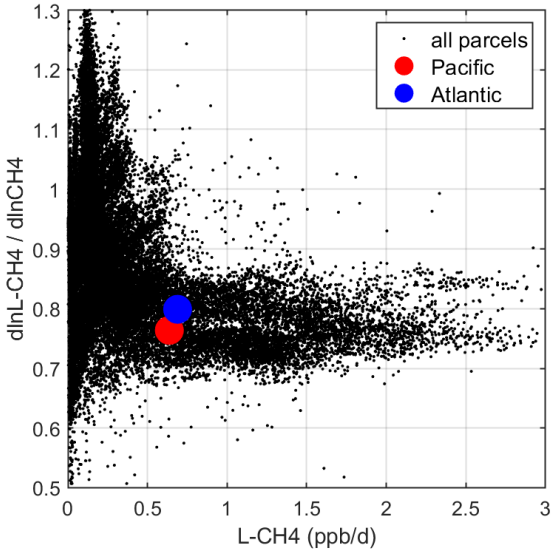

Figure 69. Sensitivity of CH_4 loss with respect to its abundance (dln[L-CH4]/dln[CH_4], in % per %) versus loss rate (L-CH4, in ppb/d) for parcels in ATom-1. All ATom-1 10 s parcels, including continental data, are plotted (small black dots) as well as the basin-mean values for Pacific (red dot) and Atlantic (blue dot).

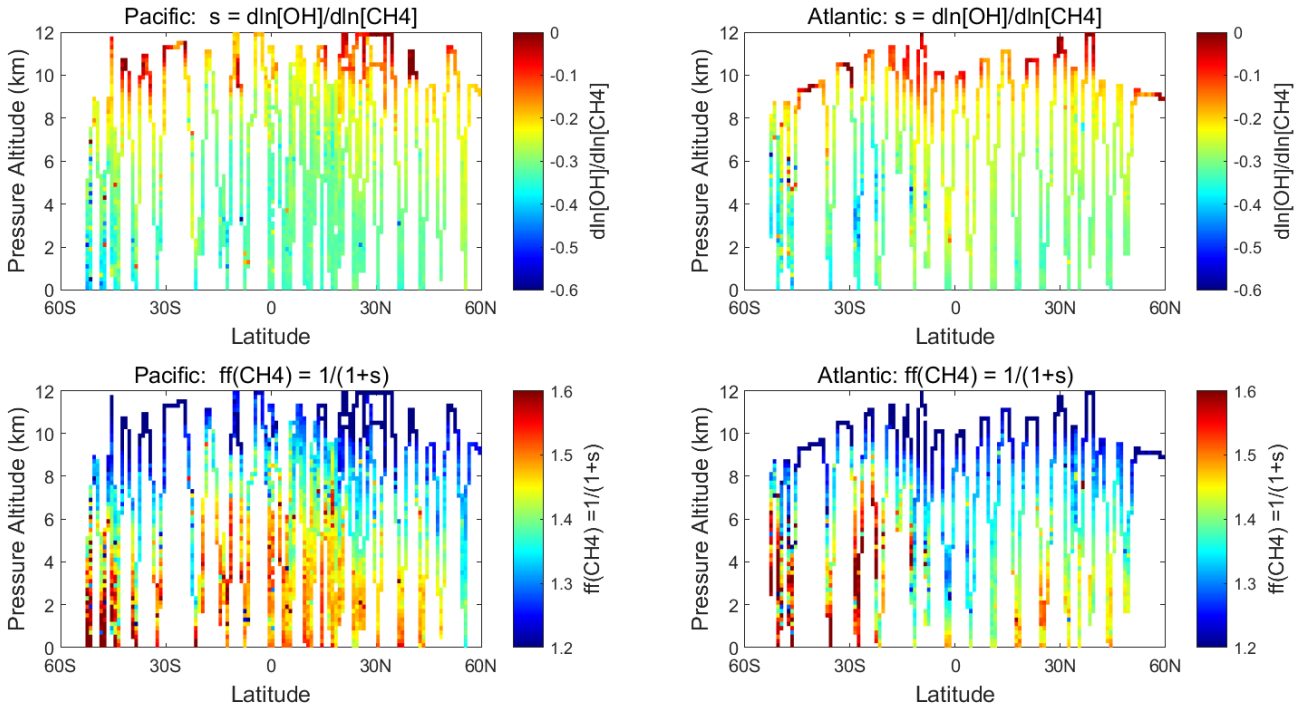

Figure 70. 2D curtain plots from ATom-1 of (top) the OH sensitivity to CH_4, s_{OH} = dln[OH]/dln[CH_4] = dln[L-CH4]/dln[CH_4] – 1, for Pacific and Atlantic basins, and (bottom) the CH_4 lifetime feedback factor, ff_{CH4} = 1/(1+s_{OH}) for the same.

7. Conclusions and Perspective

This manuscript completes the presentation and analysis of the ATom observations focusing on reactive, gas-phase chemistry affecting the tropospheric budgets of CH_4 and O_3. For the four seasonal deployments of ATom-1234 (August, February, October and May, respectively), we use the profiling curtains to identify large-scale regions of the troposphere that drive the budgets, particularly in the lower troposphere for loss of O_3 and CH_4, as well as the smaller heterogeneities, particularly in the upper troposphere for NOx-driven hot spots of O_3 production. These results are the first near-global views of the remote troposphere, primarily the middle of the Pacific and Atlantic Ocean basins, from the perspective of their net chemical reactivities based on observations at 200 m scales. Statistics are also accumulated for the Southern Ocean and Arctic basin, but as expected from global chemistry models, these regions contribute little to the global O_3 and CH_4 budgets.

ATom's regular profiling of the ocean basins allows for weighted averages to build probability densities for key species and reactivities. Although the individual curtain plots for each ocean transect show clear meteorological variability for each deployment, these probability densities are quite similar and provide a robust test for the modeled distribution of species and reaction rates. For example, the 30°S-30°N tropical distributions of O_3, CO and relative humidity are distinct between the

Pacific and Atlantic (higher values of both) but similar for each deployment in each basin. On the other hand, the Eastern Pacific transect (0°-30°N, 121°W) is very different for each deployment. The compelling statistics built up from the ATom deployments are a metric that should be used to evaluate our current global chemistry models.

The Modeling Data Stream (MDS) developed for ATom (G2023 plus this publication) relies on gap-filling for sporadic measurements or missing data and is essential if reactivities for the 10 s air parcels are to be calculated without losing most of the parcels. The MDS concept was a reasonable and necessary step for the Reactivity Data Stream (RDS); however, as we have seen with the successive MDS versions, there is a painful learning curve for what to do with missing data and no truly optimal method yet identified. The MDS/RDS approach defined in the pre-ATom deployment papers (P2017; P2018) is still the best method for calculation diel-averaged rates. The ATom-method of inserting the observed chemical composition of 10 s parcels in global chemistry models to calculate reaction rates (RDS) remains a compromise: integrating without sources or sinks means that NOx and alkanes decrease over 24 hours while HOOH and CH_3OOH increases. We cannot identify a method of including these that does not also prejudice the results and that remains easy to implement in most global models. One improvement might be to use satellite derived photolysis rates for the day of observation (e.g., Holmes, 2016) rather than just having the models pick 5 days from their own meteorology fields to average over.

The calculation of reactivities (R) with the RDS protocol allows us to step further and derive the sensitivity factors ($S = d\ln(R)/d\ln(X)$) relative to the chemical species (X). From these sensitivities, we can identify the critical species where model error in their atmospheric simulation will cause large errors in the budgets. This information is useful in directing model-measurement comparisons. From the sensitivities, we have also derived correctly linearized lifetimes and even the CH_4 chemical feedback. Admittedly these are only first-order estimates and do not include the full set of feedbacks in a flux-driven, free-running global chemistry model. Nevertheless, it does provide an independent estimate based primarily on observations.

The ATom measurements can provide a substantial contribution to understanding model differences and even identifying model errors in global tropospheric chemistry. What is clear from this measurement-model analysis since P2017 is that most of the model difference is caused by models calculating different climatologies for the key species such as O_3, CO, H_2O, NOx, CH_4 plus T. When models use the same distribution of key species, they calculate nearly the same reactivities even though their chemical models have a wide range of species and complexity.

There remain uncertainties in kinetic rates and cross sections, yet models tend to use the same values (e.g., Burkholder et al., 2020). Using fixed MDS chemical composition, the model differences are due mostly to variability in photolysis rates driven by clouds (Hall et al., 2018). For example, the model-model root-mean-square differences in reactivities adopting the same chemical composition are ~10% using the same model but different years (hence different cloud fields); they are ~20% for different models that come close to matching one another; they reach 50% if those models use different H_2O and T; and they exceed 100% for some models that are known to be aberrant in other diagnostics. Thus, the most important model metric to develop from the ATom measurements would be standard probability densities of the key species in those regions where reactivities are largest: the lower tropics for loss of O_3 and CH_4, the upper tropics for production of O_3. These could include co-variation patterns (2D probability densities, in G2023). Sensitivity analysis of the 24-hour reactivities provides some core data that we feel should become a standard part of CCM evaluations and inter-comparisons.

The other ATom information that is important to understand for tropospheric chemistry but is not readily a metric, are the unusual large-scale air masses (20° in latitude) of high reactivity that are clearly transient events, most likely of continental origin: ATom-3 south Tropical Atlantic large mass of high-NOx, high P-O3 surrounded by high L-O3; ATom-14 Eastern Pacific huge air masses of very high L-O3. Overall, the ATom data set based on 10 s (2 km) air parcels, has allowed us to partially deconstruct the spatial scales and variability that defines tropospheric chemistry from composition to reactivity.

Data/Code Availability. The full raw ATom data set is first posted short-term on the NASA ESPO ATom website (https://espo.nasa.gov/atom/content/ATom). The final archive for ATom data and merged data sets will be at Oak Ridge National Laboratory (ORNL), see https://daac.ornl.gov/ATOM/guides/ATom_merge.html, and Wofsy et al., 2021. The MDS and RDS data sets as well as the MATLAB codes and some intermediate data used in this analysis are posted on Dryad (https://doi.org/10.7280/D1B12H, see Prather et al., 2023). Earlier versions, primarily for ATom-1 based on Guo et al. (2021; 2023), are posted on Dryad (https://doi.org/10.7280/D1Q699 and link to https://zenodo.org/record/5905662#.ZBS1Kx_MIlw, see Guo, 2022).

Author contribution. MJP designed the analysis, developed the MDS, and wrote the manuscript. HG and XZ performed most of the RDS calculations. HG worked on the MDS design and co-wrote the manuscript.

Competing interests. The authors declare that they have no conflict of interest.

Acknowledgements. The authors are indebted to the entire ATom Science Team including the managers, pilots and crew, who made this mission possible. We thank the instrument teams who were co-authors on the first paper (Guo et al., 2023) for this valuable data set. Primary funding of the preparation of this paper at UC Irvine was through NASA grants NNX15AG57A and 80NSSC21K1454.

References

Allen, H. M., Crounse, J. D., Kim, M. J., Teng, A. P., Ray, E. A., McKain, K., Ray E.A., Sweeney, C., and Wennberg, P.O.: H_2O_2 and CH_3OOH (MHP) in the remote atmosphere: 1. Global distribution and regional influences. Journal of Geophysical Research: Atmospheres, 127, e2021JD035701. https://doi.org/10.1029/2021JD035701, 2022.

Anderson, D. C., B. N. Duncan, A. M. Fiore, C. B. Baublitz, M. B. Follette-Cook, J. M. Nicely, and G. M. Wolfe (2021), Spatial and temporal variability in the hydroxyl (OH) radical: understanding the role of large-scale climate features and their influence on OH through its dynamical and photochemical drivers, Atmos Chem Phys, 21(8), 6481-6508, 10.5194/acp-21-6481-2021, 2021.

Brock, C. A., Froyd, K. D., Dollner, M., Williamson, C. J., Schill, G., Murphy, D. M., Wagner, N. J., Kupc, A., Jimenez, J. L., Campuzano-Jost, P., Nault, B. A., Schroder, J. C., Day, D. A., Price, D. J., Weinzierl, B., Schwarz, J. P., Katich, J. M., Wang, S. Y., Zeng, L. H., Weber, R., Dibb, J., Scheuer, E., Diskin, G. S., DiGangi, J. P., Bui, T., Dean-Day, J. M., Thompson, C. R., Peischl, J., Ryerson, T. B., Bourgeois, I., Daube, B. C., Commane, R., and Wofsy, S. C. (2021) Ambient aerosol properties in the remote atmosphere from global-scale in situ measurements, Atmos Chem Phys, 21(19), 15023-15063, 10.5194/acp-21-15023-2021, 2021.

Brune, W. H., Miller, D. O., Thames, A. B., Allen, H. M., Apel, E. C., Blake, D. R., Bui, T. P., Commane, R., Crounse, J. D., Daube, B. C., Diskin, G. S., DiGangi, J. P., Elkins, J. W., Hall, S. R., Hanisco, T. F., Hannun, R. A., Hintsa, E. J., Hornbrook, R. S., Kim, M. J., McKain, K., Moore, F. L., Neuman, J. A., Nicely, J. M., Peischl, J., Ryerson, T. B., St Clair, J. M., Sweeney, C., Teng, A. P., Thompson, C., Ullmann, K., Veres, P. R., Wennberg, P. O., and Wolfe, G. M. (2020): Exploring Oxidation in the Remote Free Troposphere: Insights From Atmospheric Tomography (ATom), J Geophys Res-Atmos, 125, ARTN e2019JD031685, 10.1029/2019JD031685, 2020.

Burkholder, J.B.; Sander, S.P.; Abbatt, J.P.D.; Barker, J.R.; Cappa, C.; Crounse, J.D.; Dibble, T.S.; Huie, R.E.; Kolb, C.E.; Kurylo, M.J.; Orkin, V.L.; Percival, C.J.; Wilmouth, D.M.; Wine, P.H. (2020) "Chemical Kinetics and Photochemical Data for Use in Atmospheric Studies, Evaluation No. 19," JPL Publication 19-5, Jet Propulsion Laboratory, Pasadena, May 2020, http://jpldataeval.jpl.nasa.gov, 2020.

Griffiths, P. T., Murray, L. T., Zeng, G., Shin, Y. M., Abraham, N. L., Archibald, A. T., Deushi, M., Emmons, L. K., Galbally, I. E., Hassler, B., Horowitz, L. W., Keeble, J., Liu, J., Moeini, O., Naik, V., O'Connor, F. M., Oshima, N., Tarasick, D., Tilmes, S., Turnock, S. T., Wild, O., Young, P. J., and Zanis, P. (2021) Tropospheric ozone in CMIP6 simulations, Atmos Chem Phys, 21, 4187-4218, 10.5194/acp-21-4187-2021, 2021.

Guo, Hao (2022), Heterogeneity and chemical reactivity of the remote Troposphere defined by aircraft measurements, Dryad, Dataset, https://doi.org/10.7280/D1Q699, 2022.

Guo, H., Flynn, C. M., Prather, M. J., Strode, S. A., Steenrod, S. D., Emmons, L., Lacey, F., Lamarque, J.-F., Fiore, A. M., Correa, G., Murray, L. T., Wolfe, G. M., St. Clair, J. M., Kim, M., Crounse, J., Diskin, G., DiGangi, J., Daube, B. C., Commane, R., McKain, K., Peischl, J., Ryerson, T. B., Thompson, C., Hanisco, T. F., Blake, D., Blake, N. J., Apel, E. C., Hornbrook, R. S., Elkins, J. W., Hintsa, E. J., Moore, F. L., and Wofsy, S.: Heterogeneity and Chemical Reactivity of the Remote Troposphere defined by Aircraft Measurements, Atmos. Chem. Phys., 21, 13729–13746, https://doi.org/10.5194/acp-21-13729-2021, 2021, see Guo et al., 2023.

Guo, H., Flynn, C. M., Prather, M. J., Strode, S. A., Steenrod, S. D., Emmons, L., Lacey, F., Lamarque, J.-F., Fiore, A. M., Correa, G., Murray, L. T., Wolfe, G. M., St. Clair, J. M., Kim, M., Crounse, J., Diskin, G., DiGangi, J., Daube, B. C., Commane, R., McKain, K., Peischl, J., Ryerson, T. B., Thompson, C., Hanisco, T. F., Blake, D., Blake, N. J., Apel, E. C., Hornbrook, R. S., Elkins, J. W., Hintsa, E. J., Moore, F. L., and Wofsy, S., (2023). Heterogeneity and Chemical Reactivity of the Remote Troposphere defined by Aircraft Measurements - CORRECTED, Atmos. Chem. Phys., 23, 99-117, 10.5194/acp-23-99-2023, 2023.

Hall, Samuel R., Kirk Ullmann, Michael J. Prather, Clare M. Flynn, Lee T. Murray, Arlene M. Fiore, Gustavo Correa, Sarah A. Strode, Stephen D. Steenrod, Jean-Francois Lamarque, Jonathon Guth, Béatrice Josse, Johannes Flemming, Vincent Huijnen, N. Luke Abraham, and Alex T. Archibald (2018) Cloud impacts on photochemistry: a new climatology of photolysis rates from the Atmospheric Tomography mission, Atmos. Chem. Phys., 18, 16809–16828, doi: 10.5194/acp-18-16809-2018, 2018.

Holmes, C.D. (2016) Sat-J: a satellite-derived dataset of global atmospheric photolysis rates, AGU Fall Meeting Abstracts, 2016, abstract #A33A-0189. https://agu.confex.com/agu/fm16/meetingapp.cgi/Paper/182189, 2016.

Holmes, C. D. (2018). Methane feedback on atmospheric chemistry: Methods, models, and mechanisms. Journal of Advances in Modeling EarthSystems,10, 1087–1099. doi: 10.1002/2017MS001196, 2018.

Holmes, C. D., M. J. Prather, O. A. Sovde, and G. Myhre (2013), Future methane, hydroxyl, and their uncertainties: key climate and emission parameters for future predictions, Atmos Chem Phys, 13(1), 285-302, 10.5194/acp-13-285-2013, 2013.

Prather, M.J. (1994) Lifetimes and eigenstates in atmospheric chemistry, Geophys.Res.Lett., 21, 801-804, 1994.

Prather, M.J. (1996) Natural modes and time scales in atmospheric chemistry: theory, GWPs for CH4 and CO, and runaway growth, Geophys.Res.Lett., 23, 2597-2600, 1996.

Prather, M. J. (2009), Tropospheric O_3 from photolysis of O_2, Geophys. Res. Lett., 36, L03811, 10.1029/2008GL036851, 2009.

Prather, M.J., Flynn, C.M., Zhu, X., Steenrod, S.D., Strode, S.A., Fiore, A.M., Correa, G., Murray, L.T. and Lamarque, J.F., (2018). How well can global chemistry models calculate the reactivity of short-lived greenhouse gases in the remote troposphere, knowing the chemical composition. Atmospheric Measurement Techniques, 11(5), 2653-2668, https://doi.org/10.5194/amt-11-2653-2018, 2018.

Prather, M.J., Zhu, X., Flynn, C.M., Strode, S.A., Rodriguez, J.M., Steenrod, S.D., Liu, J., Lamarque, J.F., Fiore, A.M., Horowitz, L.W. and Mao, J., (2017). Global atmospheric chemistry–which air matters. Atmospheric Chemistry and Physics, 17(14), 9081-9102, 10.5194/acp-17-9081-2017, 2017.

Prather, M. J., Guo, H., Flynn, C. M., Strode, S. A., Steenrod, S. D., Emmons, L., Lacey, F., Lamarque, J.-F., Fiore, A. M., Correa, G., Murray, L. T., Wolfe, G. M., St. Clair, J. M., Kim, M., Crounse, J., Diskin, G., DiGangi, J., Daube, B. C., Commane, R., McKain, K., Peischl, J., Ryerson, T. B., Thompson, C., Hanisco, T. F., Blake, D., Blake, N. J., Apel, E. C., Hornbrook, R. S., Elkins, J. W., Hintsa, E. J., Moore, F. L., and Wofsy, S., (2023), Heterogeneity and chemical reactivity of the remote troposphere defined by the NASA ATom Mission aircraft measurements – the Modeling and Reactivity Data Streams (MDS & RDS), Dryad, Dataset, https://doi.org/10.7280/D1B12H, 2023.

Schill, G. P., Froyd, K. D., Bian, H., Kupc, A., Williamson, C., Brock, C. A., Ray, E., Hornbrook, R. S., Hills, A. J., Apel, E. C., Chin, M., Colarco, P. R., and Murphy, D. M. (2020), Widespread biomass burning smoke throughout the remote troposphere, Nat Geosci, 13, 422-425, 10.1038/s41561-020-0586-1, 2020.

Stevenson, D. S., Young, P. J., Naik, V., Lamarque, J. F., Shindell, D. T., Voulgarakis, A., Skeie, R. B., Dalsoren, S. B., Myhre, G., Berntsen, T. K., Folberth, G. A., Rumbold, S. T., Collins, W. J., MacKenzie, I. A., Doherty, R. M., Zeng, G., van Noije, T. P. C., Strunk, A., Bergmann, D., Cameron-Smith, P., Plummer, D. A., Strode, S. A., Horowitz, L., Lee, Y. H., Szopa, S., Sudo, K., Nagashima, T., Josse, B., Cionni, I., Righi, M., Eyring, V., Conley, A., Bowman, K. W., Wild, O., and

Archibald, A., (2013), Tropospheric ozone changes, radiative forcing and attribution to emissions in the Atmospheric Chemistry and Climate Model Intercomparison Project (ACCMIP), Atmos Chem Phys, 13, 3063-3085, 10.5194/acp-13-3063-2013, 2013.

Strode, S. A., J. H. Liu, L. Lait, R. Commane, B. Daube, S. Wofsy, A. Conaty, P. Newman, and M. Prather (2018), Forecasting carbon monoxide on a global scale for the ATom-1 aircraft mission: insights from airborne and satellite observations and modeling, Atmos Chem Phys, 18(15), 10955-10971, 10.5194/acp-18-10955-2018, 2018.

Thompson, C. R., Wofsy, S. C., Prather, M. J., Newman, P. A., Hanisco, T. F., Ryerson, T. B., Fahey, D. W., Apel, E. C., Brock, C. A., Brune, W. H., Froyd, K., Katich, J. M., Nicely, J. M., Peischl, J., Ray, E., Veres, P. R., Wang, S., Allen, H. M., Asher, E., Bian, H., Blake, D., Bourgeois, I., Budney, J., Bui, T. P., Butler, A., Campuzano-Jost, P., Chang, C., Chin, M., Commane, R., Correa, G., Crounse, J. D., Daube, B., Dibb, J. E., Digangi, J. P., Diskin, G. S., Dollner, M., Elkins, J. W., Fiore, A. M., Flynn, C. M., Guo, H., Hall, S. R., Hannun, R. A., Hills, A., Hintsa, E. J., Hodzic, A., Hornbrook, R. S., Huey, L. G., Jimenez, J. L., Keeling, R. F., Kim, M. J., Kupc, A., Lacey, F., Lait, L. R., Lamarque, J., Liu, J., Mckain, K., Meinardi, S., Miller, D. O., Montzka, S. A., Moore, F. L., Morgan, E. J., Murphy, D. M., Murray, L. T., Nault, B. A., Neuman, J. A., Nguyen, L., Gonzalez, Y., Rollins, A., Rosenlof, K., Sargent, M., Schill, G., Schwarz, J. P., St. Clair, J. M., Steenrod, S. D., Stephens, B. B., Strahan, S. E., Strode, S. A., Sweeney, C., Thames, A. B., Ullmann, K., Wagner, N., Weber, R., Weinzierl, B., Wennberg, P. O., Williamson, C. J., Wolfe, G. M., & Zeng, L., (2021), The NASA Atmospheric Tomography (ATom) Mission: Imaging the Chemistry of the Global Atmosphere, Bulletin of the American Meteorological Society, on-line release, 10.1175/bams-d-20-0315.1, 2021.

Thornhill, G., Collins, W., Olivié, D., Skeie, R. B., Archibald, A., Bauer, S., Checa-Garcia, R., Fiedler, S., Folberth, G., Gjermundsen, A., Horowitz, L., Lamarque, J.-F., Michou, M., Mulcahy, J., Nabat, P., Naik, V., O'Connor, F. M., Paulot, F., Schulz, M., Scott, C. E., Séférian, R., Smith, C., Takemura, T., Tilmes, S., Tsigaridis, K., and Weber, J.: Climate-driven chemistry and aerosol feedbacks in CMIP6 Earth system models, Atmos. Chem. Phys., 21, 1105–1126, https://doi.org/10.5194/acp-21-1105-2021, 2021a.

Thornhill, G. D., Collins, W. J., Kramer, R. J., Olivié, D., Skeie, R. B., O'Connor, F. M., Abraham, N. L., Checa-Garcia, R., Bauer, S. E., Deushi, M., Emmons, L. K., Forster, P. M., Horowitz, L. W., Johnson, B., Keeble, J., Lamarque, J.-F., Michou, M., Mills, M. J., Mulcahy, J. P., Myhre, G., Nabat, P., Naik, V., Oshima, N., Schulz, M., Smith, C. J., Takemura, T., Tilmes, S., Wu, T., Zeng, G., and Zhang, J.: Effective radiative forcing from emissions of reactive gases and aerosols – a multi-model comparison, Atmos. Chem. Phys., 21, 853–874, https://doi.org/10.5194/acp-21-853-2021, 2021b.

Travis, K. R., Heald, C. L., Allen, H. M., Apel, E. C., Arnold, S. R., Blake, D. R., Brune, W. H., Chen, X., Commane, R., Crounse, J. D., Daube, B. C., Diskin, G. S., Elkins, J. W., Evans, M. J., Hall, S. R., Hintsa, E. J., Hornbrook, R. S., Kasibhatla, P. S., Kim, M. J., Luo, G., McKain, K., Millet, D. B., Moore, F. L., Peischl, J., Ryerson, T. B., Sherwen, T., Thames, A. B., Ullmann, K., Wang, X., Wennberg, P. O., Wolfe, G. M., and Yu, F. Q. (2020), Constraining remote oxidation capacity with ATom observations, Atmos Chem Phys, 20, 7753-7781, 10.5194/acp-20-7753-2020, 2020.

Veres, P. R., Neuman, J. A., Bertram, T. H., Assaf, E., Wolfe, G. M., Williamson, C. J., Weinzierl, B., Tilmes, S., Thompson, C. R., Thames, A. B., Schroder, J. C., Saiz-Lopez, A., Rollins, A. W., Roberts, J. M., Price, D., Peischl, J., Nault,

B. A., Moller, K. H., Miller, D. O., Meinardi, S., Li, Q. Y., Lamarque, J. F., Kupc, A., Kjaergaard, H. G., Kinnison, D., Jimenez, J. L., Jernigan, C. M., Hornbrook, R. S., Hills, A., Dollner, M., Day, D. A., Cuevas, C. A., Campuzano-Jost, P., Burkholder, J., Bui, T. P., Brune, W. H., Brown, S. S., Brock, C. A., Bourgeois, I., Blake, D. R., Apel, E. C., and Ryerson, T. B. (2020), Global airborne sampling reveals a previously unobserved dimethyl sulfide oxidation mechanism in the marine atmosphere, P Natl Acad Sci USA, 117, 4505-4510, 10.1073/pnas.1919344117, 2020.

Voulgarakis, A., Naik, V., Lamarque, J. F., Shindell, D. T., Young, P. J., Prather, M. J., Wild, O., Field, R. D., Bergmann, D., Cameron-Smith, P., Cionni, I., Collins, W. J., Dalsoren, S. B., Doherty, R. M., Eyring, V., Faluvegi, G., Folberth, G. A., Horowitz, L. W., Josse, B., MacKenzie, I. A., Nagashima, T., Plummer, D. A., Righi, M., Rumbold, S. T., Stevenson, D. S., Strode, S. A., Sudo, K., Szopa, S., and Zeng, G., (2013), Analysis of present day and future OH and methane lifetime in the ACCMIP simulations, Atmos Chem Phys, 13, 2563-2587, 10.5194/acp-13-2563-2013, 2013.

Williamson, C. J., Kupc, A., Rollins, A., Kazil, J., Froyd, K. D., Ray, E. A., Murphy, D. M., Schill, G. P., Peischl, J., Thompson, C., Bourgeois, I., Thomas, B. R. A., Diskin, G. S., DiGangi, J. P., Blake, D. R., Bui, T. P. V., Dollner, M., Weinzierl, B., and Brock, C. A. (2021), Large hemispheric difference in nucleation mode aerosol concentrations in the lowermost stratosphere at mid- and high latitudes, Atmos Chem Phys, 21, 9065-9088, 10.5194/acp-21-9065-2021, 2021.

Wofsy, S.C., S. Afshar, H.M. Allen, E.C. Apel, E.C. Asher, B. Barletta, J. Bent, H. Bian, B.C. Biggs, D.R. Blake, N. Blake, I. Bourgeois, C.A. Brock, W.H. Brune, J.W. Budney, T.P. Bui, A. Butler, P. Campuzano-Jost, C.S. Chang, M. Chin, R. Commane, G. Correa, J.D. Crounse, P. D. Cullis, B.C. Daube, D.A. Day, J.M. Dean-Day, J.E. Dibb, J.P. DiGangi, G.S. Diskin, M. Dollner, J.W. Elkins, F. Erdesz, A.M. Fiore, C.M. Flynn, K.D. Froyd, D.W. Gesler, S.R. Hall, T.F. Hanisco, R.A. Hannun, A.J. Hills, E.J. Hintsa, A. Hoffman, R.S. Hornbrook, L.G. Huey, S. Hughes, J.L. Jimenez, B.J. Johnson, J.M. Katich, R.F. Keeling, M.J. Kim, A. Kupc, L.R. Lait, K. McKain, R.J. Mclaughlin, S. Meinardi, D.O. Miller, S.A. Montzka, F.L. Moore, E.J. Morgan, D.M. Murphy, L.T. Murray, B.A. Nault, J.A. Neuman, P.A. Newman, J.M. Nicely, X. Pan, W. Paplawsky, J. Peischl, M.J. Prather, D.J. Price, E.A. Ray, J.M. Reeves, M. Richardson, A.W. Rollins, K.H. Rosenlof, T.B. Ryerson, E. Scheuer, G.P. Schill, J.C. Schroder, J.P. Schwarz, J.M. St.Clair, S.D. Steenrod, B.B. Stephens, S.A. Strode, C. Sweeney, D. Tanner, A.P. Teng, A.B. Thames, C.R. Thompson, K. Ullmann, P.R. Veres, N.L. Wagner, A. Watt, R. Weber, B.B. Weinzierl, P.O. Wennberg, C.J. Williamson, J.C. Wilson, G.M. Wolfe, C.T. Woods, L.H. Zeng, and N. Vieznor (2021). ATom: Merged Atmospheric Chemistry, Trace Gases, and Aerosols, Version 2. ORNL DAAC, Oak Ridge, Tennessee, USA. https://doi.org/10.3334/ORNLDAAC/1925, 2021.

Wolfe, G. M., Nicely, J. M., Clair, J. M. S., Hanisco, T. F., Liao, J., Oman, L. D., Brune, W. B., Miller, D., Thames, A., Abad, G. G., Ryerson, T. B., Thompson, C. R., Peischl, J., McCain, K., Sweeney, C., Wennberg, P. O., Kim, M., Crounse, J. D., Hall, S. R., Ullmann, K., Diskin, G., Bui, P., Chang, C., and Dean-Day, J. (2019), Mapping hydroxyl variability throughout the global remote troposphere via synthesis of airborne and satellite formaldehyde observations, P Natl Acad Sci USA, 116, 11171-11180, 10.1073/pnas.1821661116, 2019.

Young, P. J., Naik, V., Fiore, A. M., Gaudel, A., Guo, J., Lin, M. Y., Neu, J. L., Parrish, D. D., Rieder, H. E., Schnell, J. L., Tilmes, S., Wild, O., Zhang, L., Ziemke, J., Brandt, J., Delcloo, A., Doherty, R. M., Geels, C., Hegglin, M. I., Hu, L., Im, U., Kumar, R., Luhar, A., Murray, L., Plummer, D., Rodriguez, J., Saiz-Lopez, A., Schultz, M. G., Woodhouse, M. T., and

Zeng, G., (2018) Tropospheric Ozone Assessment Report: Assessment of global-scale model performance for global and regional ozone distributions, variability, and trends, Elementa-Science of the Anthropocene, 6, 10.1525/elementa.265, 2018.